

Investigation of Photodegradation in Optical Chemical Sensors

Dipl.-Ing. Barbara Enko

DISSERTATION

zur Erlangung des akademischen Grades
einer Doktorin der technischen Wissenschaften
der Studienrichtung
Technische Chemie
erreicht an der
Technischen Universität Graz

Univ.-Prof. Mag.rer.nat. Dr.phil. Georg Gescheidt-Demner
Institut für Physikalische und Theoretische Chemie
Technische Universität Graz

Graz 2012

Dedicated to my family
Mama, Papa, Richi, Bine
and Daniel.

Acknowledgements

With this thesis, eleven years at the University of Technology Graz come to an end. At this point, I want to thank people that guided and supported me through all this time.

Foremost, I thank my advisor Univ.-Prof. Mag.rer.nat. Dr.phil. Georg Gescheidt-Demner for continuous support of my Ph.D study and research, for his patience, motivation, humour, guidance and knowledge. He fostered my professional autonomy and encouraged me to develop scientific ideas and put them into practice.

I thank my co-advisor Univ.-Prof. Dipl.-Chem. Dr.rer.nat. Ingo Klimant for valuable scientific contributions, help in the realization of ideas and his dedication of significant amounts of time and thought to this project. He taught me relevant ways of thinking, working and analyzing in the field of optical chemical sensors.

I give my sincere gratitude to Dr. Sergey Borisov, who constantly and essentially helped and supported me. He showed me how to creatively and passionately develop, set up and conduct smart experiments. Furthermore, he always took time and effort to support me in scientific writing.

I thank the programme “FreChe Materie” for financing my PhD thesis and all people responsible for making this programme a valuable and enriching experience to me. Thanks to my industry mentor Dr. Claudia Muresanu for good advice, Univ.-Prof. Dipl.-Chem. Dr.rer.nat. Frank Uhlig for leading the programme, Maria Theresia Koller and Ing. Mitra Mitteregger for patient and friendly help with administration and the other mentees for nice dinners and meetings. I am especially thankful to DI Claudia von der Linden for great and valuable career coaching sessions.

I am thankful to Prof.Dr. Wolfgang Bäumlner and Dr. Johannes Regensburger at the University of Regensburg for hosting me for one month in their institute and conducting the singlet oxygen luminescence spectroscopy experiments. Further, I thank Prof. Dr. Diederich and Dr. Milan Kivala for providing super-acceptor substances and publishing.

I thank my colleagues at the Institute of Physical and Theoretical Chemistry. Apart from valuable coffee breaks, Christine Onitsch spent countless hours in sample and solvent preparation with me and we shared the challenging experience of repairing our beloved ENDOR. Thanks to Ulf Rosspeintner for neverending enthusiasm, Dmytro “Dimi” Neshchadin for asking me constantly how my writing is and jumping to help whenever needed, Markus Griesser for sharing knowledge and skill in just about everything nerdy, Michal Zalibera for being my EPR joker and Pawel Cias for fun breaks. Working in this group was interesting and fun. I am grateful to Marion Hofmeister for always friendly support in administration, Hilde Freißmuth for all her supplies magic and Ing. Helmut Eisenkölbl for patiently helping and fixing almost everything that is to be plugged in a power socket.

A great thanks to my colleagues at the Institute of Analytical Chemistry and Food Chemistry. Wernfried Haas and Gunter Zenkl were “PhD older brothers” to me and we became good friends over the years. Apart from being my MATLAB magician, Birgit Ungerböck became a dear friend and important mental support to me (“Great minds think alike”). I thank Kerstin Waich and Günter Mistlberger for encouraging, helpful and fun coffee/beer talks, Tobi Abel(s) and Klaus Koren for repeatedly helping me with switches and cable stuff and Gerda Winterleitner for preparing modified singlet oxygen quenchers and polymers. A big thank you to the rest of the gang (Babsi, Chrissi, Christoph, Daniel, Eveline, Lisi, Lukas, Michela, Philipp, Spela, Torsten, Tobi, ...) for so many great lunch- and coffee breaks, fun trips and beers. I guess lunch at work will never be the same delicious and fun anywhere else.

I thank all my friends for their love and support (Mone, Flo, Flo, Ulli, René (here’s your name in my thesis), Carmen, Thommi, ...). I thank my friend Gernot Rauch who is also my Shiatsu therapist for helping me and my body sustain and the DSA crowd (Claudia, Daniel, Harald, Monika, Tina, Wernfried) for letting me escape from time to time. I thank all sources of pleasant escapism: Singers of songs and makers of music, J. Michael Straczynski for creating “Babylon 5”, Marion Zimmer Bradley for creating “Darkover” and the Avalon series, Michael Landon for creating “Little House on the Prairie” and the owner of the “Keller”. Thanks to Claudia and Wernfried for great weekly dinners, barbecues and “my” place on the couch. A thank you goes out to all the LaTeX-nerds out there who like to spend their time solving LaTeX problems for people like me.

The most important gratitude is to my family, Resi, Fredi, Richi, Bine and Daniel. Without your constant support, time, encouragement and deep love, I wouldn’t have made it.

Eidesstattliche Erklärung

Ich erkläre an Eides statt, dass ich die vorliegende Arbeit selbstständig verfasst, andere als die angegebenen Quellen/Hilfsmittel nicht benutzt, und die den benutzten Quellen wörtlich und inhaltlich entnommenen Stellen als solche kenntlich gemacht habe.

Statutory Declaration

I declare that I have authored this thesis independently, that I have not used other than the declared sources/resources, and that I have explicitly marked all material which has been quoted either literally or by content from the used sources.

Graz, im März 2012

Abstract

The interaction of light and organic matter builds the core concept applied in optical chemical sensors. At the same time, this interaction can lead to photochemical processes causing photodegradation of components employed in the sensor. Photodegradation alters physical and chemical properties of sensor components, often at the price of sensor performance. The underlying mechanisms of photodegradation in optical chemical sensors are not yet understood.

This thesis aims to investigate chemical processes contributing to photodegradation in optical chemical sensors, focusing on mechanisms involving photosensitized singlet oxygen. In doing so, this work also clarifies the role of singlet oxygen in photodegradation with respect to other potential contributing mechanisms. Further, singlet oxygen quenchers and their performance as stabilizing agents in optical chemical sensors are investigated.

Zusammenfassung

Die Wechselwirkung zwischen Licht und organischer Materie stellt das Kernkonzept optischer chemischer Sensoren dar. Diese Wechselwirkung kann zu photochemischen Prozessen führen, die die Photodegradation eingesetzter Sensorkomponenten verursachen. Photodegradation verändert physikalische und chemische Eigenschaften von Sensorkomponenten, oft auf Kosten der Leistung des Sensors. Die der Photodegradation von optisch chemischen Sensoren zugrunde liegenden Mechanismen sind noch nicht aufgeklärt.

Das Ziel dieser Dissertation ist es, chemische Prozesse, die zur Photodegradation beitragen, zu untersuchen, im Speziellen Mechanismen, die Singulett-Sauerstoff involvieren. Dabei wird die Rolle des Singulett-Sauerstoffs im Vergleich zu anderen potentiellen Mechanismen, die zur Photodegradation beitragen, aufgeklärt. Weiters werden Singulett-Sauerstofflöcher und ihre Wirkung als stabilisierende Komponenten in optischen chemischen Sensoren untersucht.

Contents

1	Introduction	1
1.1	Photodegradation Processes in Polymers & Dyes	1
1.1.1	Photodegradation in Polymers	2
1.1.2	Photodegradation of Dyes	5
1.1.3	Singlet Oxygen	8
1.1.4	Stabilizing Strategies in Polymers	13
1.1.5	Stabilizing Strategies in Dyes	14
1.2	Photodegradation Processes in Optical Chemical Sensors . . .	16
1.2.1	Optical Chemical Sensors	16
1.2.2	Interaction of Polymers and Dyes upon Irradiation . .	20
1.2.3	Stabilization Strategies in Optical Chemical Sensors . .	21
1.2.4	Previous Work	21
1.3	Thesis Overview	24
1.3.1	Aim of this Work	24
1.3.2	Polymer- and Dye Classes investigated in this Work . .	24
1.3.3	Outline of this Work	28
2	Investigating the Role of $^1\text{O}_2$ in Photodegradation Processes	29
2.1	Introduction	29
2.2	Theory & Methods	31
2.2.1	Absorption Spectroscopy	31
2.2.2	EPR Measurements	32
2.3	Experimental	33
2.3.1	Materials	33
2.3.2	Absorption Spectroscopy Measurements	33
2.3.3	EPR Measurements	34
2.4	Results & Discussion	34
2.4.1	Choice of Materials	34
2.4.2	Determining the Electronic Configuration of B prone to $^1\text{O}_2$ Attack	38

2.4.3	Comparing Photostabilities of various Optical Chemical Sensor Dye Classes in the Ground State	41
2.4.4	EPR measurements	48
2.5	Conclusion	51
3	Investigating the Role of Polymers and $^1\text{O}_2$ Quenchers in Photodegradation Processes	53
3.1	Introduction	53
3.2	Theory & Methods	55
3.2.1	Total Photon Emission (TPE) by $^1\text{O}_2$ in Polymer Films	55
3.2.2	Oxygen Consumption in Polymer Films via Optical Oxygen Sensing	55
3.2.3	Dye Stability in Polymer Films via Absorption Spectroscopy	59
3.3	Experimental	60
3.3.1	Materials	60
3.3.2	Measurements	62
3.4	Results & Discussion	64
3.4.1	Choice of Materials	64
3.4.2	Testing Different $^1\text{O}_2$ Quencher Classes in Different Polymers	68
3.4.3	Testing the Performance of DABCO in Different Polymers	75
3.4.4	Investigating further Amino Compounds for $^1\text{O}_2$ Quenching Ability	85
3.5	Conclusion	90
3.5.1	Polymers	90
3.5.2	$^1\text{O}_2$ Quenchers	91
3.6	Appendix	93
4	EPR Investigations of Organic Super-Acceptors	97
4.1	Introduction ¹	97
4.2	Experimental	99
4.2.1	Sample Preparation	99
4.2.2	Measurements	99
4.3	Results	99
4.4	Conclusion	103
	List of Abbreviations	123

“Understanding is a three-edged sword”

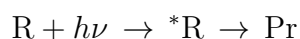
KOSH NARANEK
Babylon 5

Chapter 1

Introduction

1.1 Photodegradation Processes in Polymers & Dyes

The term “Photochemical Reaction” is generally used to describe a chemical reaction caused by absorption of ultraviolet, visible or infrared radiation. There are many ground-state reactions which have photochemical counterparts. Among these are photochemical nitrogen extrusions, photocycloadditions, photodecarbonylations, photodecarboxylations, photoenolizations, photo-Fries rearrangement, photoisomerizations, photooxidations, photorearrangements, photoreductions, photosubstitutions, etc². In basic terms, all photochemical reactions involve the overall process:



where R is an organic molecule that absorbs a photon ($h\nu$), whose frequency (ν) is correct for light absorption by R; *R is an electronically excited molecule; and Pr is an isolated product (or products)³.

Photochemical reactions are deliberately a method of choice in various fields of chemical synthesis because photochemical paths offer the advantage over thermal methods of forming thermodynamically disfavored products, overcome large activation barriers in a short period of time, and allow reactivity otherwise inaccessible by thermal methods. However, undesired photochemical reactions such as photooxidation, photooxygenation or photoinduced electron transfer (PET) in organic materials such as polymers may lead to photodegradation, causing the change or even loss of eventually desired characteristic material properties². Photodegradation and stabilisation methods are subjects of interest in various fields of material science, especially polymer chemistry⁴.

1.1.1 Photodegradation in Polymers

Photodegradation in Polymers has been exhaustively researched since the late 1960's and consequently, publications in the field are abundant. The book "Photodegradation in Polymers" by Jan f. Rabek⁴ reviews and categorizes relevant contributions to the subject and therefore serves as the basis for this section.

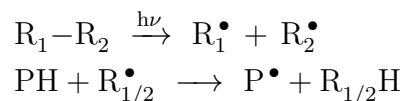
In general, photodegradation processes in polymers proceed through photoinitiated radical chain reactions that generate reactive radical species such as hydroperoxides. The first step initiating these processes is the absorption of radiation (photoinitiation). As polymers consist only of C–C, C–H, C–O and C–Cl bonds, they are not expected to absorb radiation of wavelengths longer than 190 nm. However, present chromophores in the polymer potentially absorb radiation. Chromophores in polymers are of different types and, if not an integral part of the chemical structure of the polymer (such as aromatic groups in polystyrene), part of impurities. These impurities can be categorized as "internal impurities" and "external impurities" and may act as photoinitiators for chemical reactions leading to photodegradation of polymers.

1. **"Internal impurities"** contain chromophoric groups, including
 - hydroperoxides, carbonyl and unsaturated bonds,
 - catalyst residues attached to chain ends of macromolecules,
 - charge-transfer complexes (CTCs) with oxygen.
2. **"External impurities"** contain chromophoric and/or photoreactive groups, including

- traces of catalysts, solvents, etc,
- additives (pigments, dyes thermal stabilizers, antioxidants, photostabilizers, lubricants, plasticizers, etc),
- compounds from polluted urban atmosphere and smog, such as naphthalene, anthracene, etc,
- traces of metals, metal oxides and metal salts from processing equipment and containers. The extrusion, milling, chopping and compounding steps involved in polymer processing can all introduce traces or even particles of such impurities into the polymer.

Different types of impurities lead to different photoinitiation reactions:

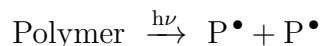
- External low molecular impurities (R_1-R_2) absorb radiation and produce low molecular weight radicals ($R_{1/2}^\bullet$) which further react with a polymer (PH) producing a polymer alkyl radical (P^\bullet) by the hydrogen atom abstraction reaction:



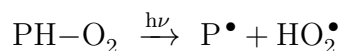
- Internal in-chain and/or end-chain impurity chromophores present as part of a polymer structure absorb light radiation and produce polymer alkyl radicals (P^\bullet) and/or low-molecular radical fragments (R^\bullet):



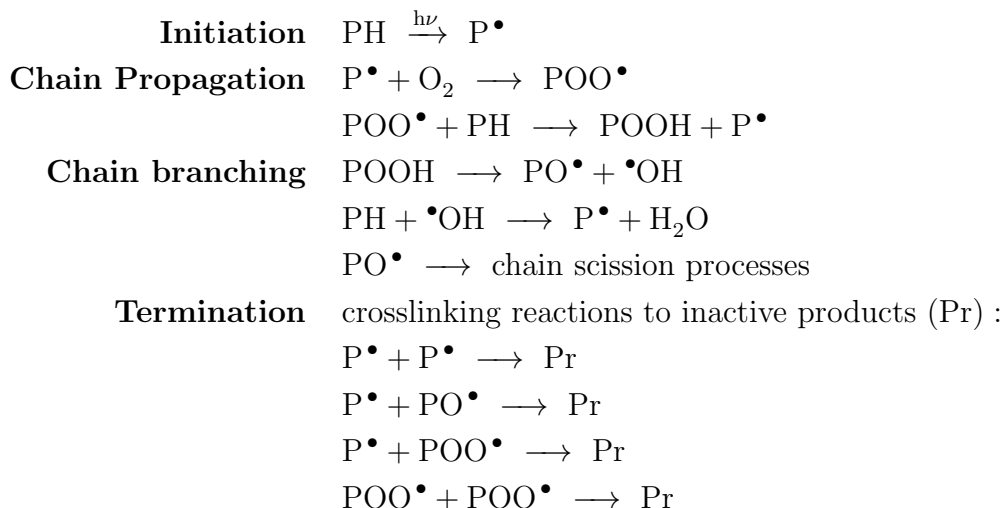
- Direct dissociation of a given chemical bond, which has been excited to the excited singlet or triplet state:



- Charge-transfer complexes (CTCs) formed between polymer and oxygen:



Radicals generated in photoinitiation reactions are highly reactive and cause photo-oxidative degradation processes such as photo-oxidation, chain scission, crosslinking and secondary reactions occurring by free radical mechanisms in the polymer. The mechanistic steps of photo-oxidation include:



where PH is the polymer, P^\bullet is the polymer alkyl radical, PO^\bullet is the polymer alkoxy radical, POO^\bullet is the polymer peroxy radical, POOH is the polymer hydroperoxide and HO^\bullet is the hydroxy radical. In this process, the formation of polymer alkylperoxy radicals (POO^\bullet) by reaction of polymer alkyl radicals (P^\bullet) with oxygen is the key reaction leading to chain propagation. Figure 1.1 gives a schematic overview of the overall mechanism of polymer photo-oxidative degradation. The fact that macroradicals in a solid polymer survive for a long time may account for oxidative degradation and crosslinking which continue for some time after irradiation (“dark processes”).

Photo-oxidation of polymers produces a complex mixture of different products. The identification of these products is key to the evaluation of mechanisms by which the photodegradation reactions occur. Photo-oxidative degradation generally causes main chain scission and crosslinking, the former being generally predominant in the presence of oxygen. Which of the above described reactions is favored in chain branching and termination strongly depends on the type of polymer and impurities present.

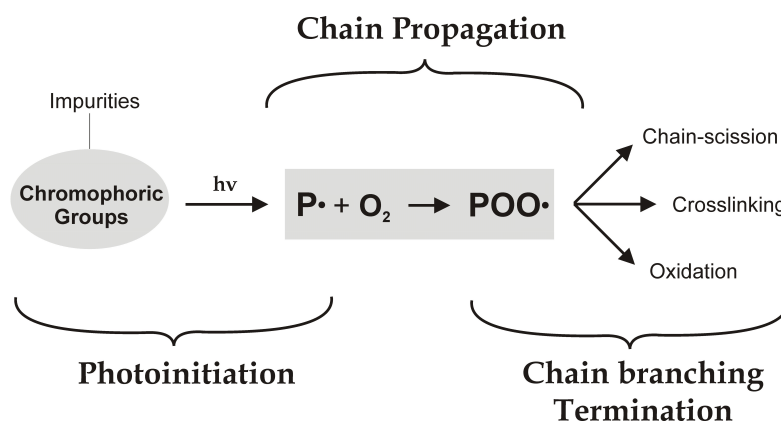


Figure 1.1: General mechanism of polymer photo-oxidative degradation. Internal and external impurities in the polymer carry chromophoric groups, which act as photoinitiators. Photoinitiation leads to polymer alkyl radicals ($PO\cdot$) which react with oxygen giving polymer alkylperoxy radicals, exhibiting the key reaction leading to chain propagation. Chain branching and termination reactions of the radical chain reaction mechanism further lead to chain-scission, crosslinking and oxidative processes in the polymer.

1.1.2 Photodegradation of Dyes

As an intrinsic property, dyes provide structures enabling the absorption of light in the UV and visible region, which may lead to photochemical reactions. Depending on various chemical and physical factors, these photochemical reactions can involve the dyes themselves as reactants and lead to photodegradation of the dyes. The photodegradation of dyes has been observed and studied for almost a century - early reports of the lability of dyes towards light dating back to 1933⁵. While the photodegradation of dyes is deliberately employed and developed in the field of wastewater treatment⁶, it is a highly undesired occurrence in polymers and optical chemical sensors, where dyes are applied as colourants or indicators, respectively. The great variety of dye structures leads to an abundance of possible and probable degradation pathways which are additionally influenced by other chemical species present in the surroundings of the dye. Photodegradation processes of dyes can be categorized in terms of chemical mechanisms:

- Photoaddition
- Photolysis
- Disproportionation

- Attack of photogenerated reactive species

Photoaddition

The term “photoaddition” describes the additive reaction of a dye in its excited state with an organic reactant. The products of photoadditions are species containing the structures of both reactants. A representative example of photoaddition as one photodegradation pathway of a dye has been described by Schöllnhammer and Hemmerich in their work on the photochemistry of Riboflavin⁷. Schuman Jorns et al. described an intramolecular photoaddition mechanism in Riboflavin⁸, which is depicted in figure 1.2. When compared to other photodegradation mechanisms, photoadditions of dyes occur rarely.

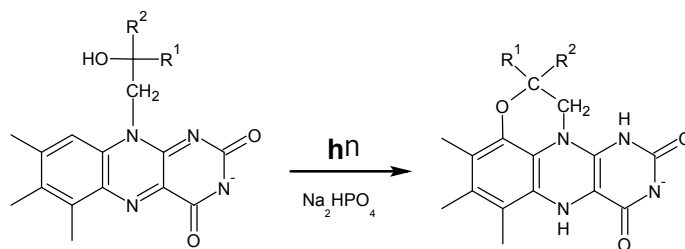


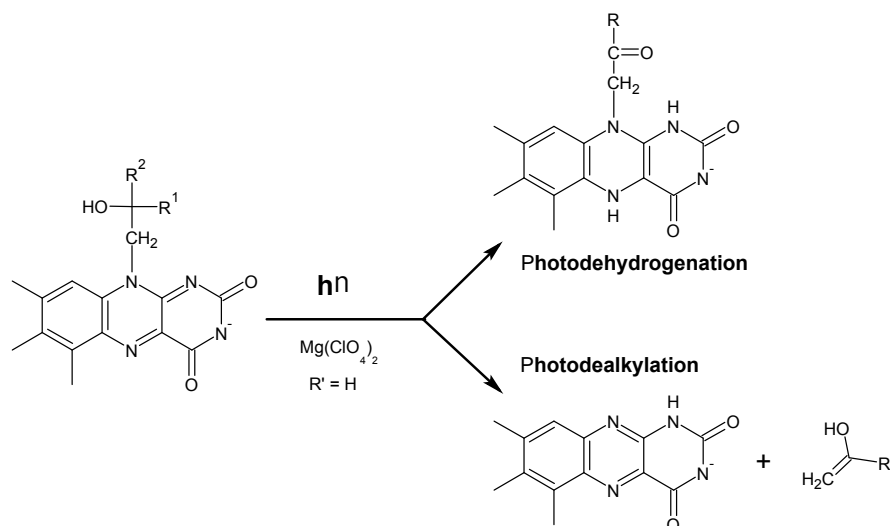
Figure 1.2: Intramolecular photoaddition of Riboflavin⁸.

Photolysis

The photolysis of dyes leads to the decomposition and dissociation (photodissociation) of the dye structure, including ligand loss in organometallic complexes^{9–11}. Photolysis is another possible photodegradation mechanism of above described Riboflavin and occurs as photodehydrogenation and/or photodealkylation of the parent structure, depicted in figure 1.3. Photolysis can occur as a direct consequence of the absorption process but mostly is the follow-up reaction of later described chemical attacks on the dye by a reactive species.

Disproportionation

The disproportionation of dyes results from triplet-triplet annihilation involving an electron transfer step. Triplet-triplet annihilation is a process in which two molecules both in their triplet excited state interact (usually upon collision) to produce one molecule in an excited singlet state and another in

Figure 1.3: Photolysis reactions of Riboflavin⁸.

the ground state². Milosavljevic and Thomas report on an electron transfer from one molecule to the other upon triplet-triplet annihilation, leading to disproportionation of the investigated dye $\text{Ru}(\text{bpy})_3^{2+}$ ¹²:



This mechanism has also been reported by others^{9,10,13}.

Attack of Photogenerated Reactive Species

Photochemical and photophysical processes enable the generation of reactive oxygen species (ROS), such as singlet oxygen ($^1\text{O}_2$) or hydroxyl radicals ($\bullet\text{OH}$). The attack of dyes by these reactive species ultimately leads to photooxygenation or photolysis. This mechanism is the core principle of photocatalytic degradation of dyes in wastewater treatment, where TiO_2 serves as radical generator¹⁴: Upon illumination with UV light, an electron excites out of its energy level and consequently leaves a hole in the valence band. Further, electrons are promoted from the valence band to the conduction band of TiO_2 to give electron-hole pairs. The valence band potential is positive enough to generate hydroxyl radicals ($\bullet\text{OH}$) at the surface of TiO_2 and the conduction band potential is negative enough to reduce molecular oxygen to the oxygen radical anion ($\bullet\text{O}_2^-$), which further reacts with present H_2O to H_2O_2 . H_2O_2 dissociates into two hydroxyl radicals on the TiO_2 surface. Generated hydroxyl radicals ($\bullet\text{OH}$) further attack organic matter in

their surroundings, initiating to degradation processes. Figure 1.4 shows a schematic overview of photocatalysis employing TiO_2 . Many works describe photocatalytic processes involving different catalysts and dyes^{6,14–18}.

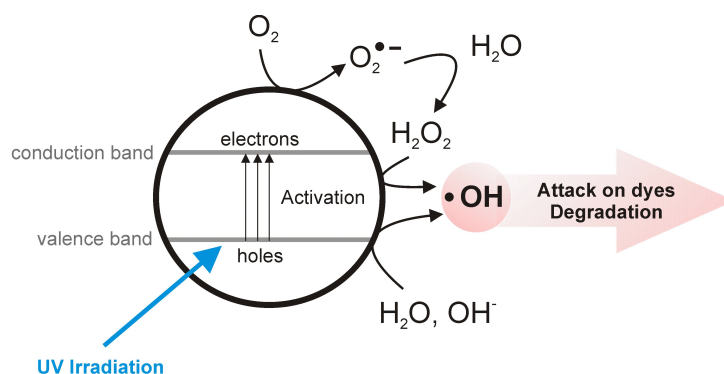


Figure 1.4: General mechanism of the photocatalysis on TiO_2 nanomaterials¹⁴. TiO_2 is irradiated with UV light. Electrons are promoted from the valence band to the conduction band (Activation), giving electron-hole pairs. At the surface of TiO_2 , hydroxyl radicals ($\bullet\text{OH}$) are generated via oxidation of H_2O and OH^- and reduction of molecular oxygen O_2 . Generated hydroxyl radicals ($\bullet\text{OH}$) further attack dyes adsorbed on the surface of TiO_2 , initiating decomposition processes of the dyes (Degradation).

Since this work focuses on the involvement of singlet oxygen in photodegradation processes, the photosensitized generation of singlet oxygen will be discussed in detail in the next section.

1.1.3 Singlet Oxygen

The term “Singlet Oxygen” ($^1\text{O}_2$) refers to the lower lying of the two first electronically excited states of molecular oxygen ($^1\Delta_g$). Due to its open-shell electronic structure, molecular oxygen possesses a special electronic configuration leading to three energetically close lying electronic states, one triplet ground state ($^3\Sigma_g^-$) and two excited states ($^1\Sigma_g^+$ and $^1\Delta_g$), both being of singlet multiplicity¹⁹. The role of $^1\text{O}_2$ in a variety of photooxygenation processes has been demonstrated by many works in the last 80 years^{20,21}. Figure 1.5 gives a schematic overview of $^1\text{O}_2$ generation, application and contribution to photodegradation, all of which will be discussed more detailed in this section.

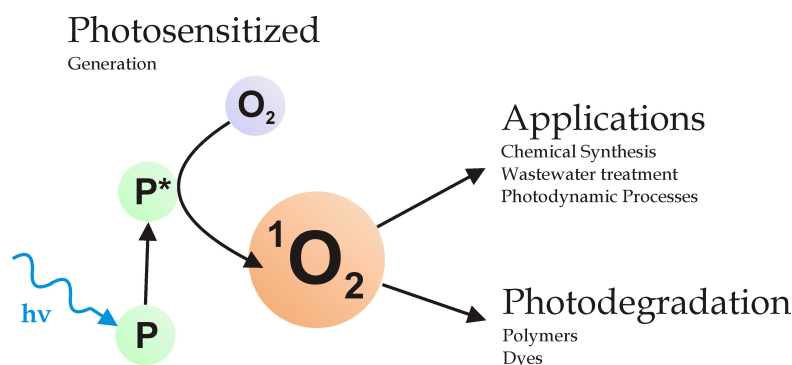


Figure 1.5: Overview of generation, application and contribution to photodegradation of $^1\text{O}_2$. A photosensitizer dye (**P**) is irradiated ($h\nu$) and consequently present in its excited state (**P***). Molecular ground state oxygen (O_2) dynamically quenches **P*** and is excited to $^1\text{O}_2$. The generation of $^1\text{O}_2$ is beneficial in various applications whereas it can also be part of photodegradation processes in polymers and dyes.

Photosensitized Generation of $^1\text{O}_2$

The most common means of $^1\text{O}_2$ generation is photosensitization. Photosensitization, in this case, describes an energy transfer from an electronically excited sensitizer to ground state molecular O_2 ($^3\Sigma_g^-$). A photosensitizer is a molecular entity changing its electronic configuration from its ground state to its excited state via the absorption of light^{2,19}. This process was already mentioned in 1.1 as part of the general description of photochemical reactions:



For deeper understanding, the theory of photosensitization shall be elaborated more detailed. Turro, Ramamurthy and Scaiano dedicate one chapter in their textbook “Modern Molecular Photochemistry of Organic Molecules”³ to Molecular Oxygen and Organic Photochemistry, which holistically covers and explains fundamental theories behind $^1\text{O}_2$ generation and reactivity very detailed. Therefore, this section is based on this chapter. Figure 1.6 shows a Jablonski diagram, in which terms and processes described in the following paragraphs are schematically depicted.

Most organic molecules (except diradicals) possess a ground state of singlet multiplicity. Singlet multiplicity in the ground state (S_0) describes the ground state orbital configuration of two spin-paired electrons in the Highest Occupied Molecular Orbital (HOMO). The radiative transition from the

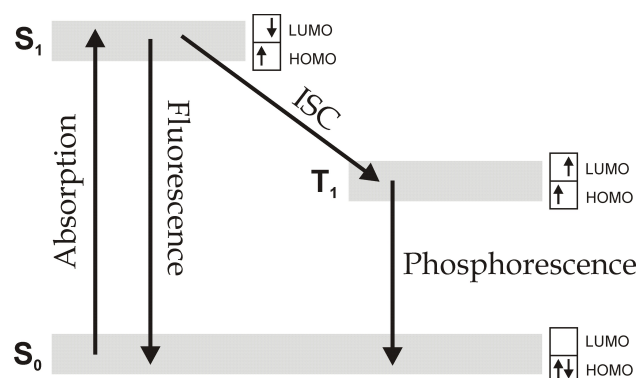


Figure 1.6: Jablonski Diagram.

ground- to the excited state of an organic molecule leads to the occupation of the molecule's Lowest Unoccupied Molecular Orbital (LUMO). There are two possible orbital configurations of the first excited state: (1) In the first excited singlet state (S_1), the electron occupying the HOMO possesses the opposite spin of the LUMO electron. (2) In the first excited triplet state (T_1), the HOMO and the LUMO electrons possess the same spin. The transition from S_0 to T_1 ($S_0 \rightarrow T_1$) is spin-forbidden whereas the transition $S_0 \rightarrow S_1$ is spin-allowed, therefore the latter transition is most probable. In symbolic terms, the most probable radiative transition of an organic molecule from its ground to its excited state can be written as:

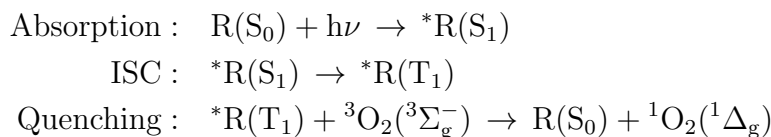


Apart from radiative de-excitation (fluorescence), there are multiple possible relaxation pathways for a molecule in its first excited singlet state, one of which is called Intersystem Crossing (ISC). ISC describes a spin-forbidden transition between two isoenergetic vibrational levels belonging to electronic states of different multiplicities such as the transition $S_1 \rightarrow T_1$ ²². Certain molecular characteristics, such as heavy atom complexes, enhance the probability of ISC (see also 1.3.2). Since the relaxation $T_1 \rightarrow S_0$ is spin-forbidden and highly improbable, the lifetime of the T_1 state compared to that of S_1 is in general relatively long (Radiative decay rates ranges: $S_1 \rightarrow S_0 : (10^6 - 10^9) \text{ s}^{-1}$; $T_1 \rightarrow S_0 : (10^3 - 10^{-2}) \text{ s}^{-1}$).

Both excited states, S_1 and T_1 can be quenched by ground state molecular O_2 (${}^3\Sigma_g^-$). In the dynamic quenching process, the electronically excited molecule *R transfers energy to O_2 (${}^3\Sigma_g^-$). If the amount of transferred energy is sufficient and the total spin is conserved, O_2 (${}^3\Sigma_g^-$) undergoes a transition

to its first excited singlet state, that is $^1\text{O}_2$ ($^1\Delta_g$). In the case of S_1 quenching, the formation of $^1\text{O}_2$ is only feasible if the energy gap ΔE_{ST} between S_1 and T_1 is greater than the energy gap between the triplet ground and singlet state of oxygen ($22.4 \text{ kcal mol}^{-1}$). Such a value for ΔE_{ST} is not uncommon for π, π^* states, which are characteristic for aromatic and polyaromatic systems. However, the efficiency of $^1\text{O}_2$ production through quenching of T_1 states is greater than of S_1 states, respectively, which is explained by significantly longer decay times of the former.

In summary, quenching of excited triplet states (T_1) by ground state O_2 ($^3\Sigma_g^-$) leads to most efficient $^1\text{O}_2$ generation when compared to other processes:



Applications of Photosensitized $^1\text{O}_2$

Many publications and reviews address the application of photosensitized $^1\text{O}_2$ in various fields²³⁻²⁶. The main areas of $^1\text{O}_2$ application are (categories taken from²⁴):

- **Fine Chemical Synthesis:** The versatility and the high degree of stereoselectivity of $^1\text{O}_2$ make it a useful synthetic agent.
- **Wastewater Treatment:** The application of $^1\text{O}_2$ allows the direct use of solar energy in wastewater treatment, thus being a potential economical solution to a difficult environmental problem.
- **Photodynamic Processes:** The photodynamic effect describes the damage of living tissue by the combination of a photosensitizer, visible light, and oxygen. The relevance of photodynamic processes is constantly increasing, especially in the fields of:
 - Blood sterilization
 - Photodynamic therapy of cancer
 - Insecticides and herbicides

The Role of $^1\text{O}_2$ in Photodegradation Processes

While the generation of $^1\text{O}_2$ is an important part of the above described applications, the potential photodegradation of polymers and dyes caused by $^1\text{O}_2$ is undesired in many cases. The reactivity of $^1\text{O}_2$ towards organic molecules and its role in polymer photodegradation has been widely researched and discussed^{20,24,26–32}. $^1\text{O}_2$ has also been part of works about the photodegradation of dyes^{10,12,13,33–35}. While the role of $^1\text{O}_2$ in polymer photodegradation is quite clear, the main mechanisms leading to photodegradation of dyes are still a matter of discussion.

Polymers Pospíšil et al.³⁶ point out that $^1\text{O}_2$ attacks unsaturated segments and structural inhomogeneities in polymers. These reactions account for oxygenated products, hydroperoxides in particular, actively involved in consecutive degradation processes. Further, oxygenation of phenolic antioxidants and UV absorbers (polymer stabilising agents) with $^1\text{O}_2$ depletes their efficiency by interrupting activity mechanisms and increases their consumption.

While $^1\text{O}_2$ may not directly initiate photodegradation chain reactions in polymers, it certainly enhances various mechanisms contributing to photodegradation³⁶. When, for example, applied as matrix material in optical chemical sensors, polymers may react with embedded dyes³³ and are certainly exposed to higher $^1\text{O}_2$ concentrations than in other applications not involving $^1\text{O}_2$ sensitizers. Under such circumstances, $^1\text{O}_2$ attack might be added to relevant photodegradation mechanisms and further investigated.

Dyes Upon the photodegradation mechanisms of dyes discussed in section 1.1.2, the attack of the dye by photogenerated reactive species is a strongly contributing process. Since photosensitized $^1\text{O}_2$ is generated via the excited triplet state of a dye molecule (sensitizer), dyes populating this state are more likely to produce $^1\text{O}_2$. Consequently, the role of $^1\text{O}_2$ in photodegradation depends on the photophysical characteristics of the dye.

The most important parameter for any potential sensitizer considering the formation of $^1\text{O}_2$ is called the *efficiency for singlet oxygen generation* (S_Δ) and defines the fraction of triplet quenching events that result in the

formation of singlet oxygen³:

$$S_{\Delta} = \frac{\text{moles of singlet oxygen formed}}{\text{moles of excited triplets quenched by oxygen}}$$

According to³, various parameters and sensitizer/matrix characteristics influence the efficiency of singlet oxygen generation:

- High value of S_{Δ} .
- Long triplet lifetimes in order to maximize triplet quenching.
- Good spectral properties enabling selective excitation of the sensitizer.
- A solvent with good $^1\text{O}_2$ solubility and where $^1\text{O}_2$ has a long lifetime.

There are works about photosensitized $^1\text{O}_2$ attack leading to photooxygenation of dyes^{10,11,34,37}. Sensitization of $^1\text{O}_2$ might also lead to generation of other ROS such as hydroperoxide radicals, that consequently contribute to photodegradation³⁸. However, the role of $^1\text{O}_2$ in photodegradation processes is still a matter of discussion.

1.1.4 Stabilizing Strategies in Polymers

The overall photodegradation processes in polymers have been discussed in section 1.1.1. Photodegradation in polymers is a conglomerate of photoinitiated radical chain reactions. Chromophoric groups stemming from internal or external impurities act as photoinitiators by absorbing light and reacting with oxygen giving alkoxy peroxide radicals which again propagate further radical chain reactions. Photoinitiation and following radical chain reactions can be prevented and/or terminated by adding different stabilizing agents to the polymer, thereby influencing different aspects of photodegradation. Publications in the field of polymerstabilization are manifold, the categories used in this section are based on a review by Hans Zweifel³⁹.

According to their mode of action, polymer stabilizers can be categorized as follows:

- **Antioxidants**
 - H-Donors (aromatic amines, phenols) hinder hydrogen abstraction of peroxy radicals from the polymer backbone.

- Hydroperoxide decomposers (phosphites, phosphonites, thiosyn-ergists) transform hydroperoxides into non-radical, non-reactive and thermally stable products.
- Alkyl radical scavengers (hindered amine light stabilizers (HALS), hydroxyl amines, benzofuranone derivatives) react with alkyl radicals to form non-reactive products.
- **Metal Deactivators** form stable complexes with metal ions which, uncomplexed, catalyze the decomposition of peroxides forming reactive radicals.
- **Light Stabilizers**
 - UV absorbers absorb UV radiation hence hindering absorption by potential photoinitiators (chromophoric groups) present in the polymer.
 - Quenchers dynamically quench and thereby deactivate chromophoric side groups from their excited state to their ground state.
 - Hindered Amine Light Stabilizers (HALS) are still a matter of discussion in terms of their exact stabilizing mechanisms.

Amongst these stabilizers, the group of Hindered Amine Light Stabilizers (HALS) draws special attention. HALS are sterically hindered amines based on tetramethyl piperidine (figure 1.7) derivatives. Basically, there are two modes of action for HALS as stabilizers in polymers: (1) radical scavenging and (2) quenching of polymer-oxygen CTCs⁴⁰. However, HALS don't seem to prevent reactions of ¹O₂ in polymers^{36,41}.

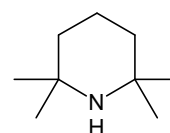


Figure 1.7:
2,2,6,6-
Tetramethylpiperidine

1.1.5 Stabilizing Strategies in Dyes

In order to stabilize dyes, multiple aspects of photodegradation need to be considered. According to mechanism, several stabilization strategies may be effective:

- Triplet-triplet annihilation and consecutive effects can be prevented by **low dye concentrations**.

-
- Ligand loss is subject to the architecture of transition metal complexes and therefore can only be prevented by ligand derivatisation, tuning of excited state energies and modifying ligand coordination geometries.
 - Photooxygenation and other reactions caused by photogenerated reactive species such as $^1\text{O}_2$ may be prevented through several strategies:
 1. **Derivatization** of the dye structure can stabilize the dye towards $^1\text{O}_2$ attack. The introduction of chloride substituents, for example, reduces the oxidation potential of aromatic systems⁴².
 2. By **avoiding population of triplet excited states**, potential generation of $^1\text{O}_2$ is avoided.
 3. Deactivating $^1\text{O}_2$ by **employing $^1\text{O}_2$ quenchers** in the dye environment also has stabilizing effects, whereat physical $^1\text{O}_2$ quenching (without chemical reactions) is preferable.
 4. Embedding dyes in materials such as clay⁴³ or montmorillonite⁴⁴ hinders ROS in diffusing to the dye area.

1.2 Photodegradation Processes in Optical Chemical Sensors

1.2.1 Optical Chemical Sensors

According to the IUPAC definition, a chemical sensor is⁴⁵ “a device that transforms chemical information, ranging from concentration of a specific sample component to total composition analysis, into an analytically useful signal.” . This definition of a chemical sensor was modified and specified by The Cambridge Definition of Chemical Sensors⁴⁶:

“Chemical sensors are miniaturized devices that can deliver real-time and on-line information on the presence of specific compounds or ions in even complex samples.”

The main elements of a sensing system are⁴⁷:

- Analyte
- Transduction Platform
- Signal Processing Unit

The transduction platforms of optical chemical sensors (OCS) are based on measuring changes of an optical property: refractive index, light scattering, reflectance, absorbance, fluorescence, chemiluminescence, etc.²². Some analytes possess optically active properties that can be measured, however, for most sensors, a transduction mechanism including an optically active species (further referred to as indicator, dye or sensitizer) that interacts with the analyte is needed. The interaction of the sensor dye with the analyte causes measurable changes of optical dye properties. The Jablonski diagram depicted in figure 1.6 shows photophysical processes which can serve as transduction platforms for optical chemical sensors. The most widely used techniques employed in optical chemical sensors are optical absorption and luminescence⁴⁷.

Absorption-based OCS

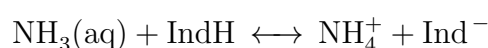
In absorption-based OCS, the absorption characteristics of the employed indicator dye change upon reaction with the analyte. This principle is commonly used in colorimetric pH sensing where pH indicators are employed. The pK_a of these indicators indicates the center of the measurable pH range, for example, cresol red, bromophenol blue and bromocresol purple respond

to acidic pH (pH <7) while naphtholbenzene and phenolphthalein respond at basic pH (pH >7)⁴⁷. The relatively narrow pH response range of most of these dyes has been addressed whereby several indicators with different pK_a values have been combined in one sensor in order to produce a linear pH response over a wide range⁴⁸.

Fluorescence-based OCS

In fluorescence-based OCS, the fluorescence characteristics of the employed indicator dye change upon reaction with the analyte. A trace ammonia sensor employing Eosin as fluorescence indicator serves as an example for fluorescence-based OCS.

There are many applications needing the detection of dissolved ammonia concentrations at sub mg/l-levels since ammonia is reported to be toxic for aquatic organisms above a concentration of 25 μg/l⁴⁹. An ammonia sensor system, presented in the work of Waich et. al⁵⁰, reaches detection limits below 1 μg/l and is based on the change of fluorescence intensity of Eosin ethylester in the presence of ammonia. Eosin ethylester is a xanthene fluorophor dye with a pK_a value of 3.8⁵¹, which is the lowest pK_a value of commercially available dyes of this class. Therefore, Eosin ethylester is the most promising compound for trace measurements of ammonia. The employed sensing principle (depicted in figure 1.8) is the acid-base equilibrium between ammonia (pK_a = 9.24) and the dye (also called indicator, Ind):



The emission characteristics of xanthene dyes strongly depend on species formed by protonation or deprotonation. The deprotonation of Eosin ethylester results in a rise of its fluorescence intensity. Accordingly, the measurable change in Eosin ethylester fluorescence intensity is proportional to ammonia concentration in the dye environment.

Phosphorescence-based OCS

In phosphorescence-based OCS, the phosphorescence characteristics of the employed indicator dye change upon reaction with the analyte. One of the most important applications of phosphorescent indicator dyes in OCS is oxygen sensing. Since oxygen is one of the key analytes, its monitoring is of extreme importance in environmental monitoring, seawater analysis and marine research, food industry medicine, and many other fields of science and

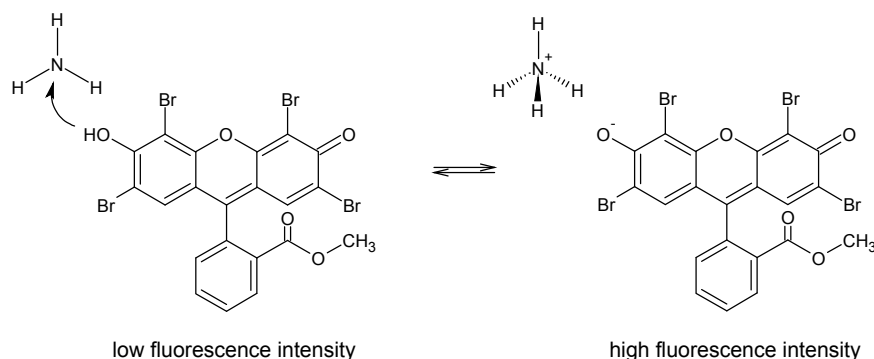


Figure 1.8: Acid-base equilibrium between Ammonia and Eosin⁵⁰.

technology⁵².

The application of phosphorescent indicator dyes in oxygen sensors functions via dynamic quenching of the triplet excited state of the dye by ground state molecular oxygen. The dynamic quenching process is deeply explained on a molecular level in section 1.1.3. The phosphorescence process includes two measurable physical quantities: (1) The emission lifetime (τ) and (2) The emission intensity (I). Dynamic quenching alters both quantities to a measurable extent. The Stern-Volmer relation describes the quantitative (and kinetic) relation between the quencher concentration ($[Q]$) and phosphorescence lifetime and intensity, respectively⁵³:

$$\frac{\tau_0}{\tau} = \frac{I_0}{I} = 1 + K_{SV} [Q]$$

where τ_0 , τ , I_0 and I are luminescence emission lifetimes and intensities in the absence and in the presence of quencher, respectively. $[Q]$ stands for quencher concentration and K_{SV} is the Stern-Volmer constant. The graphical plot of this relation is given in figure 1.9. Various oxygen sensors employ the Stern-Volmer relation of dynamic quenching as transduction platform^{52,54,55}.

Optical Chemical Sensor Design

The employed transduction mechanism is the core of optical chemical sensor design. Since most optical chemical sensors apply organic molecules interacting with light (dyes) as indicators or sensitizers and do not measure intrinsic optical analyte properties, this section confines to design techniques of indirect optical chemical sensors.

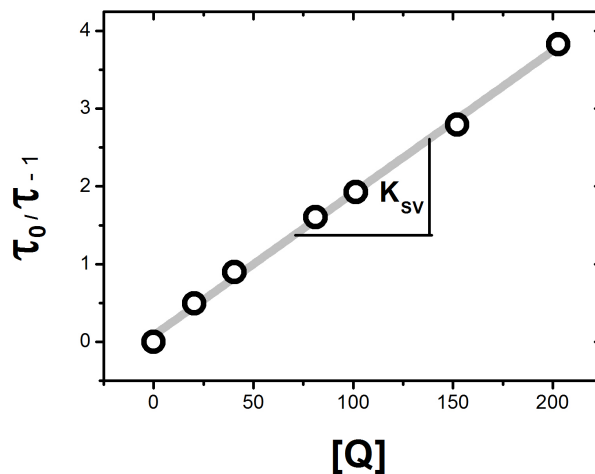


Figure 1.9: Stern-Volmer relation. $\frac{\tau_0}{\tau} - 1$ is plotted versus $[Q]$. The gradient of the linear fit is K_{SV} .

To begin with, the employed indicator needs to be immobilized in a matrix. The sensor matrix should possess certain characteristics such as transparency for light in the needed wavelength region, chemical inertness, permeability for the analyte to the indicator, imperviousness to leaching effects, just to mention a few. Accordingly, polymers and glasses (sol-gel matrices) featuring these characteristics are the first choice as matrix materials. Polymers have been widely used as matrix materials for a broad range of optical chemical sensors. They have many desirable features and compare well with sol-gel matrices for most applications. While polymers may not be as photochemically stable as sol-gels, some polymers are more suitable than sol-gels for high-temperature applications such as autoclavation. Moreover, the use of polymers as matrix materials allows easy processability. The most widely used materials include polystyrene (PS), polyvinyl chloride (PVC), polymethyl methacrylate (PMMA), polydimethyl siloxanes (PDMS) and cellulose derivatives such as ethyl cellulose (EC)^{47,55}.

Further, light needs to be guided from a light source to the indicator and back to a detection system. Waveguiding techniques applied in optical chemical sensors categorize in two fields: (1) Fiber Optic Chemical Sensors (FOCS) and (2) Planar Waveguide Chemical Sensors (PWCS). Various reviews elaborate and discuss these techniques^{47,54,55}, for a detailed description is not essential in this work. It should be noted though that both techniques enable an intense illumination of indicators and light intensity displays an influential quantity in photodegradation processes.

In conclusion, miscellaneous aspects and application requirements govern optical chemical sensor design strategies of which this section mentions the most significant considering photostability: Polymers are often chosen as matrix materials and employed waveguiding techniques may yield in high illumination intensities.

1.2.2 Interaction of Polymers and Dyes upon Irradiation

The embedding of dyes in polymers in optical chemical sensors has effects on the photodegradation on both, the polymer and the dye. Dye photoinitiated degradation of polymers is a phenomenon commonly known in industry as phototendering⁴. Excited dye molecules may abstract a hydrogen atom from a polymer molecule and produce a polymer alkyl radical and protonated dye radical, both leading to further radical chain reactions described in section 1.1.1. While $^1\text{O}_2$ may not directly initiate photodegradation chain reactions in polymers, still it certainly enhances various mechanisms contributing to photodegradation³⁶. When applied as matrix material in optical chemical sensors, polymers are certainly exposed to higher $^1\text{O}_2$ concentrations than in other applications not involving $^1\text{O}_2$ sensitizers. Under such circumstances, $^1\text{O}_2$ attack might be added to relevant photodegradation mechanisms and further investigated.

The photodegradation of dyes in polymers strongly differs from that in solution¹¹. In polymers, the mobility of dyes and the diffusion of gases are restricted, altering the kinetics and relevant interactions of photodegradation processes.

In chapter 1.1, photodegradation processes of polymers and dyes are discussed separately. Contributing mechanisms and factors are well understood and deeply researched in both fields. However, in the field of optical chemical sensors, where dyes are embedded in polymer matrices and commonly accepted degradation mechanisms are altered in terms of their relevance, few is known and understood on a deeper level.

1.2.3 Stabilization Strategies in Optical Chemical Sensors

The fact that photodegradation processes in OCS are not well understood yet causes little success of stabilization attempts. The approach of employing the same stabilizing agents as in polymers may fail due to altered mechanisms contributing to photodegradation of the polymer. Moreover, stabilizers commonly used in polymers can alter sensor characteristics when employed in OCS. HALS, for example, react with molecular oxygen⁵⁶⁻⁵⁸, which is the analyte of oxygen sensors. These reactions bias sensing results.

Dye stabilization strategies discussed in section 1.1.4 often won't be successful in OCS. Preventing triplet-triplet annihilation by lowering dye concentration is often not an option due to the need of high dye concentrations in rather thin polymer films for enhanced sensor performance. The design of indicator dyes is a delicate issue and doesn't always have immense (and sometimes desired) degrees of freedom. Avoiding generation of $^1\text{O}_2$ by avoiding population of triplet excited states is often counterproductive since, for example in oxygen sensors, the $^1\text{O}_2$ generating mechanism displays -at the same time- the very sensing platform. Physical quenching of $^1\text{O}_2$ might be one of the most feasible and effective stabilizing strategies amongst others. However, the role of $^1\text{O}_2$ in OCS photodegradation and potential stabilizing $^1\text{O}_2$ quenchers have not been deeply investigated yet.

1.2.4 Previous Work

In their work about decay kinetics of excited state Ruthenium tris(bipyridine) ($^*\text{Ru}(\text{bpy})_3^{2+}$) adsorbed in cellulose, Milosajevic and Thomas¹² found bleaching effects at $\text{Ru}(\text{bpy})_3^{2+}$ concentrations above 10 mM and high intensity illumination. According to the authors, these bleaching effects are caused by triplet-triplet annihilation involving an electron transfer step, leading to disproportionation of the dye. Photoinduced disproportionation of $\text{Ru}(\text{bpy})_3^{2+}$ has also been studied by Kennelly et al.¹³ on porous Vycor glass, reporting on concentration effects on disproportionation as well. A review on Ru^{2+} polypyridine complexes by Juris et al.⁹ describes ligand photosubstitution and photodissociation processes (“ligand loss”) in addition to electron transfer processes, suggesting strategies to overcome these drawbacks of such complexes. These strategies are based on preventing population of the so-called Metal-Centered excited state (MC), which is key to ligand photosubstitution and photodissociation, and include tuning of excited state energies by changing ligands and modifying ligand coordination geometries as to stabilise the

overall complex structure.

Carraway et al.³⁵ investigated the decomposition of $\text{Ru}(\text{bpy})_3^{2+}$ in silicone rubbers. They found that measured decomposition effects were enhanced in the presence of O_2 . A comparison of three differently substituted and activated Ru^{2+} polypyridine complexes, supposedly diverging in reactivity towards $^1\text{O}_2$, showed an effect of $^1\text{O}_2$ indeed, though the authors ascribed this effect not to $^1\text{O}_2$ but to different photolysis levels of the investigated complexes. They further concluded that $^1\text{O}_2$ is not the primary cause for sensor deactivation. Fuller et al.¹¹ investigated the same complexes as Carraway et al., comparing photostabilities of the complexes in different matrices (polymers and solutions). They found O_2 to be a key agent in photodegradation processes in general. They concluded though, that in solution, O_2 has a somewhat stabilizing effect on the complexes (referred to photodegradation in O_2 -free solutions). According to the authors, this stabilizing effect occurs due to quenching deactivation of the excited state, which displays the initial point of ligand photodissociation. On the contrary, O_2 strongly enhanced photodecomposition of investigated complexes in polymer matrices. This effect is explained by a so-called “cage effect”, in which photosensitized $^1\text{O}_2$ is trapped in close proximity to the sensitizer and has an enhanced opportunity to destroy it. In summary, this work names two main photodegradation mechanisms: (1) photooxidation/ -oxygenation by photosensitized $^1\text{O}_2$ and (2) ligand photosubstitution (or photodissociation). In solution, these two effects are antidiromic - the photosensitization of $^1\text{O}_2$ (through quenching the excited state of the sensitizer) prevents ligand photodissociation. In polymer matrices, the limited diffusion of photosensitized $^1\text{O}_2$ (with respect to solutions) leads to enhanced photooxidation of the sensitizer.

Hartman et al. published two papers on photodegradation of Ru^{2+} polypyridine complexes, investigating the effects of photobleaching on luminescence intensity and lifetime^{10,34}. Further, the effect of $^1\text{O}_2$ quenchers was investigated. These works showed a major influence of oxygen (and photosensitized $^1\text{O}_2$, respectively) on photodegradation processes, manifesting mainly in absorption spectra and emission decay times. Additionally, a polymer matrix dependence of photoeffects was observed. The authors ascribed altered absorption spectra and emission decay times as well as matrix effects in photobleaching experiments to photosensitized $^1\text{O}_2$. In this case, $^1\text{O}_2$ reacts with the sensitizer giving non-emissive, oxygenated photoproducts. The absorption bands of these photoproducts overlap with emission bands of the original sensitizer, leading to RET from sensitizer to photoproduct. This mechanism explains changes of sensitizer emission decay times. Matrix ef-

fects are explained by the varying ability of different polymers for providing acceptor vibrational modes for excited ($^1\text{O}_2$) singlet state energy. However, in agreement with the above mentioned work of Carraway et al.³⁵, luminescence intensity decrease is suggested to be dominated by ligand loss. All results were in agreement with obtained MALDI-TOF data. In addition to photophysical and photochemical characterisations of photodegradation processes, investigations of different tertiary amines as $^1\text{O}_2$ quenchers proved 1,4-DiAzaBiCyclo[2.2.2]Octane (DABCO) to act as an efficient photostabilizing agent in examined sensor films.

In their work on fluorescent pH sensors, Weidgans et al.⁴² reported photostability tests on differently substituted Fluoresceins. They found that electron-withdrawing substituents on the chromophore system of the dye, such as chloro substituents, have a stabilizing effect whereas alkyl substituents such as dihexyl strongly decrease photostability. Borisov et al.⁵⁹ performed similar tests on Fluoresceins, comparing them to a lipophilic HPTS derivative. The results were in agreement with the results of Weidgans et al. and showed that the tested HPTS derivative possesses a greater photostability than the tested Fluorescein derivatives. In another publication, Borisov et al.³⁷ investigated the photostability of various metalloporphyrins, ascribing photodegradation to attack of photosensitized $^1\text{O}_2$. Apart from cyclovoltammetric measurements determining oxidation potentials of investigated dyes in³⁷, the latter mentioned works did not further investigate photodegradation mechanisms.

Õige et al.⁶⁰ studied effects of long-term aging on various characteristics of an oxygen sensor consisting of a Pt^{2+} porphyrin complex in a PMMA film. The decrease of sensor performance over aging time under varied conditions was in general ascribed to polymer deplasticization and physical aging. No further mechanistical interpretation was made whatsoever. Jivaramonaikul et al.⁶¹ synthesized various substituted 4-methylcoumarin derivatives and found that the photostability of these compounds is affected by substitution positions as well as types of substituents. One photostability testing experiment was carried out in the absence and in the presence of oxygen and resulted in no significant difference of degradation data. However, they did not further generalize their results nor investigate photodegradation mechanisms in detail.

1.3 Thesis Overview

1.3.1 Aim of this Work

Since photodegradation processes in OCS are not well understood, the elaboration of stabilization strategies is a challenge not yet successfully met. This work aims to clarify the role of $^1\text{O}_2$ in photodegradation processes and further establish stabilizing strategies for optical chemical sensors based on the physical quenching of $^1\text{O}_2$. It does so by investigating the reactivity of commonly applied sensor dyes towards $^1\text{O}_2$ in their ground- as well as excited state, testing the influence of the polymer matrix on photodegradation and finally scanning potential physical $^1\text{O}_2$ quenchers for their suitability as stabilizing agents in optical chemical sensors. The methods applied are absorption spectroscopy, electron paramagnetic resonance (EPR), luminescence spectroscopy and oxygen sensing.

1.3.2 Polymer- and Dye Classes investigated in this Work

Dye classes employed as indicators in optical chemical sensors as well as polymer matrix materials are manifold and their choice primarily depends on the analyte of interest. Various reviews give an overview of established mechanisms and developments in the field^{47,54,55,62-66}. In the following, dye classes involved in this work's research are introduced.

Fluoresceins

Fluorescein (figure 1.10) is a xanthene dye and possesses multiple characteristics qualifying it and its derivatives (Fluoresceins) for the use as indicator in optical chemical sensors:

- High extinction coefficient ($\epsilon = 7.84 \cdot 10^4 \text{ mol cm}^{-1} \text{ l}^{-1}$)⁶⁷
- High fluorescence quantum yield ($\Phi_F = 0.9$)⁶⁷
- Solubility in aqueous media^{67,68}
- Fluorescence properties strongly depend on pH⁴²
- pK_a can be tuned through derivatisation without significantly affecting spectral properties⁵⁹
- Non-toxicity to living cells⁶⁸

Since the fluorescence properties of Fluorescein and its derivatives (Fluoresceins) strongly depend on pH, they represent a favoured class of indicators in optical chemical sensors^{42,59,64,67-70}. Figure 1.8 in section 1.2.1 shows a pH-sensing scheme with a Fluorescein derivative (Eosin ethylester). Apart from pH-sensing, Fluoresceins are also applied in sensing other analytes, such as copper(II) ions⁷¹.

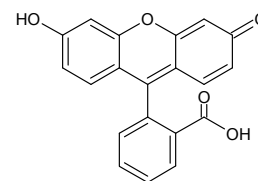


Figure 1.10: Fluorescein.

Coumarins

Coumarin (figure 1.11) shares some characteristics with Fluoresceins, such as a high extinction coefficient, fluorescence quantum yield, easy derivatisation and spectral tuneability, making them also favoured sensor dyes^{72,73}. Coumarin derivatives (Coumarins) offer huge variability and flexibility in their application as indicators in optical chemical sensors.

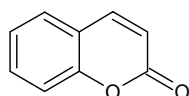


Figure 1.11: Coumarin.

To start with, Coumarins can act as complexation ligands for metal ions. Complexation measurably alters spectral properties of coumarins. For example, depending on substituent groups, complexation might enhance or quench fluorescence of Coumarin moieties. Optical chemical sensors based on enhancement or quenching of fluorescence through complexation of the fluorophore are sometimes called “turn on”, “turn off” or simply “on-off” types⁷³⁻⁷⁵. The range of potential analytes includes Mg^{2+} , Ca^{2+} ⁷⁶, Zn^{2+} , Cd^{2+} ⁷⁷, Fe^{3+} ⁷⁸, Hg^{2+} ⁷⁵ and, most prominently, Cu^{2+} ^{73,74,79,80}. An example of an “on-off” Cu^{2+} sensing mechanism is given in figure 1.12. The coumarin derivative used as indicator changes its absorption maximum (λ_{max}) upon complexation with Cu^{2+} . Additionally, the Cu^{2+} complex is non-fluorescent whereas the uncomplexed coumarin derivative is fluorescent⁷³.

Further, Coumarins serve as indicators for pH based on mechanisms such as intramolecular photoinduced electron transfer⁸¹ or acid-base equilibria as in⁸².

Moreover, Förster Resonance Energy Transfer (FRET) indicator systems employ Coumarins as donor and/or acceptor moieties^{72,83,84}. FRET again is a concept serving different means in optical chemical sensors. For example, FRET is a key process in enhancing brightness of luminescence sensors

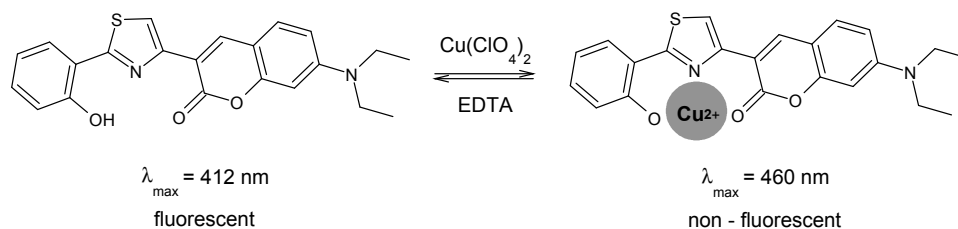


Figure 1.12: “On-off” sensing mechanism for Cu^{2+} ⁷³.

through light harvesting⁷².

HPTS

HPTS abbreviates 1-HydroxyPyrene-3,6,8-TriSulfonate (figure 1.13). HPTS serves as pH indicator in optical chemical sensors based on the equilibrium of its protonated and deprotonated forms^{37,85,86}. In addition to pH sensing, HPTS is employed in CO_2 sensors^{87–91}. Note that for CO_2 , the general sensing principle is the same as in pH sensing: an acid-base equilibrium. In optical chemical CO_2 sensors, HPTS is immobilized in the form of an ion pair. The ion pair is associated with a small amount of H_2O enabling the formation of carbonic acid (H_2CO_3) and subsequent deprotonation reactions in the presence of CO_2 . Deprotonation alters pH which again shifts the acid-base equilibrium of HPTS⁸⁷.

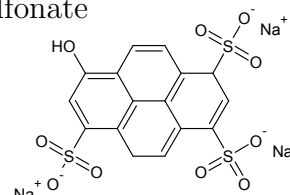


Figure 1.13: HPTS.

Transition Metal Complexes

Upon other applications^{11,92}, transition metal complexes are mainly used as O_2 probes in optical chemical sensors due to their strong luminescence and long lifetimes. The mechanism of O_2 sensing based on luminescence quenching has been explained in section 1.2.1. Long luminescence lifetimes in transition metal complexes stem from enhanced ISC (and therefore strong population of the first triplet excited state T_1) due to the heavy atom effect. The heavy atom effect describes the influence of nuclear charge on spin-orbit induced transitions³. Note that often, the lowest excited state of transition metal complexes is a metal-to-ligand charge transfer state (MLCT), which is responsible for excited-state electron transfer, emission or quenching chem-

istry^{9,11}.

Used transition metals and ligands vary and there has been broad research and development in the field^{55,93,94}. This work concentrates on three transition metal complex categories (structures given in figure 1.3.2):

1. **Metalloporphyrins**^{37,60,92,95}. Especially Pt^{2+} and Pd^{2+} complexes are used as O_2 probes. Note that metalloporphyrins are also deliberately used as photosensitizers of $^1\text{O}_2$ in photodynamic therapy²⁴.
2. **Polypyridyl Complexes**^{9,11,35,96,97}. In this category, Ru^{2+} , Ir^{3+} and Os^{2+} are complexed transition metals with a focus on Ru^{2+} .
3. **Cyclometalated Coumarin Complexes**^{52,98,99}. Ir^{2+} and Pt^{2+} are the most commonly applied transition metals in this category.

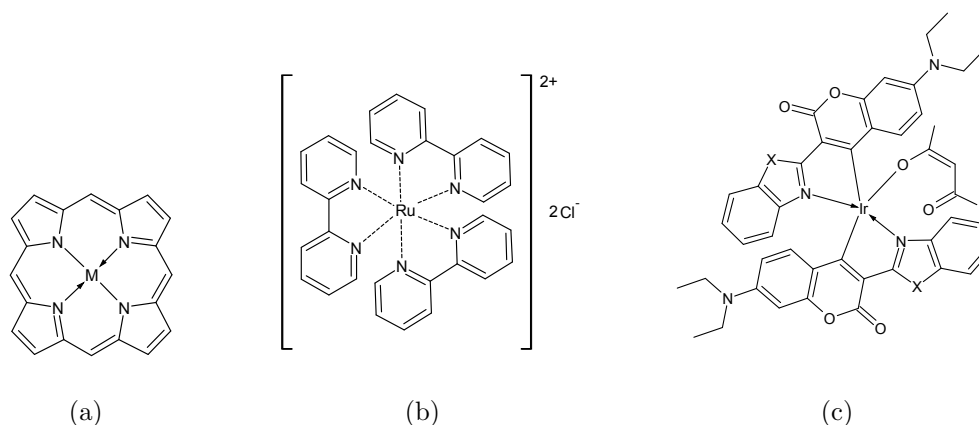


Figure 1.14: Transition metal complexes: (a) Metalloporphyrin, $\text{M} = \text{Pt}^{2+}, \text{Pd}^{2+}$, (b) Polypyridyl Complex ($\text{Ru}(\text{bpy})_3^{2+}$, 2Cl^-), (c) Cyclometalated Coumarin Complexes, $\text{X} = \text{NMe}, \text{O}, \text{S}$,⁵².

A variety of polymers are currently used as matrix materials in optical chemical sensors^{55,93,100}. This work investigates representatives of various polymer classes (according to Polymer Data Handbook¹⁰¹). Names and abbreviations are given in table 1.1.

Table 1.1: Polymers investigated in this work.

Abbreviation	Name	Polymer Class ¹⁰¹
EC	Ethylcellulose	Carbohydrate polymers
D4	Hydrogel D4	Polyurethanes
PMMA	Poly(methyl metacrylate)	Metacrylate polymers
PPO	Poly(2,6-dimethyl-1,4-phenylene oxide)	Polyether engineering thermoplastics
PS	Polystyrene	Vinyl polymers
PSAN	Poly(styrene-co-acrylonitrile)	Copolymer
PSS	Poly(phenylsilesquioxane)	Polysiloxanes
RL	Eudragit RL100	Ammonio metacrylate copolymer type A

1.3.3 Outline of this Work

Chapter 2 This chapter presents investigations on the role of $^1\text{O}_2$ in photodegradation of optical chemical sensor dyes by means of two methods. Both studies are based on a photosensitizer featuring high $^1\text{O}_2$ generation efficiency and photostability, generating a $^1\text{O}_2$ surplus upon irradiation. The effect of a $^1\text{O}_2$ surplus on various sensor dyes was monitored by means of Absorption Spectroscopy and Electron Paramagnetic Resonance (EPR). The established methods provide the possibility to compare photostabilities of a broad variety of sensor dye classes and further allow determining electronic configurations of a dye prone to $^1\text{O}_2$ attack.

Chapter 3 This chapter presents investigations on the role of polymers and $^1\text{O}_2$ quenchers in photodegradation processes of optical chemical sensors. Literature suggests a variety of $^1\text{O}_2$ quenchers^{41,79,102–115}, most of which are claimed to be physical quenchers. Selected based on availability and processability, a set of suggested $^1\text{O}_2$ quenchers has been tested by means of $^1\text{O}_2$ luminescence lifetime, oxygen consumption and dye stability measurements.

Chapter 4 This chapter presents investigations of organic super-acceptors by the means of EPR. Presented results have been published in the attached publication¹.

“We are star stuff. We are the universe made manifest trying to figure itself out.”

DELENN
Babylon 5

Chapter 2

Investigating the Role of $^1\text{O}_2$ in Photodegradation Processes

2.1 Introduction

The role of $^1\text{O}_2$ in photodegradation of optical chemical sensors is still a matter of discussion. Upon other mechanisms such as triplet-triplet annihilation and ligand loss, photosensitized $^1\text{O}_2$ attack is generally considered to contribute to photodegradation. However, the extend to which $^1\text{O}_2$ contributes to photodegradation is unclear. In previous work described in detail in 1.2.4, Carraway et al.³⁵ neglect $^1\text{O}_2$ attack to be a major cause for photodegradation of their investigated dyes whereas Fuller et al.¹¹, investigating the very same dyes as Carraway et al. find $^1\text{O}_2$ attack to be a key process in dye photodegradation in polymer matrices. The works of Hartmann et al.^{10,34} clearly support a theory involving photosensitized $^1\text{O}_2$ attack as primary cause for photodegradation of optical chemical sensors. Borisov et al.³⁷ ascribe photobleaching of investigated metalloporphyrins to oxygenation by photosensitized $^1\text{O}_2$. The means by which the influence of $^1\text{O}_2$ on pho-

Photodegradation was investigated previously primarily included measurements in the absence and presence of O_2 , addition of $^1\text{O}_2$ quenchers to probes and correlating oxidation potentials to photodegradation rates. However, to the best of our knowledge, there hasn't been an attempt to detect $^1\text{O}_2$ and other probably evolving reactive oxygen species in the photobleaching process of optical chemical sensors. Further, any conclusions drawn out of experiments involving one photosensitizer solely strongly depend on the $^1\text{O}_2$ generation efficiency of the sensitizer.

An additional aspect investigated and discussed in this chapter concerns the question as to which electronic configuration of a dye (namely the ground- or excited state, respectively) substantially contributes to the dye's photodegradation. On the one hand, according to the oxidation potential, the excited state of a dye is more prone to $^1\text{O}_2$ attack than its ground state. On the other hand, if irradiated with moderate light intensities, only a small fraction of dye molecules are present in the excited state. The relevance of discussing this question lies in potential stabilization strategies. If only the excited state of the dye contributes significantly to photodegradation, the sensor can be stabilized by employing FRET-cascades as sensing platforms, in which the excited state energy of the labile dye can be transferred to a more stable dye present in the sensor, hence preventing the labile dye from being attacked by $^1\text{O}_2$ in its excited state.

This section presents investigations on the role of $^1\text{O}_2$ in photodegradation of optical chemical sensor dyes by means of two methods. Both studies are based on a photosensitizer featuring high $^1\text{O}_2$ generation efficiency and photostability, generating a $^1\text{O}_2$ surplus upon irradiation. The effect of a $^1\text{O}_2$ surplus on various sensor dyes was monitored by means of Absorption Spectroscopy and Electron Paramagnetic Resonance (EPR). The established methods provide the possibility to compare photostabilities of a broad variety of sensor dye classes and further allow determining electronic configurations of a dye prone to $^1\text{O}_2$ attack.

2.2 Theory & Methods

2.2.1 Absorption Spectroscopy

The photochemical system in use consists of two components: **(A)** A $^1\text{O}_2$ photosensitizer, providing a $^1\text{O}_2$ surplus upon irradiation and **(B)** the investigated dye. Components can either be dissolved in a solvent or immobilized in a polymer matrix. In order to achieve a $^1\text{O}_2$ surplus in solution, the absorption coefficient (ϵ) and concentration of **A** are significantly higher than that of **B**, respectively. Further, the absorption maximum (λ_{max}) of **A** does not overlap spectrally with that of **B** in order to enable investigations of **B** in its ground- as well as excited state. While **A** is irradiated at λ_{max} , leading to $^1\text{O}_2$ generation, **B** can either remain in the ground state or be irradiated independently of **A**. Monitoring the absorption maximum of **B** over time allows direct observation of dye concentration. A decrease in absorption intensity over time at constant pathlength and ϵ directly indicates a decrease of dye concentration due to photodegradation. This measurement setup allows three different experiments, schematically shown in figure 2.1:

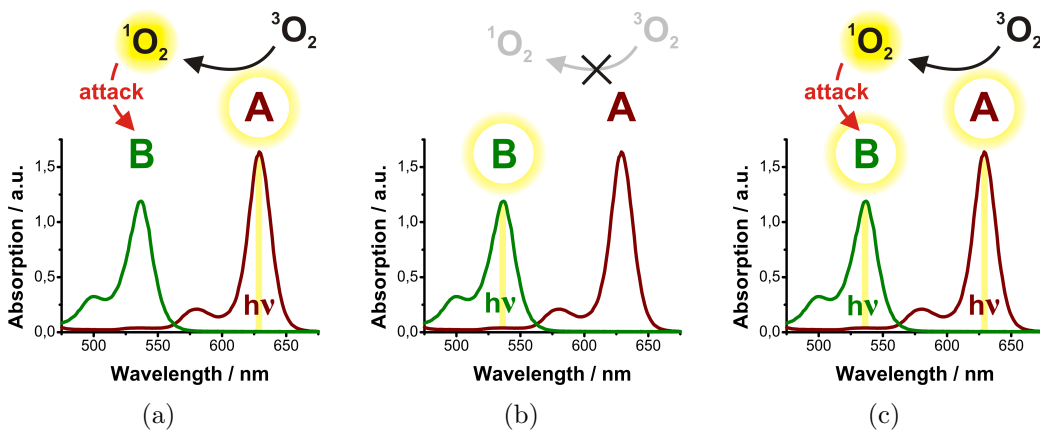


Figure 2.1: Absorption spectroscopy: (a) Irradiation of **A**, generating a $^1\text{O}_2$ surplus (photosensitization) while **B** remains in the ground state and may be attacked by $^1\text{O}_2$. (b) Irradiation of **B**. No $^1\text{O}_2$ surplus generation, the excited state of **B** is populated. (c) Irradiation of **A** and **B**. Irradiation of **A** generates a $^1\text{O}_2$ surplus (photosensitization), **B** is present in excited state and may be attacked by $^1\text{O}_2$.

- **Irradiation of A.** Excited state **A** generates a $^1\text{O}_2$ surplus (through photosensitization). **B** is present in the groundstate. This experiment

While TEMP is diamagnetic and therefore not EPR-active, TEMPO is paramagnetic and gives a triplet EPR signal (depicted in figure 2.3). A change of TEMPO concentration over the course of an experiment results in a proportional change of EPR-signal intensity. TEMP reacts specifically with $^1\text{O}_2$ (when compared to other reactive species) and therefore is a highly selective $^1\text{O}_2$ trap^{119,120}. Accordingly, the EPR-signal intensity of TEMPO is proportional to the $^1\text{O}_2$ concentration in the experiment.

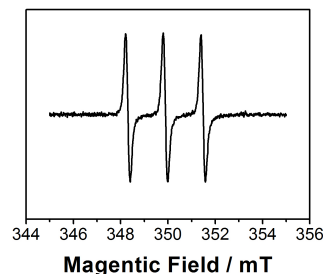


Figure 2.3: EPR signal of TEMPO.

2.3 Experimental

2.3.1 Materials

Pd(II)meso-tetra(4-fluorophenyl)tetrabenzoporphyrin (PdTPBPF, **A1**)³⁷, Pd(II)6-aza-13,20,27-trophenyltetrabenzoporphyrin (PdNTBP, **A2**)⁹⁵, Fluorescein octadecylester (**B1**), 2,7-Dichlorofluorescein octadecylester (**B2**), 2,7-Dihexylfluorescein octadecylester (**B3**)⁴², Ir(III)acetylacetonato-bis(N-methyl-benzimidazol-2-yl-7-diethylaminocoumarin) ($\text{Ir}(\text{C}_N)_2(\text{acac})$, **B9**), Ir(III)acetylacetonato-bis(benzothiazol-2-yl-7-diethylaminocoumarin) ($\text{Ir}(\text{C}_S)_2(\text{acac})$, **B10**)⁵², 1-hydroxypyrene-3,6,8-tris-bis(2-ethylhexyl)sulfonamide (HPTS(DHA), **B12**)⁵⁹ and Pt(II)(2-(2-benzothiazolyl)-7-(diethylamino)-2H-1-benzopyran-2-onato-N ($\text{Pt}(\text{C}_S)(\text{acac})$, **B13**)⁹⁹ were prepared according to literature. Coumarin 545 T (**B4**), Coumarin 30 (C_N , **B7**), Coumarin 6 (C_S , **B8**) Hydroxypyrene-3,6,8-trisulfonate (**B11**) and all solvents were purchased from Sigma-Aldrich (www.sigmaaldrich.com). Macrolux®Fluorescence Yellow 10GN (**B5**) and Macrolux®Fluorescence Red G (**B6**) were purchased from Simon & Werner GmbH (www.simon-und-werner.de). Pt(II)-2,3,7,8,12,13,17,18-octaethyl-21H,23H-porphyrin (PtOEP, **B14**) was purchased from Frontier Scientific (www.frontiersci.com).

2.3.2 Absorption Spectroscopy Measurements

The sample solution containing the $^1\text{O}_2$ sensitizer **A** and the investigated dye **B** was irradiated by a red LED array and/or a blue LED. Over the course of irradiation time, absorption spectra of the sample solution were taken frequently. The sample solution was shaken frequently, maintaining O_2 saturation and homogeneity.

All absorption spectra were acquired at a Cary 50 UV-Vis spectrophotometer (www.lzs-concept.com). The red LED array was a 642 nm high-power 10 W LED array (www.led-tech.de), focused through a lens purchased from Edmund optics (www.edmundoptics.de), operated at 4.2 W input power. The blue LED was a 505 nm LED for **B3** and **B14** and a 475 nm LED for **B8** and **B13**. Both blue LEDs (Roithner, www.roithner-laser.com) had a 5 mm diameter and were operated at 0.4 W input power. The concentration of **A** was $22 \mu\text{mol} \cdot \text{l}^{-1}$, the concentration of **B** was $10 \mu\text{mol} \cdot \text{l}^{-1}$ in all measurements. Fluoresceins (**B1-3**) and HPTS derivatives (**B11-12**) were measured under basic conditions, solutions containing $20 \mu\text{mol} \cdot \text{l}^{-1}$ NaOH. The $^1\text{O}_2$ sensitizer **A2** was used in experiments investigating **B14**, for all other **B**, **A1** was used as $^1\text{O}_2$ sensitizer.

2.3.3 EPR Measurements

The sample solution containing the $^1\text{O}_2$ trap TEMP, the $^1\text{O}_2$ sensitizer **A** and the investigated dye **B** was transferred into a glass tube, mounted in the EPR spectrometer and irradiated by a red LED array mounted in front of the EPR cavity. Over the course of irradiation time, EPR spectra of the sample solution were taken frequently.

All ESP spectra were acquired at a Bruker ESP300e spectrometer. The red LED array was a 642 nm high-power 10 W LED array (www.led-tech.de), focused through a lens purchased from Edmund optics (www.edmundoptics.de), operated at 4.2 W input power. Except for reference experiments containing $0 \mu\text{mol} \cdot \text{l}^{-1}$ of **A** and/or **B** respectively, the concentration of TEMP was $200 \mu\text{mol} \cdot \text{l}^{-1}$, the concentration of **A1** was $20 \mu\text{mol} \cdot \text{l}^{-1}$ and the concentration of **B** was $100 \mu\text{mol} \cdot \text{l}^{-1}$ in all measurements.

2.4 Results & Discussion

2.4.1 Choice of Materials

As described in 2.2.1, the photochemical system in use consists of two components: (**A**) A $^1\text{O}_2$ photosensitizer, providing a $^1\text{O}_2$ surplus upon irradiation and (**B**) the investigated dye. The working materials have been chosen corresponding to the following requirements:

- ϵ and concentration of **A** need to be significantly higher than that of **B**, respectively.

- λ_{\max} of **A** must not overlap with that of **B** in order to allow investigations of **B** in its ground- as well as excited state.
- In order to generate a sufficient amount of $^1\text{O}_2$, the efficiency of $^1\text{O}_2$ generation (S_{Δ} , explained in 1.1.3) should be high in the system, requiring long triplet lifetimes.
- The investigated dyes (**B**) represent dye classes commonly used in optical chemical sensor systems.

Based on these requirements, two metalloporphyrins were employed as $^1\text{O}_2$ sensitizers: (**A1**) *Pd(II)meso-tetra(4-fluorophenyl)tetrabenzoporphyrin* (PdTPPTBPF) and (**A2**) *Pd(II)6-Aza-13,20,27-trophenyltetrabenzoporphyrin* (PdNTBP), their structures are depicted in figure 2.4.

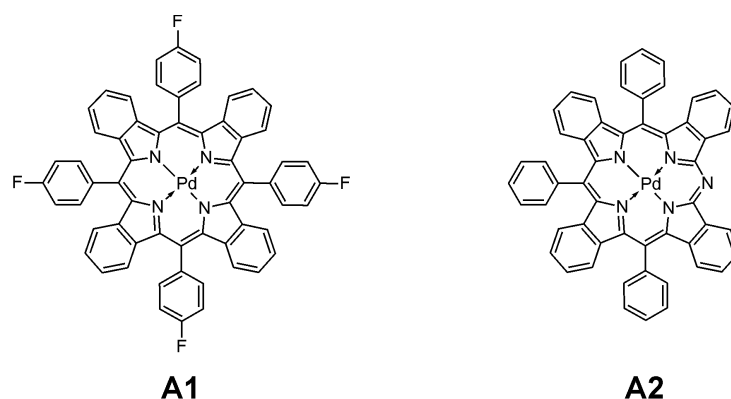


Figure 2.4: $^1\text{O}_2$ sensitizers (**A**); **A1**: PdTPPTBPF, **A2**: PdNTBP.

Both complexes are efficiently excitable by red light ($\lambda_{\max, \text{A1}} = 629 \text{ nm}$, $\epsilon_{\text{A1}} = 115\,000 \text{ M}^{-1} \text{ cm}^{-1}$ ³⁷; $\lambda_{\max, \text{A2}} = 642 \text{ nm}$, $\epsilon_{\text{A2}} = 133\,000 \text{ M}^{-1} \text{ cm}^{-1}$ ⁹⁵). Further, both compounds show virtually no absorption in a relatively broad spectral window (**A1**: 470–560 nm, **A2**: 440–550 nm, see figure 2.5). Since λ_{\max} of all investigated sensor dyes (**B**) are lower than 600 nm, **A** and **B** may be excited selectively, enabling experiments with **B** in the ground- as well as excited state. Both **A** complexes have relatively long

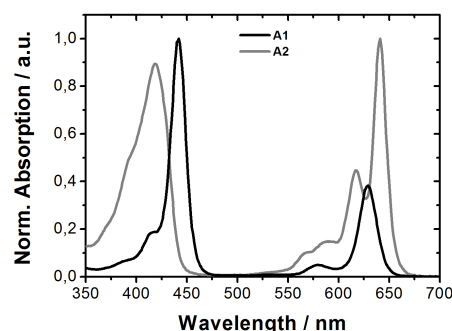


Figure 2.5: Normalized absorption spectra of **A**.

phosphorescence lifetimes in toluene ($\tau_{A1} = 297 \mu\text{s}$, $\tau_{A2} = 213 \mu\text{s}$), providing high probability of oxygen quenching. Neither of the complexes shows fluorescence^{37,95}, indicating that the quantum yields of their triplet states are close to unity and the quenching by oxygen in solution is close to the diffusion controlled limit - leading to estimated high S_{Δ} .

The investigated dyes (**B**) are derivatives of dye classes commonly used in optical chemical sensor systems. These dye classes are introduced in 1.3.2. Dye classes and compound names are given in table 2.1, their structures are depicted in figure 2.6.

Table 2.1: Investigated sensor dyes **B**, representing dye classes commonly used in optical chemical sensor systems.

Dye class	Name	
Fluoresceins	B1	Fluorescein ODE*
	B2	2,7-Dichlorofluorescein ODE* ⁴²
	B3	2,7-Dihexylfluorescein ODE* ⁴²
Coumarins	B4	Coumarin 545 T
	B5	Macrolax®Fluorescence Yellow
	B6	Macrolax®Fluorescence Red
	B7	Coumarin 30 (=C _N)
	B8	Coumarin 6 (=C _S)
Cyclometallated Ir(III)complexes	B9	Ir(C _N) ₂ (acac)** ⁵²
	B10	Ir(C _S) ₂ (acac)** ⁵²
Sulfonated PAH [°]	B11	HPTS
	B12	HPTS(DHA) ₃ (<i>1-hydroxypyrene-3,6,8-tris-bis(2-ethylhexyl)sulfonamide</i>) ⁵⁹
Pt(II)complexes	B13	Pt(C _S)(acac) (<i>Pt(II)(2-(2-benzothiazolyl)-7-(diethylamino)-2H-1-benzopyran-2-onato-N)</i>) ⁹⁹
	B14	PtOEP (<i>Pt(II)octaethylporphyrine</i>)

*ODE = OctaDecylEster, **(acac) = acetylacetonone,
[°]PAH = Polyaromatic Hydrocarbons

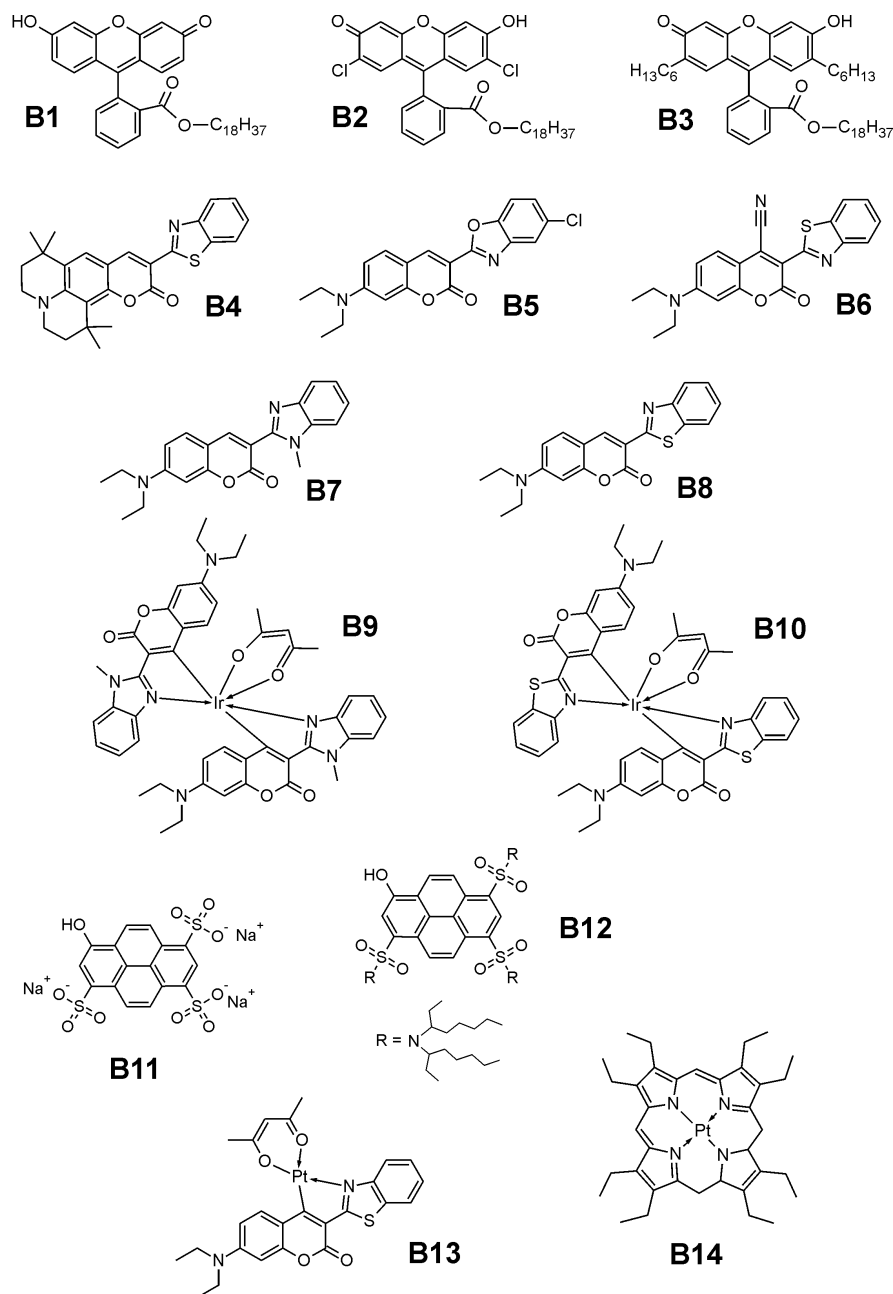


Figure 2.6: Investigated dyes (B); **B1**: Fluorescein ODE, **B2**: 2,7-Dichlorofluorescein ODE, **B3**: 2,7-Dihexylfluorescein ODE, **B4**: Coumarin 545 T, **B5**: Macrolex® Fluorescence Yellow, **B6**: Macrolex® Fluorescence Red, **B7**: Coumarin 30, **B8**: Coumarin 6, **B9**: Ir(C_N)₂(acac), **B10**: Ir(C_S)₂(acac), **B11**: HPTS, **B12**: HPTS(DHA)₃, **B13**: Pt(C_S)(acac), **B14**: PtOEP.

2.4.2 Determining the Electronic Configuration of **B** prone to $^1\text{O}_2$ Attack

The employed absorption spectroscopy measurement setup explained in 2.2.1 allows separate as well as simultaneous irradiation of **A** and **B**. **A** serves as $^1\text{O}_2$ sensitizer, generating a surplus of $^1\text{O}_2$ in the solution. **B** is the investigated dye. Sole irradiation of **B** is similar to common photodegradation experiments, photodegradation might occur due to various mechanisms. Sole irradiation of **A** generates a photosensitized $^1\text{O}_2$ surplus while **B** remains in the ground state. Since **B** is not irradiated, the most probable source of photodegradation is $^1\text{O}_2$ attack on the **B** in the ground state. During simultaneous irradiation of **A** and **B**, a $^1\text{O}_2$ surplus is generated (photosensitization by **A**), while a portion of **B** is present in the excited state. Comparing photodegradation rates of these three experiments allows conclusions as to which electronic configuration (ground- and/or excited state) of **B** is prone to $^1\text{O}_2$ attack.

All experiments have been conducted with four different **B** compounds: **B2** (2,7-Dihexylfluorescein ODE), **B8** (Coumarin 6), **B13** (Pt(C_5)(acac)) and **B14** (PtOEP). The results of these experiments are given in figure 2.7. Each graph shows the results of one **B** compound. Relative absorption maximum (at $\lambda_{\text{max,B}}$) is plotted versus irradiation time. Since absorption intensity is directly proportional to dye concentration, the plotted curves show a decrease in dye content over irradiation time caused by photodegradation. The steepness of these curves will be qualitatively referred to as “degradation rates”. Since the curves fit different mathematical functions, it is not sufficient to quantify degradation rates in a kinetic manner. The data of **B8** are heavily error-prone, however, trends of signal changes are significant. All compounds share one characteristic: Degradation rates in experiments irradiating **B** only (\circ) are very small compared to those of experiments with $^1\text{O}_2$ surplus (irradiation of **A**, \triangle and \blacksquare), respectively. **Accordingly, the presence of $^1\text{O}_2$ dramatically increases photodegradation.** While exciting **B** (in addition to **A**) has a destabilizing effect on **B8** (Coumarin 6) and **B13** (Pt(C_5)(acac)) (degradation rates of \blacksquare are bigger than of \triangle , respectively), **B2** (2,7-Dihexylfluorescein ODE) and **B14** (PtOEP) show quite the contrary behaviour. Obviously, the lifetime and type of the excited state do not indicate which effect is more prominent since 2,7-Dihexylfluorescein ODE and Coumarin 6 are fluorescent dyes with rather short lifetimes compared to Pt(C_5)(acac) and PtOEP, which are both phosphorescent dyes, possessing long triplet state lifetimes. Note that Pt(C_5)(acac) (**B13**) is a Pt(II) complex with Coumarin 6 (**B8**) as ligand. In both compounds, the

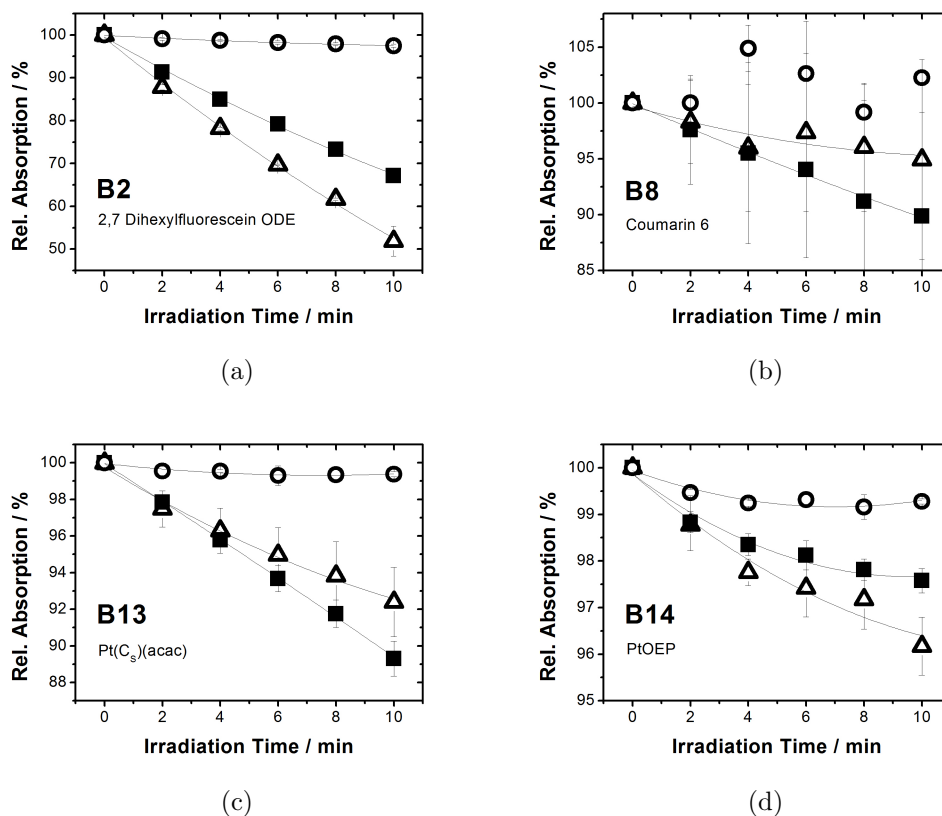


Figure 2.7: Relative absorption maximum of **B** vs. irradiation time, investigating electronic configuration (ground- and/or excited state) prone to $^1\text{O}_2$ attack: \triangle Irradiation of **A**: $^1\text{O}_2$ surplus, **B** in ground state; \circ Irradiation of **B**: NO $^1\text{O}_2$ surplus, **B** in excited state; \blacksquare Irradiation of **A** and **B**: $^1\text{O}_2$ surplus, **B** in excited state; (a) **B2**: 2,7-Dihexylfluorescein ODE, (b) **B8**: Coumarin 6, (c) **B13**: Pt(C₅)(acac), (d) **B14**: PtOEP. The presence of $^1\text{O}_2$ enhances photodegradation in all experiments. All dyes are attacked by $^1\text{O}_2$ in their ground state. The excited state of **B2** and **B14** stabilizes the structure whereas the excited state of **B8** and **B13** destabilizes the structure towards $^1\text{O}_2$ attack.

excited state causes a loss in photostability and increases photodegradation compared to the ground state. Both electronic configurations are attacked by $^1\text{O}_2$, though. This behaviour is not the case for compounds **B2** (2,7-Dihexylfluorescein ODE) and **B13** (Pt(C_S)(acac)). Here, the curves of experiments with **B** in the ground state (Δ) are steeper than the curves of experiments with **B** partially in the excited state (\blacksquare). Accordingly, the excited state of these compounds is not attacked by $^1\text{O}_2$, leading to an increase of photostability compared to the ground state. Apart from aliphatic substituents on the chromophoric π -system, 2,7-Dihexylfluorescein ODE (**B2**) and PtOEP (**B14**) do not share any structural characteristics, **B2** is a fluorescent fluorescein while **B14** is a phosphorescent Pt(II)porphyrin.

The employed measurement setup allows qualitative investigations of electronic configurations prone to $^1\text{O}_2$ attack. The results show that all investigated dyes are attacked by $^1\text{O}_2$ in their ground state. **In fact, the attack of the ground state by $^1\text{O}_2$ is the main contributing process to photodegradation in all dyes.** The influence of the excited state on photostability strongly depends on the dye structure and differs in the investigated dyes. However, even when the excited state is attacked by $^1\text{O}_2$, this process doesn't contribute as much to photodegradation as the attack of the ground state by $^1\text{O}_2$. In order to draw general conclusions as to which structural characteristics leads to which behaviour, more dyes need to be investigated.

2.4.3 Comparing Photostabilities of various Optical Chemical Sensor Dye Classes in the Ground State

The employed absorption spectroscopy measurement setup explained in 2.2.1 allows comparing the photostability of various different dye classes. The selective irradiation of **A** generates a $^1\text{O}_2$ surplus in solution while **B** remains in the ground state. Figure 2.8 shows observable absorption spectra of **B**. The spectra of **B5** and **B7-10** are not plotted here since their absorption maxima overlap with the Soret-band of **A** and are not selectively visible in the solution spectra. However, the decrease in absorption over irradiation time for these compounds was calculated using matrix deviation methods. All depicted spectra show a decrease in absorption intensity of **B** with irradiation time of **A**. According to the Lambert-Beer law, the absorption intensity is directly proportional to dye concentration (at constant pathlength and ϵ). Consequently, the decrease in absorption intensity over irradiation time directly indicates the decrease in dye concentration due to photodegradation caused by $^1\text{O}_2$ attack. In the case of **B13** (PtC_6) and **B14** (PtOEP), the growing absorption of generated photoproducts is visible in the absorption spectra.

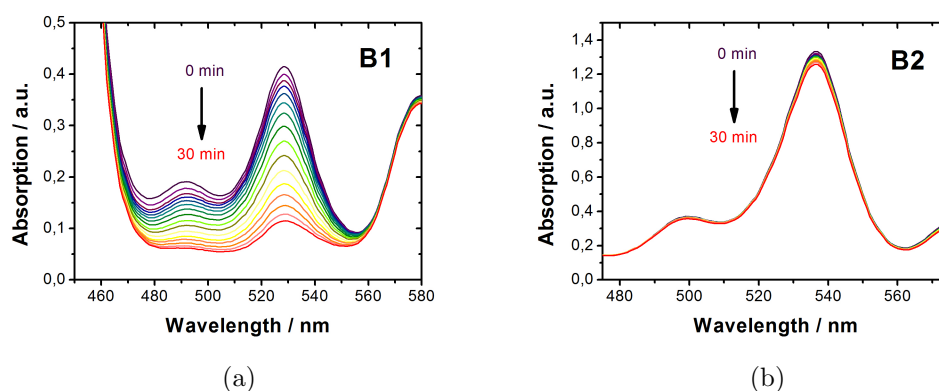
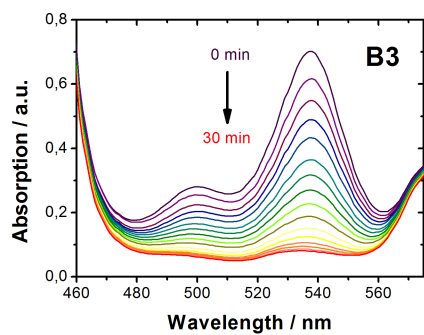
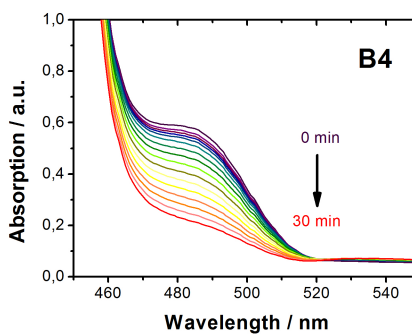


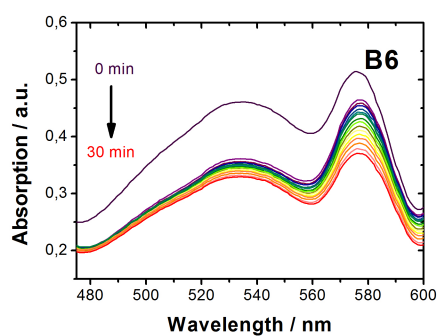
Figure 2.8: Absorption spectra of **B**; Irradiation of **A**: $^1\text{O}_2$ surplus, **B** in ground state. (continued on next page)



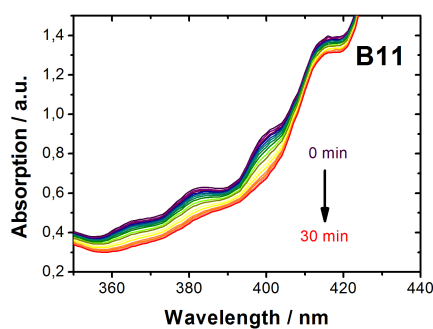
(c)



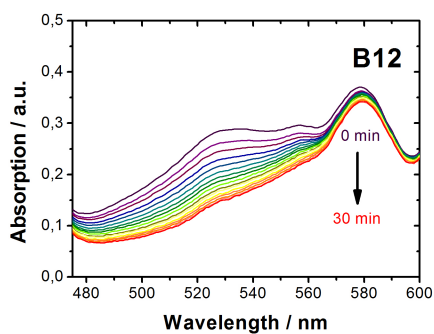
(d)



(e)



(f)



(g)

Figure 2.8: (continued) Absorption spectra of **B**; Irradiation of **A**: $^1\text{O}_2$ surplus, **B** in ground state. (contiued on next page)

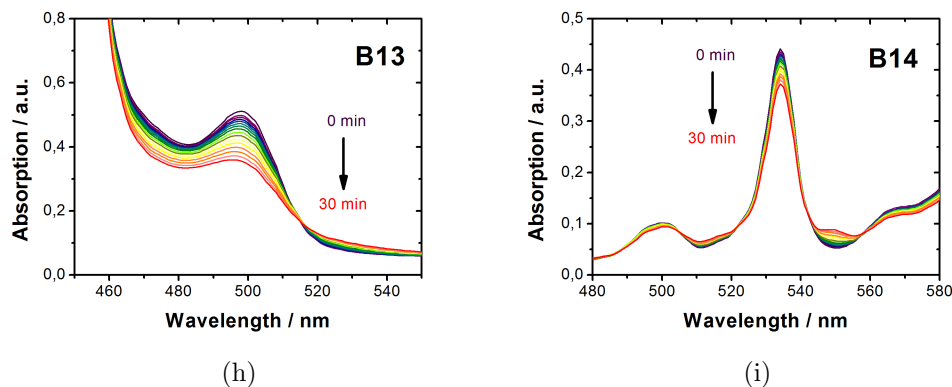


Figure 2.8: (continued) Absorption spectra of **B**; **Irradiation of A**: $^1\text{O}_2$ surplus, **B** in ground state. All spectra show a decrease in absorption intensity, thus a decrease in dye (**B**) concentration with irradiation time of **A**, caused by $^1\text{O}_2$ attack. **B1**, **B13** and **B14** feature absorption bands of photoproducts evolving over irradiation time.

Figure 2.9 shows the relative absorption maximum vs. irradiation time for all investigated dyes **B**. The curves are differently shaped and do not fit the same mathematical function. Therefore, in order to compare photostabilities, it is not sufficient to determine kinetic rate constants. The chosen parameter of comparison in this experiment is the relative dye content after 30 minutes exposure to $^1\text{O}_2$ surplus (irradiation of **A**). This parameter is given in figure 2.10 for every investigated dye **B**. A high parameter value in comparison points to high photostability, respectively.

B1 is Fluorescein ODE, **B2** (2,7-Dichlorofluorescein ODE) and **B3** (2,7-Dihexylfluorescein ODE) are Fluorescein ODE derivatives. Compared to other dye classes, Fluorescein ODE (**B1**) and 2,7-Dihexylfluorescein ODE (**B3**) are most unstable towards $^1\text{O}_2$ attack. The photostability decreases in the order **B2** > **B1** > **B3** (2,7-Dichlorofluorescein ODE > Fluorescein ODE > 2,7-Dihexylfluorescein ODE). The structural unit prone to $^1\text{O}_2$ attack is the conjugated π -system of the xanthene ring. The electron-donating alkyl groups in the 2- and 7-positions of the xanthene ring (**B3**, 2,7-Dihexylfluorescein ODE) strongly destabilize the structure whereas electron-withdrawing substituents such as chlorine atoms in these positions (**B2**, 2,7-Dichlorofluorescein ODE) dramatically improve the structure's stability. These observations are in good agreement with data obtained by Weidgans et al.⁴². Weidgans et al. report similar photostability relations of the very same Fluorescein derivatives in an experiment where the dyes were irradiated.

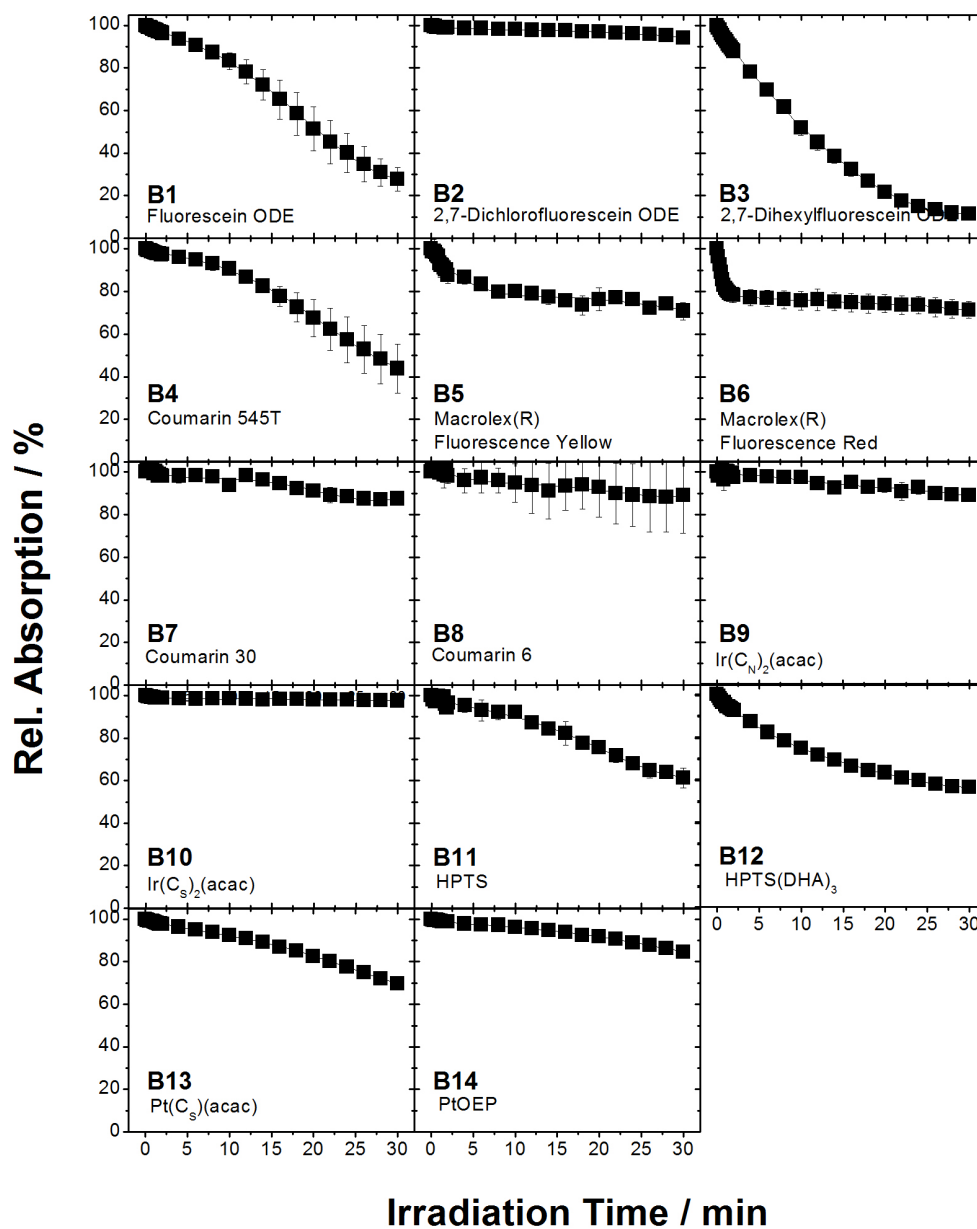


Figure 2.9: Relative absorption maximum of **B** vs. irradiation time, investigating photostability of **B** in the ground state; **Irradiation of A:** $^1\text{O}_2$ surplus, **B** in ground state. In order to compare photostabilities, it is not sufficient to determine kinetic rate constants since the curves are differently shaped and do not fit the same mathematical function.

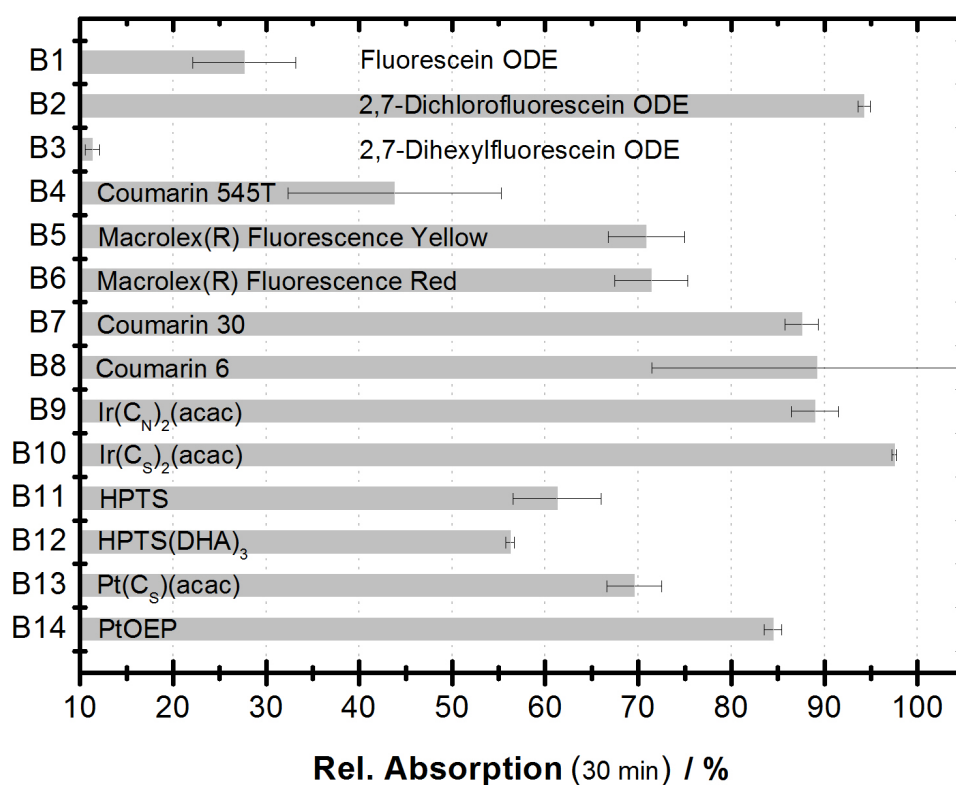


Figure 2.10: Relative absorption maxima after 30 minutes exposure to $^1\text{O}_2$ surplus, investigating photostability of **B** in the ground state; **Irradiation of A**: $^1\text{O}_2$ surplus, **B** in ground state. Absorption intensities are directly proportional to dye concentration in solution. A relatively high dye concentration after 30 minutes exposure to $^1\text{O}_2$ points to high photostability and vice versa, with respect to other dyes investigated. **B1-3**: Fluoresceins; **B4-8**: Coumarins; **B9-10**: Cyclometalated Ir(III) Coumarin complexes; **B11-12**: HPTS derivatives; **B13-14**: Pt(II) complexes.

ated directly and therefore the sole source of photosensitized $^1\text{O}_2$.

B4-8 are Coumarin derivatives. In general, Coumarins are more resistant to $^1\text{O}_2$ attack than Fluoresceins (with the exception of chlorine-substituted **B2**). Coumarin 545T, Macrolex® Fluorescence Red and Coumarin 6 (**B4**, **B6** and **B8**, respectively) feature a benzothiazole structure in addition to the Coumarin entity. The Coumarin structure in these compounds has different substituents: A cyano group in **B6** (Macrolex® Fluorescence Red) and a Julolidine group instead of a diethylamino group in **B4** (Coumarin 545T). Both substituents destabilize the structure, as **B8** (Coumarin 6) is the most stable Coumarin derivative investigated. The Julolidine group is known to be more electron-donating than the diethylamino group, thus destabilizing the π -system in the Coumarin. Macrolex® Fluorescence Yellow (**B5**) features a benzoxazole structure and Coumarin 30 (**B7**) a benzimidazole structure in addition to the Coumarin entity. Although the benzoxazole structure in **B5** carries an electron-withdrawing and therefore stabilizing chlorine substituent, it is less resistant towards $^1\text{O}_2$ attack than **B7**.

$\text{Ir}(\text{C}_N)_2(\text{acac})$ and $\text{Ir}(\text{C}_S)_2(\text{acac})$ (**B9** and **B10**, respectively) are cyclometalated Ir(III) complexes, note that their ligands are Coumarins **B7** (Coumarin 30) and **B8** (Coumarin 6). Interestingly, the metal complexes are more stable towards $^1\text{O}_2$ attack than their respective metal-free ligands. This result could be explained by the electron-withdrawing character of the Iridium atom. However, when applied as single sensor dye, the $^1\text{O}_2$ generation efficiency is higher for metal complexes than for ligands (which produce virtually no $^1\text{O}_2$), since the complexes show efficient phosphorescence and no fluorescence and the quantum yield of the triplet state is expected to be close to unity. An efficient population of the long-lived triplet state strongly enhances the probability of $^1\text{O}_2$ photosensitization. Therefore, under conditions not involving external generation of a $^1\text{O}_2$ surplus, photostabilities of metal complexes might be lower than of their respective metal-free ligands despite their higher resistance to $^1\text{O}_2$ attack. $\text{Ir}(\text{C}_N)_2(\text{acac})$ (**B9**) is significantly less stable than $\text{Ir}(\text{C}_S)_2(\text{acac})$ (**B10**), which might be explained by the lower stability of the benzimidazole structure in the ligand with respect to the benzothiazole structure. This relation is less pronounced in the metal-free ligands, however, the results correlate well with trends in photostabilities obtained previously⁵². In fact, compounds containing imidazole are applied as $^1\text{O}_2$ detection agents, implicating a high reactivity towards $^1\text{O}_2$ ¹²¹.

B11 and **B12** are HPTS and its sulfonamide derivative, respectively. In general, both compounds occupy an intermediate position between Fluores-

ceins and Coumarins on the photostability scale. The aliphatic substituents introduced in the sulfonamide derivative destabilize the structure.

Pt(C_S)(acac) and PtOEP (**B13** and **B14**, respectively) are Pt(II) complexes with octaethylporphyrine and Coumarin6 (**B8**) as ligands, respectively. Note that the same Coumarin derivative is the ligand in cyclometalated Ir(III) complex **B10** (Ir(C_S)₂(acac)). While the Ir(III) metal complex **B10** is more stable than the metal-free ligand **B8**, this is not the case for Pt(II) metal complex **B13**. Also, the Pt(II) Coumarin complex is less stable towards ¹O₂ attack than the Pt(II) octaethylporphyrin complex.

The introduced analytical method allows comparing photostabilities of various optical chemical sensor dye classes. The results demonstrate the importance of ¹O₂ in photodegradation processes and shed a light on structural dye characteristics influencing stability towards ¹O₂ attack. While fluorescent dyes might not generate ¹O₂ as efficiently as introduced phosphorescent metal-ligand complexes upon direct irradiation, they are in general more prone to ¹O₂ attack and therefore even small amounts of ¹O₂ might lead to significant photodegradation of these dyes.

2.4.4 EPR measurements

While $^1\text{O}_2$ is not detectable via EPR, it can be “trapped” by TEMP, giving EPR-active TEMPO. This mechanism is explained in 2.2.2, the triplet EPR signal of TEMPO is given in figure 2.11a. TEMP is highly selective towards $^1\text{O}_2$, accordingly a rise in EPR signal intensity over irradiation time of a photosensitizer (photosensitized generation of $^1\text{O}_2$) is proportional to a rise in $^1\text{O}_2$ concentration (shown in figure 2.11b).

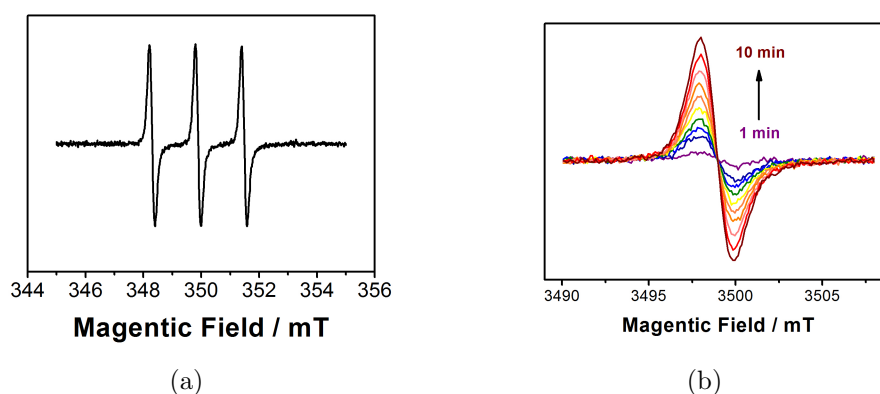


Figure 2.11: EPR spectra of TEMPO: (a) Single EPR spectrum. (b) Central peak evolving during irradiation of **A** ($^1\text{O}_2$ generation), spectra taken every minute for 10 minutes.

The photochemical system in use is the same as in performed absorption spectroscopy experiments. A photosensitizer (**A**) generates a $^1\text{O}_2$ surplus upon selective irradiation. Given that no other compound is present in solution, $^1\text{O}_2$ -trap TEMP reacts with generated $^1\text{O}_2$ giving EPR-active TEMPO. The signal intensity rises over irradiation time, indicating a rise in $^1\text{O}_2$ concentration. This process is depicted in figure 2.11b, showing the increasing central signal peak. If, in addition to **A** and TEMP, an additional dye (**B**) potentially reacting with $^1\text{O}_2$ is present, the rising rate of the TEMPO signal will be altered since TEMP and **B** are competitive reactants for $^1\text{O}_2$.

The results of this experiment set are given in figure 2.12. The parameter representing signal intensity is the relative integral surface of the respective TEMPO EPR spectra, plotted versus irradiation time of **A**. All investigated solutions contain TEMP in the same concentration. Two reference experiments containing (►) only **B3** (2,7-Dihexylfluorescein ODE) and TEMP and (◄) only TEMP without any dyes, show no significant rise in TEMPO

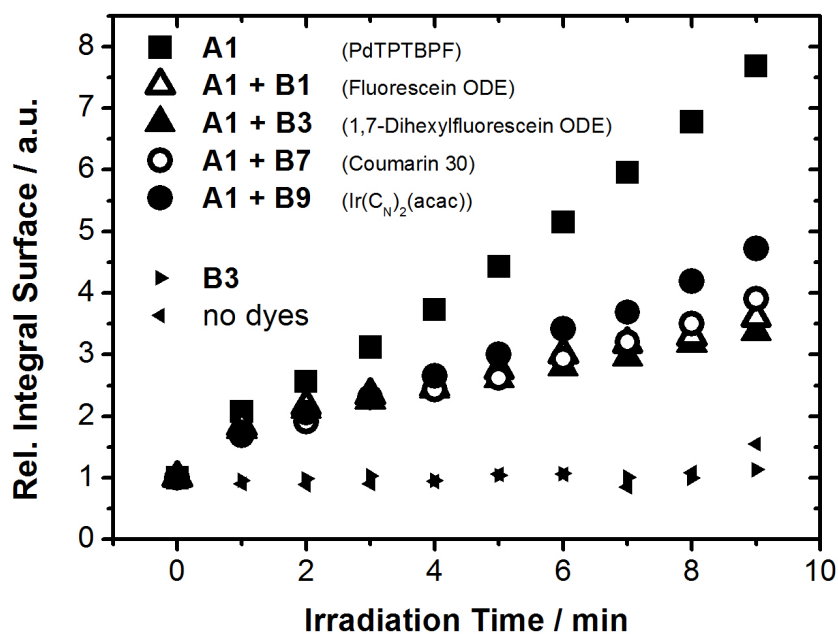


Figure 2.12: Relative integral surface of EPR spectra (of TEMPO) vs. irradiation time of **A**. The rise in relative surface integral of the TEMPO signal is directly proportional to the rise of $^1\text{O}_2$ concentration. All solutions contain TEMP in the same concentrations. In reference experiments with solutions containing TEMP and **B3** or no dye at all, respectively, no $^1\text{O}_2$ is generated. In the solution containing TEMP and **A** (photosensitizer) only, $^1\text{O}_2$ concentration rises almost linear over irradiation time. In the presence of dyes potentially reacting with $^1\text{O}_2$, the slope of concentration curves descends, indicating a reaction of dyes **B** with $^1\text{O}_2$.

concentration over irradiation time. The experiment investigating $^1\text{O}_2$ generation by **A** without additional dyes (■) shows an almost linear rise in TEMPO and thus $^1\text{O}_2$ concentration over irradiation time. All other investigated solutions contained TEMP, **A** and additional dyes **B** (Δ , \blacktriangle , \circ , \bullet). The presence of **B** as potential $^1\text{O}_2$ reactant drastically lowers $^1\text{O}_2$ concentration. The probability of **B** reacting with TEMPO (and not with $^1\text{O}_2$) can be neglected since absorption spectroscopy experiments clearly show a decrease in **B** concentration over irradiation time of **A**, stemming from $^1\text{O}_2$ attack, with no TEMPO present. There is the possibility of **B** acting as a $^1\text{O}_2$ quencher, though. However, when compared to absorption spectroscopy measurements, the here presented data suggests reaction of **B** and $^1\text{O}_2$. The stability of **B** towards $^1\text{O}_2$ attack were found to descent in the order: **B9** > **B7** > **B1** > **B3** ($\text{Ir}(\text{C}_N)_2(\text{acac})$ > Coumarin 30 > Fluorescein ODE > 2,7-Dihexylfluorescein ODE) (results presented in 2.4.3). These findings perfectly correlate with results obtained in EPR experiments. The slope of $^1\text{O}_2$ concentration curves descents in the very same order as the stability of respective **B** dyes towards $^1\text{O}_2$ attack. It should be noted that, comparing **B9** and **B7** ($\text{Ir}(\text{III})$ Coumarin complex $\text{Ir}(\text{C}_N)_2(\text{acac})$ and the respective metal-free ligand Coumarin 30), the relation of stabilities towards $^1\text{O}_2$ attack (figure 2.10) differs from the relation of the respective $^1\text{O}_2$ concentration curve slopes (figure 2.12). The relation of stabilities towards $^1\text{O}_2$ is nearly 1, the metal complex **B9** is only marginally more stable than the metal-free ligand **B7**. The relation of concentration curve slopes in the EPR experiment is clearly > 1 , with the metal complex **B9** altering $^1\text{O}_2$ concentration significantly less than the metal-free ligand **B7**. This discrepancy could be caused by other processes than $^1\text{O}_2$ attack (such as ligand loss) causing photodegradation of **B9**, leading to almost similar photostability as the metal-free ligand **B7**, whereas $^1\text{O}_2$ “consumption” of **B9** is less pronounced than in the case of **B7**.

The described EPR measurements clearly show the importance of $^1\text{O}_2$ in photodegradation processes. With the help of a $^1\text{O}_2$ -trap, $^1\text{O}_2$ could be detected and quantified in a relative manner, pointing to $^1\text{O}_2$ attack majorly contributing to photodegradation in all performed experiments.

2.5 Conclusion

The results obtained leave no doubt concerning the importance of photosensitized $^1\text{O}_2$ in photodegradation processes of optical chemical sensors. The applied method employing a $^1\text{O}_2$ sensitizer generating $^1\text{O}_2$ independently of investigated dyes allows a direct comparison of sensitivities and stabilities of various compounds towards $^1\text{O}_2$ attack. Further, the method is capable of determining the influence of electronic configurations on dye stabilities. The applied EPR measurement technique employing a $^1\text{O}_2$ trap allows tracing reactions of $^1\text{O}_2$ and sensor dyes.

Results of measurements investigating the electronic configuration of optical chemical sensor dyes prone to $^1\text{O}_2$ attack showed that the presence of $^1\text{O}_2$ substantially increases photodegradation of the dyes. All investigated dyes are prone to $^1\text{O}_2$ attack in their ground state, which is the main contributing process to photodegradation in all cases. The influence of the excited state on dye photostability has yet to be clarified in detail since both, a stabilizing as well as a destabilizing effect of the excited state on the overall dye stability towards $^1\text{O}_2$ has been observed for different compounds. To draw general conclusions as to which structural characteristics evoke which effect, more dyes need to be investigated.

Apart from pointing out photostability differences between various dye classes, a comparison of dye stabilities towards $^1\text{O}_2$ attack in the ground state showed that substituents in dye derivatives can have a strong impact on photostability, which has been found before⁴². However, comparing fluorescent compounds to phosphorescent transition metal complexes leads to the general understanding that the latter are more photostable towards $^1\text{O}_2$ attack. Still, in applications irradiating dyes directly, the efficiency for $^1\text{O}_2$ generation has to be taken into account, being much higher for phosphorescent transition metal complexes than for fluorescent compounds. Therefore, when applied as sole sensor dye and directly irradiated, transition metal complexes may be less photostable than fluorescent compounds despite their higher resistance to $^1\text{O}_2$ attack.

Results obtained in EPR experiments reinforce the import role of $^1\text{O}_2$ in photodegradation processes, showing the reaction of independently generated $^1\text{O}_2$ with investigated optical chemical sensor dyes.

In addition to clarifying the substantial contribution of $^1\text{O}_2$ to photodegradation processes, these findings are particularly important for designing sen-

sensor systems containing more than one dye, such as multianalyte sensors⁸⁸ and light harvesting sensor systems^{72,84}, in which different dye stabilities and $^1\text{O}_2$ generation efficiencies cause interfering photodegradation effects.

“Great Maker! Sometimes I feel
I don’t understand anything
anymore.”

LONDO MOLLARI
Babylon 5

Chapter 3

Investigating the Role of Polymers and $^1\text{O}_2$ Quenchers in Photodegradation Processes

3.1 Introduction

The implementation of optical sensing principles in sensor devices (see also 1.2.1) requires immobilizing sensor dyes in a matrix. Polymers are widely used as matrix materials for a broad range of optical chemical sensors^{47,55,93,100}. As discussed earlier in chapter 1, polymers undergo photodegradation processes, a matter broadly and deeply researched and published since the 1960’s^{20,24,26–32}. According to today’s publications and understanding, most photodegradation processes in polymers proceed through photoinitiated radical chain reactions that generate reactive radical species such as hydroperoxides. While $^1\text{O}_2$ may not directly initiate photodegradation chain reactions in polymers, it certainly enhances various mechanisms contributing to photodegradation^{20,29,36}. When applied as matrix material in optical chemical

sensors, polymers may react with embedded dyes³³ and are certainly exposed to higher $^1\text{O}_2$ concentrations than in other applications not involving $^1\text{O}_2$ sensitizers. Under such circumstances, $^1\text{O}_2$ attack might be added to relevant photodegradation mechanisms and further investigated.

Previous work (see section 1.2.4) considering photodegradation processes of optical chemical sensors is focused on dyes only and hardly investigates the role of polymers. The role of polymers in photodegradation processes of optical chemical sensors evolves around two central questions: (1) How stable are different polymers towards $^1\text{O}_2$ attack and (2) How long is the $^1\text{O}_2$ fluorescence lifetime (τ_{SO}) in different polymers? Though these questions might be mechanistically intertwined, they address different problems. First, the stability of polymers towards $^1\text{O}_2$ attack adds up to the overall lifetime of an optical chemical sensor, since photooxygenations in a polymer alter its chemical and physical characteristics needed in optical chemical sensors. Second, τ_{SO} differs depending on the polymer for not only the polymer's reactivity towards $^1\text{O}_2$ but also other physical dimensions such as the diffusion coefficient as a function of solubility and permeability of the gas in the polymer vary. A relatively long τ_{SO} exposes embedded dyes and other additives to $^1\text{O}_2$ for a longer time than a short τ_{SO} , respectively, and therefore enhances the probability of $^1\text{O}_2$ attack.

Considering the important role of $^1\text{O}_2$ in photodegradation processes (elaborated in chapter 2) points towards potentially efficient optical chemical sensor stabilizing strategies¹²². First, avoiding the generation of $^1\text{O}_2$ through avoiding the population of triplet excited states in photosensitizers and second, deactivating $^1\text{O}_2$ by quenching its excited state. The former often is not feasible in optical chemical sensors since populating triplet excited states of photosensitizers in many cases is core of the sensing principle itself, for example in oxygen sensors applying dynamic quenching and the Stern-Volmer relation (see also 1.2.1). The latter, quenching $^1\text{O}_2$, can be achieved by quenchers chemically reacting with $^1\text{O}_2$ (chemical quenching) or quenchers not chemically reacting with $^1\text{O}_2$ but deactivating it through other mechanisms, such as the formation and decomposition of temporary charge-transfer complexes (physical quenching)¹²³. As a stabilizing strategy in optical chemical sensors, physical quenching of $^1\text{O}_2$ is desired.

This section presents investigations on the role of polymers and $^1\text{O}_2$ quenchers in photodegradation processes of optical chemical sensors. Literature suggests a variety of $^1\text{O}_2$ quenchers^{41,79,102–115}, most of which are claimed to be physical quenchers. Selected based on availability and process-

ability, a set of suggested $^1\text{O}_2$ quenchers has been tested by means of $^1\text{O}_2$ luminescence lifetime, oxygen consumption and dye stability measurements.

3.2 Theory & Methods

3.2.1 Total Photon Emission (TPE) by $^1\text{O}_2$ in Polymer Films

The radiative transition from the first electronically excited state of oxygen ($^1\Delta_g$) to its triplet ground state ($^3\Sigma_g^-$) emits a photon ($h\nu$), whose wavelength is 1268 nm¹²⁴. The process of photosensitized generation and radiative deactivation of $^1\text{O}_2$ is schematically shown in figure 3.1. The intensity (I) and lifetime (τ) of the emission decay are quantities accessible by single photon counting techniques since the early 1980's and have constantly been improved for measurements in solution^{125,126}. However, determining τ_{SO} in polymers is a challenge¹²⁷ due to low quantum yields, low signal-to-noise ratio (often caused by photosensitizers emitting in the far IR), microheterogeneity of environments in polymers, etc. Acquired signals often result from complex interactions in the sample and don't allow simplified interpretation. Although attempts to calculate the $^1\text{O}_2$ emission lifetime τ_{SO} have been successful, view experimental data is available¹²⁸⁻¹³⁰. Additionally, interpretation of obtained data needs to consider aspects such as oxygen and $^1\text{O}_2$ quencher concentration, since the meaning of signal rise and decay strongly depends on these factors¹²⁷. Since for investigated polymer films, τ_{SO} could not be determined, the total sum of emitted photons (Total Photon Emission, TPE) by $^1\text{O}_2$ in different polymer matrices containing different $^1\text{O}_2$ quenchers serves as comparable quantity, allowing semi-quantitative interpretation of obtained data.

In order to obtain desired data in different polymers containing different types of $^1\text{O}_2$ quenchers, a $^1\text{O}_2$ sensitizer (**P**) and the $^1\text{O}_2$ quencher (**Q**) are immobilized in a polymer film coated on a carrier Mylar® foil. The probe is then put inside a cuvette and mounted in the measurement system.

3.2.2 Oxygen Consumption in Polymer Films via Optical Oxygen Sensing

Though $^1\text{O}_2$ is argued not to directly initiate photodegradation chain reactions in polymers, it still plays an important role as photooxygenating and in-

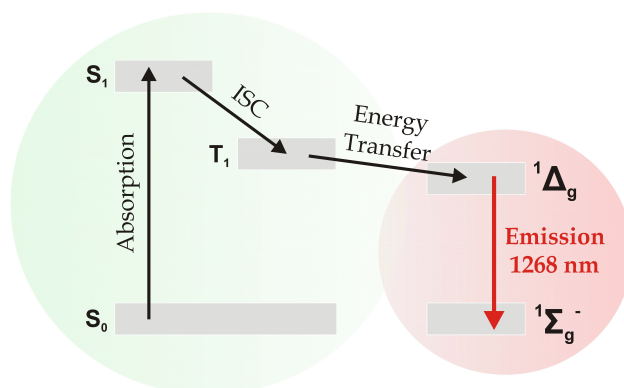


Figure 3.1: Energy diagram showing photosensitized generation and photon emission of $^1\text{O}_2$. The photosensitizer absorbs light and is excited to its first singlet excited state S_1 . Via intersystem crossing (ISC), the triplet state T_1 is populated. In the dynamic quenching process, energy is transferred from the T_1 state of the photosensitizer to the $^1\Delta_g$ state of $^1\text{O}_2$. $^1\text{O}_2$ emits a photon with $\lambda = 1268$ nm.

intermediate chain reaction agent of photodegradation processes^{29,36}. A broad variety of methods are employed to analyse and describe photodegradation processes in polymers^{4,131,132}, one of which is the measurement of oxygen consumption (also referred to as oxygen uptake) by polymers during degradation¹³³. Oxygen uptake can also be measured in various ways, however, to the best of our knowledge, optical chemical sensing of oxygen in polymer films hasn't been applied in this particular manner yet.

The measurement system applied consists of a photosensitizer dye (**P**) serving as optical chemical sensing platform for oxygen via dynamic quenching, a sensing method described in 1.2.1. The photosensitizer is immobilized in a polymer matrix. Further, a $^1\text{O}_2$ quencher (**Q**) is optionally added into the polymer. The polymer is coated as a film on a carrier material, being a Mylar® foil. Additionally, an oxygen barrier is coated on the polymer. The oxygen barrier consists of a polyvinyl alcohol (PVOH) layer, featuring good gas-barrier properties such as low solubility and permeability for low polarity gas molecules such as oxygen^{134,135}.

The photosensitizer dye **P** is irradiated whereat its first excited singlet state S_1 and consequently (through intersystem crossing) its first excited triplet state T_1 are populated. Molecular oxygen present in the polymer film in feasible proximity can now dynamically quench the dye's triplet state.

This process shortens the dye's phosphorescence lifetime τ_{T_1} to a measurable extend, which is the key characteristic for measuring oxygen concentration in the polymer film. During the quenching process, energy transfer from the dye to molecular oxygen leads to a transition from ground state 3O_2 to excited state 1O_2 . Further, 1O_2 may:

- chemically react with the polymer, the photosensitizer dye **P** and/or the 1O_2 quencher **Q**.
- be physically quenched by either, the 1O_2 quencher **Q** or 1O_2 itself (bimolecular quenching,¹³⁶).
- undergo spontaneous radiative or non-radiative (spin-forbidden) transition from it's singlet excited state ($^1\Delta_g$) to it's triplet ground state ($^3\Sigma_g^-$).

In addition to these processes involving 1O_2 , ground state oxygen may also chemically react with one of the components present in the polymer film.

All of the above processes take place solely inside the polymer film. The PVOH oxygen barrier hinders oxygen to diffuse either way, into the polymer film or out of the polymer film. The same is true for the Mylar®carrier foil. Consequently, a detected change in oxygen concentration stems from one or more of the above listed processes. Given that no 1O_2 quencher **Q** is added to the polymer film, in the case of ground state oxygen and/or 1O_2 reacting with one of the compounds present, the oxygen concentration in the polymer film will decrease over time with a characteristic rate. If an 1O_2 quencher **Q** is added to the polymer film, the decrease rate of oxygen concentration might be altered in one of the following ways, indicating different processes:

- The oxygen concentration decreases faster over time than it does with no 1O_2 quencher **Q** present: **Q** either reacts with ground state oxygen or 1O_2 .
- The oxygen concentration decreases more slowly over time than it does with no 1O_2 quencher **Q** present: **Q** physically quenches 1O_2 and "regenerates" ground state oxygen.
- The rate of oxygen concentration decrease is not altered by the presence of a 1O_2 quencher **Q**: **Q** has no measurable effect whatsoever.

The measurement principle is depicted in figure 3.2. The figure features two schemes of the polymer sensor film. Both films are covered with a

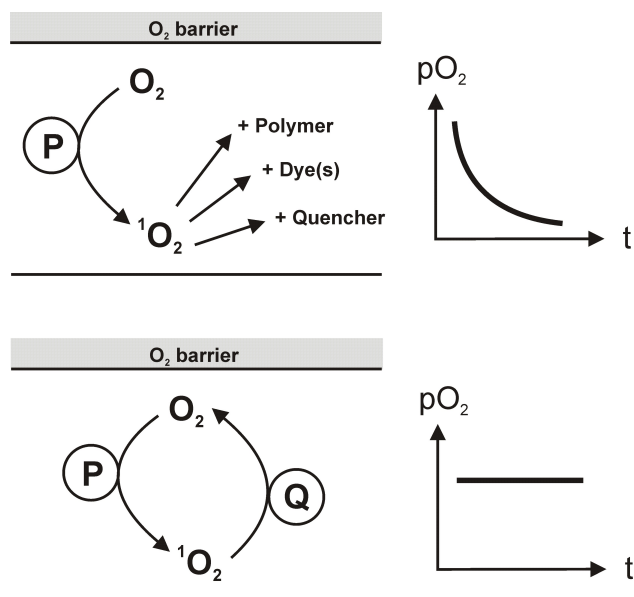


Figure 3.2: Principle of oxygen consumption measurements. Two cases of polymer sensor films are schematically shown. Both films are covered with a PVOH oxygen barrier and contain a photosensitizer dye **P** and oxygen. The lower film additionally contains a $^1\text{O}_2$ quencher **Q**. In both films, $^1\text{O}_2$ is generated upon dynamic quenching of the excited state **P** by oxygen. In the upper film, $^1\text{O}_2$ can react with other compounds present in the film, resulting in a decrease of oxygen concentration over time, schematically shown in the $p\text{O}_2$ vs. time diagram next to the film. In the idealized case of the lower film, $^1\text{O}_2$ is quenched by **Q**, “regenerating” ground state oxygen. Hence, the oxygen concentration is constant over time in this ideal case, provided no other chemical reactions such as between ground state oxygen and the polymer take place.

PVOH oxygen barrier. The upper film contains the photosensitizer dye **P** and oxygen. The lower film additionally contains a $^1\text{O}_2$ quencher **Q**. In both films, $^1\text{O}_2$ is generated upon irradiation of **P**, followed by dynamic quenching of the excited state of **P** by oxygen. In the film containing no $^1\text{O}_2$ quencher, $^1\text{O}_2$ can chemically react with all other compounds present in the film, that is the polymer itself and the photosensitizer dye **P**. The oxygen concentration decreases over time, schematically shown in the $p\text{O}_2$ vs. time diagram next to the film. In the ideal case of the lower film, $^1\text{O}_2$ is quenched by the $^1\text{O}_2$ quencher. Thereby, a transition of excited state $^1\text{O}_2$ to ground state oxygen takes place. If no other reactions described above (e.g. reaction of $^1\text{O}_2$ or oxygen with the quencher or the polymer), the oxygen concentration in the

film does not change over time, since ground state oxygen is constantly “re-generated” by the $^1\text{O}_2$ quencher.

This experimental setup allows comparing different polymers concerning their reactivity towards oxygen and $^1\text{O}_2$ and further enables to distinguish between physical and chemical $^1\text{O}_2$ quenchers and their efficiency. In addition to experiments measuring oxygen uptake by the polymer films, the sensors are characterised (without PVOH gas barrier layer) by the means of Stern-Volmer relation measurements in order to determine whether added $^1\text{O}_2$ quencher alter sensor characteristics such as K_{SV} .

3.2.3 Dye Stability in Polymer Films via Absorption Spectroscopy

Adding a $^1\text{O}_2$ quencher to optical chemical sensor systems for the sake of stabilization towards $^1\text{O}_2$ attack should not only affect the polymer but also the embedded sensor dye. The stabilisation efficiency of different $^1\text{O}_2$ quenchers in different polymers is determined by the means of common photobleaching experiments applying absorption spectroscopy. Accordingly, the measurement system consist of a photosensitizer dye (**P**) and a $^1\text{O}_2$ quencher (**Q**) immobilized in a polymer which is coated as a film on a carrier Mylar®foil. The sensor film is fixed in a transparent glass cuvette which is mounted in an irradiation setup. While constantly irradiated at a resonant absorption wavelength, absorption spectra are frequently taken. Monitoring the absorption maximum of the dye over time allows direct observation of dye concentration. A decrease in absorption intensity over time at constant pathlength and ϵ directly indicates a decrease of dye concentration due to photodegradation. In addition to photobleaching measurements, the sensor is characterized by the means of Stern-Volmer relation measurements before and after irradiation.

This experimental setup allows comparing different $^1\text{O}_2$ quenchers in different polymers considering their stabilisation efficiency towards the dye.

3.3 Experimental

3.3.1 Materials

Photosensitizer Sensor Dyes

Pd(II)meso-tetra(pentafluorophenyl)porphyrin (**P1**) was purchased from Triportech (<http://www.triportech.com/>). Pt(II)meso-tetra(pentafluorophenyl)porphyrin (**P2**) and Pt(II)-2,3,7,8,12,13,17,18-octaethyl-21H,23H-porphyrin (**P3**) were purchased from Frontier Scientific (www.frontiersci.com).

Polymers

Ethylcellulose (EC) (Ethoxyl assay 45.0-46.5%) was purchased from Sigma Aldrich (www.sigmaaldrich.com). Hydrogel D4 (available under the name HydroMedTM) was purchased from AdvanSource biomaterials (www.advbmaterials.com). Poly(methyl methacrylate) and Poly(2,6-dimethyl-p-phenylene oxide) (PPO) were purchased from Scientific Polymer Products, Inc. (<http://scientificpolymer.lookchem.com/abo>). Polystyrene (PS) and Poly(styrene-co-acrylonitrile) (PSAN) were purchased from Acros Organics (www.acros.com). Poly(phenylsilesquioxane) (PSS) was purchased from ABCR (www.abcr.de). Eudragit RL100 (RL) was purchased from Evonic Industries (<http://eudragit.evonik.com>).

$^1\text{O}_2$ Quenchers

1,4-diazabicyclo[2.2.2]octane (DABCO, **Q1**), HexaMethyleneTetrAmine (HMTA, **Q3**), 5,6-benzo-4,7,13,16,21,24-hexaoxa-1,10-diazabicyclo[8.8.8]hexacos-5-ene (Kryptofix 222B, **Q5**), N,N,N-trioctadecylamine (**Q6**), 1,2,2,6,6-pentamethyl-4-piperidinol (**Q7**), 9,10-Anthraquinone (**Q8**) and Duroquinone (**Q9**) were purchased from Sigma Aldrich (www.sigmaaldrich.com).

N-dodecyl-1,4-diazabicyclo[2.2.2]octane tetrafluoroborat (**Q2**) was synthesized by dissolving 1.602 ml dodecylbromide in 50 ml THF. This solution was dropwise added to a solution of 3 g 1,4-diazabicyclo[2.2.2]octane in 50 ml. The solution was stirred for 24 h at 75°C under reflux. The desired product was extracted from the room temperature solution with water, dichloromethane and a surplus of sodiumtetrafluoroborat. The dichloromethane fraction was washed twice with water before the solvent was removed by distillation. The NMR spectrum of this compound can be seen in the appendix of this chapter (figure 3.25).

HMTA stearat (**Q4**, **stearic acid salt of HMTA**) was prepared according to literature⁴⁰. The NMR spectrum of this compound can be seen in the appendix of this chapter (figure 3.25).

¹O₂ Quencher DABCO Covalently Linked to PolyStyrene

The polymer **S1** (and **S3**, respectively, values given in brackets) was prepared as follows: Styrene was purified by filtration through a 3 cm aluminium oxide column. 10 g purified styrol and 0.77 g (0.299 g) chloromethylstyrene were desoxygenated for 30 minutes. 0.166 g (0.1609 g) AIBN was added, the solution was heated and stirred for 6 h at 85°C under Argon atmosphere. The polymerized product was dissolved in dichloromethane and precipitated by adding the 5-fold volume of ethanol dropwise to the stirred solution. The precipitate was filtrated and purified by repeating the dissolving and precipitation step. After filtration, the product was washed twice with methanol and dried. The NMR spectra of the compounds can be seen in the Appendix of this chapter (figures 3.26 and 3.27).

For the preparation of **S2** (and **S4**, respectively, values given in brackets), 0.5 g of **S1**(**S3**) were dissolved in 14 ml dry THF. 0.26 g 1,4-diazabicyclo[2.2.2]octane (DABCO) (0.133 g hexymethylentetramin (HMTA)) were dissolved in 14 ml dry THF. The polymer solution was dropwise added to the DABCO solution. The solution was stirred for 6 h at 50°C under nitrogen atmosphere. After cooling, a sufficient amount of THF was added the room temperature solution so that all compounds dissolved. A solution of 2.6 g (1.0 g) sodium tetrafluoroborate and 75 ml methanol and 75 ml water was added to the stirred solution dropwise. The formed precipitate was filered and purified by repeating the dissolving and precipitation step. Precipitation was enhanced by adding a sufficient amount of sodium chloride to the solution. The solvent was removed by centrifugation and the product was dried. The NMR spectra of these compounds can be seen in the Appendix of this chapter (figures 3.26 and 3.27).

Other

Poly(ethylene glycol terephthalate) support (Mylar®) was purchased from Goodfellow (www.goodfellow.com). All solvents, dodecylbromide, sodiumtetrafluoroborat, styrene, chloromethylstyrene and AIBN were purchased from Sigma Aldrich (www.sigmaaldrich.com).

If not indicated differently, all chemicals were used without further purification.

3.3.2 Measurements

Preparation of Polymer Sensor Films

The “cocktails” for polymer film coating were prepared by dissolving the polymer (13 vol.%, except for D4, 10 vol.% and PSS, 40 vol%) in CHCl_3 . In addition to the polymer, the sensor dye (**P1** and **P2** 1.5 wt.%, **P3** 0.25 wt.% of polymer mass) and - if requested - the $^1\text{O}_2$ quencher (in the corresponding molar ratio P:Q) were dissolved in the sensor cocktail. The cocktails were knife-coated on Mylar® support to give, after solvent evaporation, polymer sensor films 10 μm thick.

For PVOH oxygen barriers, a solution of 10 wt.% PVOH in H_2O was prepared and knife coated onto the polymer sensor film to give, after solvent evaporation, an oxygen barrier 7.5 μm thick.

Total Photon Emission (TPE) by $^1\text{O}_2$ in Polymer Films

The polymer sensor film was diagonally placed in a glass cuvette. The cuvette was mounted in a distance of 50 cm to the irradiation laser (angle laser beam - polymer film surface: 90°) and the detector (angle polymer film surface - detector: 45°). Irradiation laser: Nd:YAG, 532 nm, 50 mW, 2 kHz, the laser beam was widened to a diameter of 2 cm by a lense. Detector: Hamamatsu R5509-42, 1270 nm filter. Further details concerning the measurement setup are described in literature¹³⁷.

Oxygen Consumption in Polymer Films via Optical Oxygen Sensing

Measurements were performed on a dual phase lock-in amplifier (DSP 830, Stanford Research Inc.). Excitation light was obtained from a 525 nm LED (Roithner, www.roithner-laser.com), amplitude 5 V, modulation frequency 5 kHz, time constant 30 ms. Excitation light was filtered by a HQ515/30 longpass filter (Analysentechnik), coupled into one branch of a bifurcated glass fibre bundle (\varnothing 2 mm) and guided to the sensor film. The sensor film was removably fixed on the other end of the bifurcated glass fibre bundle by a transparent silicone gel. Emitted light by the phosphorescent sensor dye was coupled back into the bifurcated glass fibre and guided to the detection entity in the second branch of the glass fibre bundle. Emitted light was filtered through 630 nm bandpass filter (Schott, www.schott.com). The detector was a sensitive PMT module (H5701-02, Hamamatsu, Germany).

Dye Stability in Polymer Films via Absorption Spectroscopy

The polymer sensor film was fixed inside a glass cuvette to a wall of the cuvette by a transparent silicone gel. The glass cuvette was placed in front of the excitation 505 nm LED (operated at 3 W) with a distance of 1 cm from the LED to the sensor film. For absorption spectroscopy measurements, the cuvette containing the sensor film was placed in a Cary 50 UV-VIS spectrophotometer (www.lzs-concept.com).

Calibration (Stern-Volmer) Measurements of the Oxygen Sensors

The sensor film was mounted in a home-made gas-flow device, temperd at 25°C by a Thermo-Haake DC50 cryostat. Gas calibration mixtures were obtained using a gas mixing device (MKS, www.mksinst.com). Phase-angle measurements were performed on a OxyView lock-in amplifier (PreSens, www.presens.de), excitation (505 nm, modulation frequency 4.52 kHz) and emission light guided in a glass fibre from and to the instrument. The glass fibre was mounted at an angle of 90° directly in front of the polymer sensor film.

3.4 Results & Discussion

3.4.1 Choice of Materials

$^1\text{O}_2$ Quenchers

As discussed in section 3.1, literature suggests a large variety of compounds as efficient $^1\text{O}_2$ quenchers. In his review on quenchers of $^1\text{O}_2$, D. Belluš lists and categorizes $^1\text{O}_2$ quenchers most of which are still applied today¹⁰². However, based on up-to-date literature, the $^1\text{O}_2$ quenchers investigated in this work have been selected considering reported effectiveness and processability in optical chemical sensors upon other requirements such as availability. Selected $^1\text{O}_2$ quenchers are given in table 3.1, structures are given in figure 3.3.

Investigations started off with $^1\text{O}_2$ Total Photon Emission (TPE) experiments, testing different $^1\text{O}_2$ quencher classes: DABCO **Q1**, 1,2,2,6,6-pentamethyl-4-piperidinol (which is also applied in polymer stabilization as HAL), 9,10-Anthraquinone and Duroquinone (**Q7-9**). As obtained data (described in 3.4.2) proved 9,10-Anthraquinone and Duroquinone (**Q8 & 9**) to be ineffective $^1\text{O}_2$ quenchers, further investigations focused on DABCO and the piperidinol derivative (**Q1** and **Q7**), disqualifying the latter as chemical $^1\text{O}_2$ quencher in oxygen consumption measurements. As DABCO (**Q1**) proved to be the most effective $^1\text{O}_2$ quencher tested, it was further investigated in dye stability measurements. Due to promising performance of DABCO, further amine $^1\text{O}_2$ quenchers containing tertiary amines or ammonium groups (**Q2-6**: N-dodecyl-DABCO tetrafluoroborat, HMTA, HMTA stearat, Kryptofix 222B®, N,N,N-trioctadecylamine) have been investigated by means of oxygen consumption measurements.

$^1\text{O}_2$ Quencher DABCO Covalently Linked to PolyStyrene

Since DABCO (**Q1**) was a promising $^1\text{O}_2$ quencher, its $^1\text{O}_2$ quenching ability when being covalently linked to PS was tested. The fact that DABCO possesses a relatively high vapour pressure potentially leads to evaporation of the compound out of the polymer matrix. Hence, DABCO and HMTA were covalently coupled to a polystyrene matrix and also tested in terms of $^1\text{O}_2$ quenching ability. Covalently linking the $^1\text{O}_2$ quenching compounds to the polymer prevents potential leaching and/or evaporation of the $^1\text{O}_2$ quencher out of the polymer. To obtain this DABCO (or HMTA, respectively) modified polymers (**S2** and **S3**), a polymer allowing coupling DABCO (/HMTA) to its main chain had to be synthesized. This precursor polymers (**S1**) are

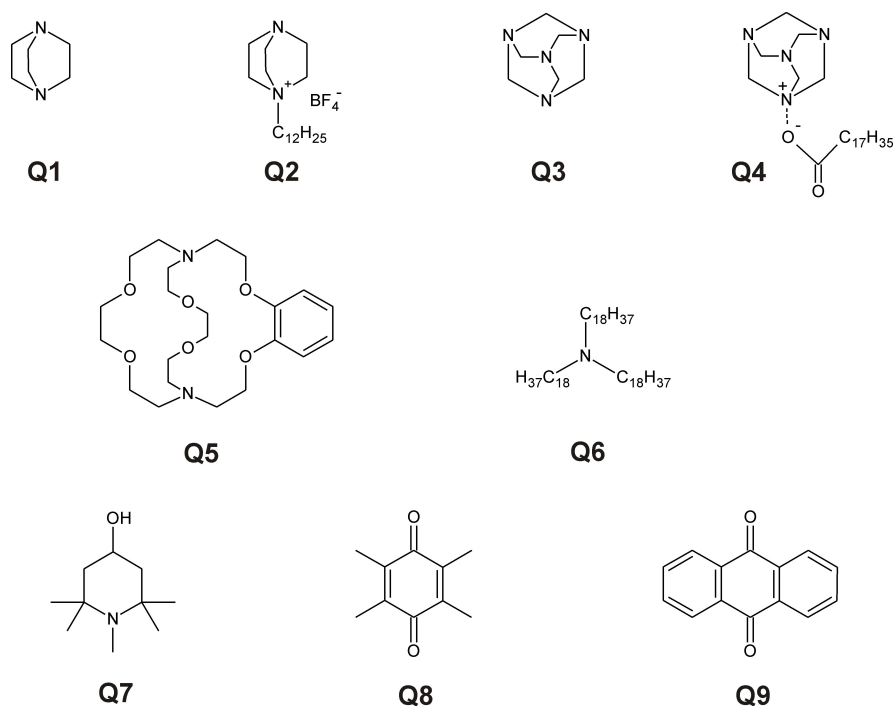


Figure 3.3: Choice of materials: Tested $^1\text{O}_2$ quenchers.

atactic copolymers of 95% styrene and 5% 4-chloromethylstyrene (98% and 2% in the precursor polymer modified with HMTA). The structures of all polymers are given in figure 3.4

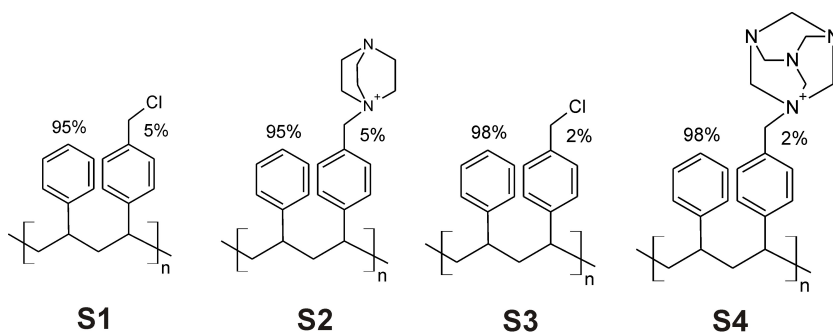


Figure 3.4: DABCO and HMTA covalently linked to polymers. Structures S1-S4.

Table 3.1: Choice of materials: $^1\text{O}_2$ Quenchers.

Abbreviation	Name	Literature
Q1	DABCO (<i>1,4-diazabicyclo[2.2.2]octane</i>)	34,109,111,128,138
Q2	N-dodecyl-DABCO tetrafluoroborat	
Q3	HMTA (<i>HexaMethyleneTetrAmine</i>)	
Q4	HMTA stearat (<i>Stearic acid salt of HMTA</i>)	40
Q5	Kryptofix 222B® (<i>5,6-benzo-4,7,13,16,21,24-hexaoxa-1,10-diazabicyclo[8.8.8]hexacos-5-ene</i>)	
Q6	N,N,N-trioctadecylamine	105,138
Q7	1,2,2,6,6-pentamethyl-4-piperidinol	41
Q8	9,10-Anthraquinone	113
Q9	Duroquinone	113

Photosensitizers

The photosensitizer dyes were chosen based on physicochemical requirements. Names and abbreviations are given in table 3.2. Available structures are given in figure 3.4.1.

Table 3.2: Choice of materials: Photosensitizers.

Abbreviation	Name
P1	PdTPFP <i>Pd(II)meso-tetra(pentafluorophenyl)porphyrin</i>
P2	PtTPFP <i>Pt(II)meso-tetra(pentafluorophenyl)porphyrin</i>
P3	PtOEP <i>Pt(II)-2,3,7,8,12,13,17,18-octaethyl-21H,23H-porphyrin</i>

Polymers

The polymers tested in this work represent currently used matrix materials in optical chemical sensors^{55,93,100}. Names and abbreviations are given in

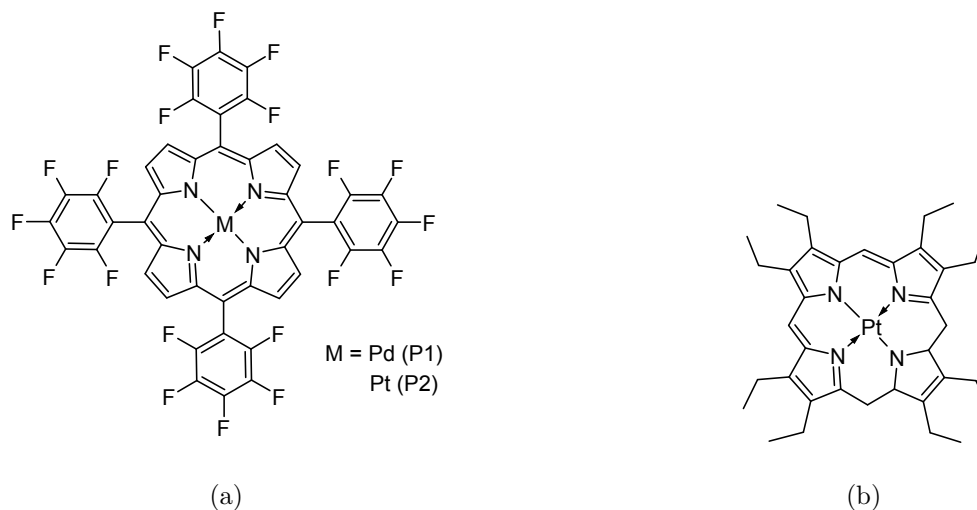


Figure 3.5: Employed photosensitizers. (a) **P1**: PdTPFPF, **P2**: PtTPFPF, (b) **P3**: PtOEP.

table 3.3. Available structures are given in figure 3.6.

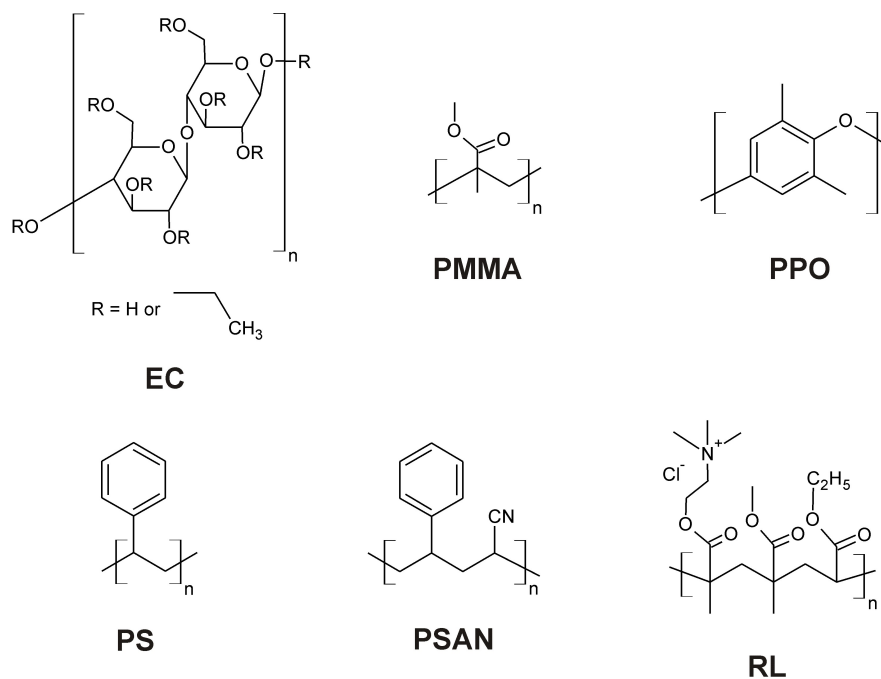


Figure 3.6: Choice of materials: Tested Polymers.

Table 3.3: Choice of materials: Polymers.

Abbreviation	Name	Polymer Class ¹⁰¹
D4	Hydrogel D4	Polyurethanes
EC	Ethylcellulose	Carbohydrate polymers
PMMA	Poly(methyl metacrylate)	Metacrylate polymers
PPO	Poly(2,6-dimethyl-1,4-phenylene oxide)	Polyether engineering thermoplastics
PS	Polystyrene	Vinyl polymers
PSAN	Poly(styrene-co-acrylonitrile)	Copolymer
PSS	Poly(phenylsilesquioxane)	Polysiloxanes
RL	Eudragit RL100	Ammonio methacrylate copolymer type A

3.4.2 Testing Different $^1\text{O}_2$ Quencher Classes in Different Polymers

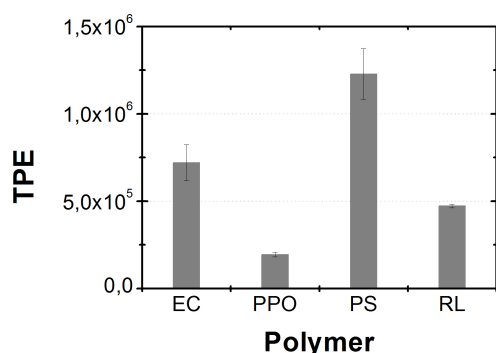
As discussed in section 3.4.1, investigations of potential $^1\text{O}_2$ quenchers started off with testing different $^1\text{O}_2$ quencher classes in different polymers by the means of $^1\text{O}_2$ Total Photon Emission (TPE) and oxygen consumption measurements. The applied methods are described in section 3.2. The tested compounds were DABCO, 1,2,2,6,6-pentamethyl-4-piperidinol (which is also applied in polymer stabilization as HAL), 9,10-Anthraquinone and Duroquinone (**Q1**, **Q7**, **Q8** and **Q9**, respectively; structures are given in figure 3.3). TPE measurements proved 9,10-Anthraquinone and Duroquinone to be ineffective $^1\text{O}_2$ quenchers, therefore DABCO and the piperidinol derivative (**Q1** and **Q7**) were further investigated by the means of oxygen consumption measurements.

Total Photon Emission (TPE) by $^1\text{O}_2$ in Polymer Films

Since for investigated polymer films, τ_{SO} could not be determined (discussed in section 3.2.1), the total sum of emitted photons (Total Photon Emission, TPE) by $^1\text{O}_2$ in different polymer matrices serves as comparable quantity. Results for polymers not containing $^1\text{O}_2$ quenchers are depicted in figure 3.7. Unfortunately, polymer samples **D4**, **PMMA**, **PSAN** and **PSS** didn't produce processable results.

When comparing total photon emissions, factors influencing this parameter need to be considered:

- The permeability coefficient for oxygen in the polymer dictates the overall oxygen concentration and therefore availability for photosensitized $^1\text{O}_2$ generation in the polymer film.
- The reactivity of the polymer towards oxygen and $^1\text{O}_2$.
- The physical $^1\text{O}_2$ quenching ability of the polymer.



The TPEs of **EC**, **PPO** and **PS** decrease in the order: **PS** > **EC** > **RL** > **PPO**. This experiment does not allow a distinction as to which extend each of the factors described above influences the TPE. However, when investigating $^1\text{O}_2$ quenchers, the TPE parameter is of higher significance.

Figure 3.7:

Figures 3.8 and 3.9 depict results of TPE measurements of polymer films containing $^1\text{O}_2$ quenchers DABCO (**Q1**), 1,2,2,6,6-pentamethyl-4-piperidinol (**Q7**), 9,10-Anthraquinone (**Q8**) and Duroquinone (**Q9**). Figure 3.8 features four graphs, each depicting results for one polymer containing DABCO (**Q1**) in different molar ratios with reference to the photosensitizer dye **P1**. The molar ratio (**P1:Q1**) spans from **1:0** to **1:200**. Obviously, TPE decreases with increasing DABCO concentration in all four investigated polymers. As the effect of DABCO on oxygen permeability and solubility in the polymer is considered to be negligible, the observed behaviour can only be ascribed to DABCO quenching the excited state $^1\text{O}_2$. Though the effect is pronounced to a different extend in different polymers, molar ratios of **P1:Q1** = **1:10** and higher are concluded to be effective in all investigated polymers. The option of DABCO eventually quenching the triplet state of the photosensitizer dye **P1** itself has been tested by the means of phosphorescence lifetime measurements and been discarded for τ_{T1} of **P1** is altered to a negligible extend by the presence of DABCO (Under N_2 atmosphere, in PS containing only **P1** τ_{T1} = 892.5 μ s; containing **P1** and DABCO in the molar ration 1:10 τ_{T1} = 681.9 μ s).

Figure 3.9 features four graphs, each depicting results for one polymer containing **Q7-9** (1,2,2,6,6-pentamethyl-4-piperidinol, 9,10-Anthaquinone and

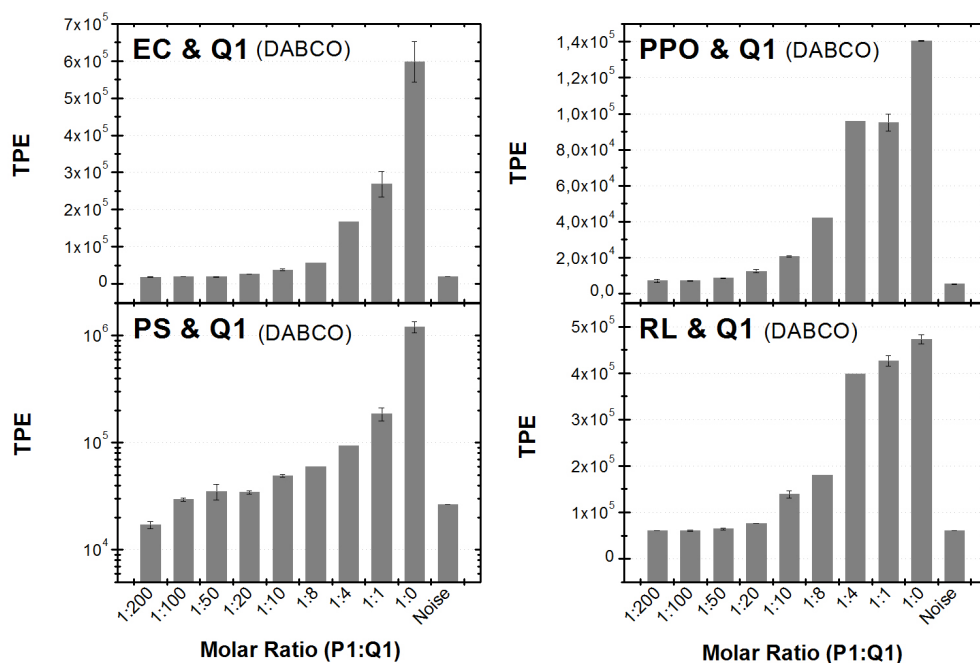


Figure 3.8: Total Photon Emission (TPE) of $^1\text{O}_2$ in investigated polymers containing $^1\text{O}_2$ quencher DABCO (**Q1**) in different molar ratios with respect to **P1**. TPE decreases with increasing DABCO concentration in all four investigated polymers. The observed behaviour can only be ascribed to DABCO quenching the excited state $^1\text{O}_2$. Molecular ratios **P1:Q1** = **1:10** and higher are concluded to be effective in all investigated polymers.

Duroquinone, respectively). Due to solubility, the molar ratio P1:Q is 1:7 for **Q8** and **Q9** and 1:200 for **Q7**. Obviously, 9,10-Anthraquinone and Duroquinone do not alter the TPE compared to TPE of polymer films containing no $^1\text{O}_2$ quencher. Accordingly, the excited state $^1\text{O}_2$ is not quenched by these agents. On the contrary, 1,2,2,6,6-pentamethyl-4-piperidinol alters the TPE drastically compared to TPE of polymer films not containing $^1\text{O}_2$ quenchers and therefore can be considered an effective $^1\text{O}_2$ quencher.

Although the obtained results do not allow a distinction between physical and chemical $^1\text{O}_2$ quenchers, they prove quenchers DABCO (**Q1**) and 1,2,2,6,6-pentamethyl-4-piperidinol (**Q7**) to drastically decrease $^1\text{O}_2$ TPE in all investigated polymers and therefore are worth to be further investigated.

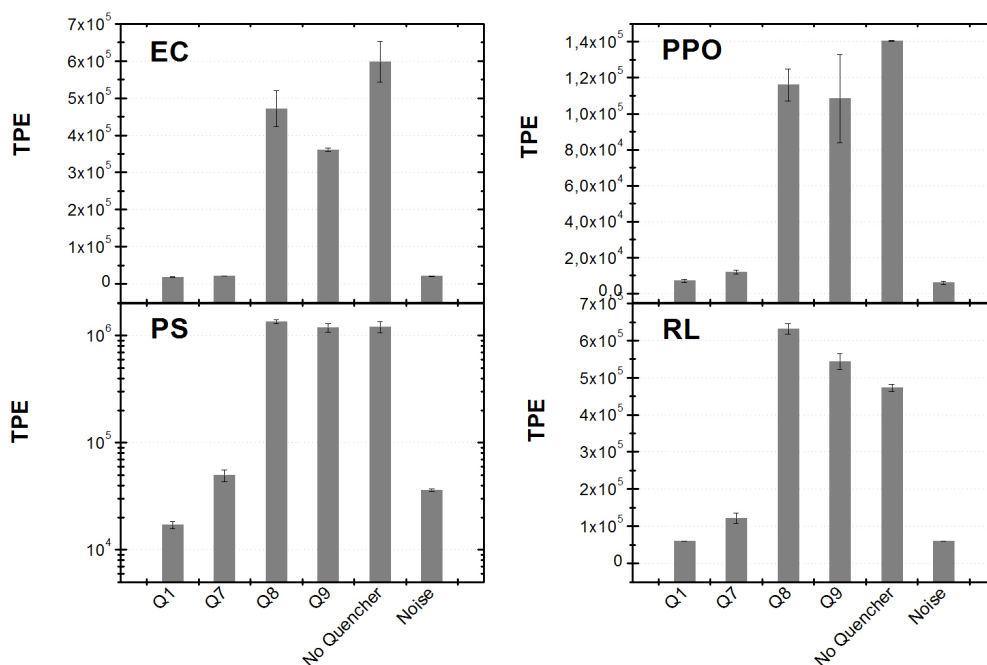


Figure 3.9: Total Photon Emission (TPE) of $^1\text{O}_2$ in investigated polymers containing $^1\text{O}_2$ quenchers 1,2,2,6,6-pentamethyl-4-piperidinol (**Q7**), 9,10-Anthraquinone (**Q8**) and Duroquinone (**Q9**) (Data of DABCO, **Q1**, is plotted here for comparison). Molar ratio (P1:Q): **Q7** 1:200; **Q8** and **Q9** 1:7. While 9,10-Anthraquinone and Duroquinone do not alter $^1\text{O}_2$ TPE in polymer films, 1,2,2,6,6-pentamethyl-4-piperidinol drastically alters TPE. Therefore, out of the here presented agents, only the piperidinol derivative (aside from DABCO) can be considered an effective $^1\text{O}_2$ quencher.

Oxygen Consumption in Polymer Films Containing DABCO or 1,2,2,6,6-pentamethyl-4-piperidinol

Since TPE measurements disqualified 9,10-Anthraquinone and Duroquinone as $^1\text{O}_2$ quenchers, DABCO and 1,2,2,6,6-pentamethyl-4-piperidinol were further investigated by the means of oxygen consumption measurements.

The polymer films investigated in this experiment series were covered

with a layer of polyvinyl alcohol (PVOH). The PVOH layer serves as an oxygen barrier. The oxygen barrier allows monitoring the oxygen concentration in the polymer film upon irradiation of an immobilized photosensitizer **P** without additional oxygen diffusing into the film. The oxygen concentration in the polymer film is detected via optical oxygen sensing as described in section 3.2.2.

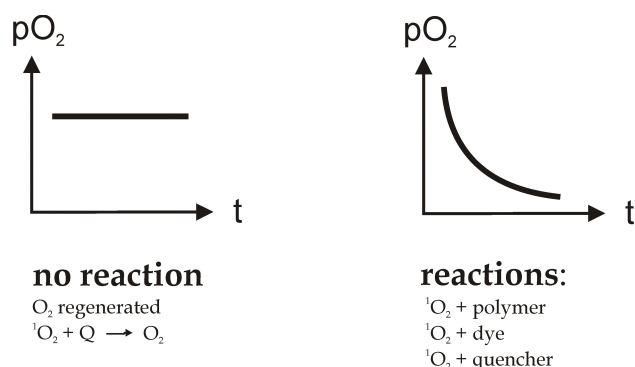


Figure 3.10: Oxygen consumption measurements. Given that no reaction of either ground state oxygen or photosensitized $^1\text{O}_2$ takes place in the film upon irradiation, the oxygen concentration in the film would stay constant over irradiation time. This behaviour indicates constant “regeneration” of O_2 (from photosynthesized $^1\text{O}_2$) via physical quenching. A decrease in oxygen concentration over irradiation time indicates chemical reactions of ground state oxygen or excited state $^1\text{O}_2$ with one of the compounds present: the polymer itself, the photosensitizer **P** or eventually added $^1\text{O}_2$ quenchers **Q**. In this case, there is no physical quenching of $^1\text{O}_2$ taking place.

Given that no reaction of either ground state oxygen or photosensitized $^1\text{O}_2$ takes place in the film upon irradiation, the oxygen concentration in the film would stay constant over irradiation time (as schematically depicted in figure 3.10 on the left side). Due to the oxygen barrier, an increase in oxygen concentration is virtually not possible and would indicate a leaking PVOH oxygen barrier. A decrease in oxygen concentration over irradiation time indicates chemical reactions of ground state oxygen or excited state $^1\text{O}_2$ with one of the compounds present: the polymer itself, the photosensitizer **P** or eventually added $^1\text{O}_2$ quenchers **Q** (as schematically depicted in figure 3.10 on the right side). If the decrease rate of oxygen concentration over irradiation time in polymer films containing no $^1\text{O}_2$ quencher **Q** is altered by the presence of a $^1\text{O}_2$ quencher **Q**, the $^1\text{O}_2$ quencher obviously has one of two effects on oxidative photodegradation processes: (1) The decrease rate

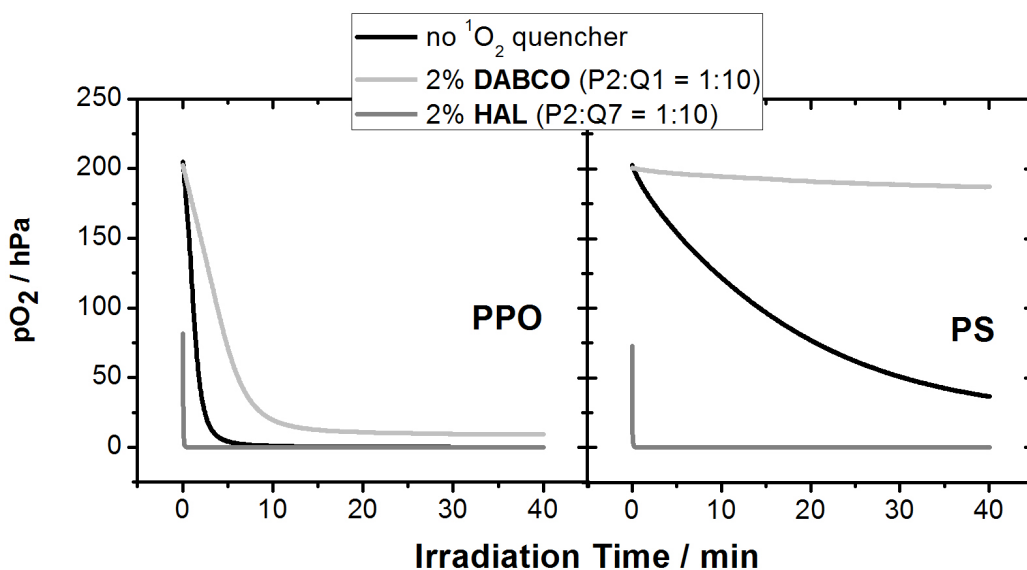


Figure 3.11: Oxygen concentration (pO_2) vs. irradiation time. Each graph shows results for one polymer, PPO and PS. Polymers contain no 1O_2 quencher (black curves), DABCO (**Q1**, light grey curves) or 1,2,2,6,6-pentamethyl-4-piperidinol called “HAL” (**Q7**, dark grey curves) in a molecular ratio of **P2:Q** = **1:10**. pO_2 decreases in all cases over time. Polymers containing the piperidinol derivative show the fastest pO_2 decrease over time, followed by polymer films containing no 1O_2 quencher. This behaviour indicates chemical reactions between 1,2,2,6,6-pentamethyl-4-piperidinol (HAL) and ground state oxygen and/or 1O_2 , respectively. pO_2 decreases slower or almost not at all (PS) in polymer films containing DABCO (**Q1**), thus showing its physical 1O_2 quenching ability.

of oxygen concentration over irradiation time is higher compared to polymer films containing no 1O_2 quencher. This behaviour indicates that in addition to the polymer and **P**, the 1O_2 quencher also chemically reacts with either ground state oxygen or excited state 1O_2 . (2) The decrease rate of oxygen concentration over irradiation time is lower compared to polymer films containing no 1O_2 quencher. This behaviour indicates that the 1O_2 quencher effectively quenches excited state 1O_2 , which is then converted into ground state oxygen.

The parameter obtained in measurements indicating the oxygen concentration is the first triplet excited state lifetime (τ_{T_1}) of **P2** (PtTPFP). As oxygen is detected via dynamic luminescence quenching, an increase of τ_{T_1} indicates a decrease of pO_2 (partial pressure of oxygen, equivalent to oxygen

concentration under standard conditions) and vice versa. The actual $p\text{O}_2$ value can be derived from τ_{T_1} through Stern-Volmer characteristics.

Following the results of TPE measurements (see section 3.4.2), $^1\text{O}_2$ quenchers DABCO (**Q1**) and 1,2,2,6,6-pentamethyl-4-piperidinol (also called “HAL”, **Q7**) were investigated by the means of oxygen consumption measurements. Figure 3.11 shows two graphs, each depicting results for one polymer film, that is, PPO and PS. The graphs plot the oxygen concentration ($p\text{O}_2$) versus irradiation time. In all experiments, $p\text{O}_2$ decreases over irradiation time. The extend to which $p\text{O}_2$ decreases varies in the same way in both polymers. Polymer films containing $^1\text{O}_2$ quencher 1,2,2,6,6-pentamethyl-4-piperidinol (HAL, **Q7**, dark grey curves) show a significantly faster $p\text{O}_2$ decrease than polymer films containing no $^1\text{O}_2$ quencher (black curves). Further, polymer films containing $^1\text{O}_2$ quencher DABCO (**Q1**, light grey curves) show a quite different behaviour: $p\text{O}_2$ decreases slower in PPO and doesn't decrease significantly at all in PS. According to theory elaborated above (see section 3.2.2, this behaviour can only be explained by 1,2,2,6,6-pentamethyl-4-piperidinol chemically reacting with ground state oxygen and/or excited state $^1\text{O}_2$ and DABCO physically quenching $^1\text{O}_2$ to a certain extend in the polymer film, which is especially pronounced in PS. The reaction of 1,2,2,6,6-pentamethyl-4-piperidinol and other HALS with ground state oxygen and $^1\text{O}_2$ has been discussed before^{56,58,139} and is now once again proved to be a reasonable mechanism. DABCO shows to be a physical $^1\text{O}_2$ quencher and therefore is further investigated.

3.4.3 Testing the Performance of DABCO in Different Polymers

The only compound efficiently acting as physical $^1\text{O}_2$ quencher upon all investigated compounds in the previous section (3.4.2) is DABCO (**Q1**). In order to test the performance of DABCO in various concentrations and different polymers, oxygen consumption and dye stability measurements were conducted. Measurement principles are elaborated in section 3.2.

Influence of DABCO Concentration on Oxygen Consumption and Dye Stability

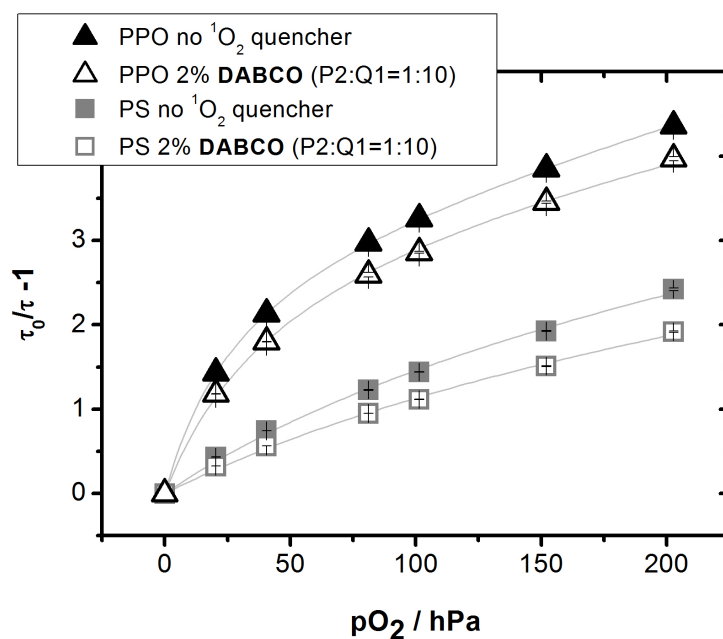


Figure 3.12: Stern-Volmer plots of PPO and PS polymer films containing no $^1\text{O}_2$ quencher and DABCO (**Q1**) in the molar ratio P2:Q1 = 1:10, respectively. The presence of DABCO in the sensor film alters the Stern-Volmer characteristics slightly due to quenching of τ_{T_1} by DABCO.

As can be seen in figure 3.12, DABCO (**Q1**) only slightly alters the SV plots of **P2** in PPO and PS, accordingly, the triplet excited state τ_{T_1} is marginally quenched by DABCO with respect to $^1\text{O}_2$.

The oxygen concentration in polymer films PPO and PS over irradiation time is shown in figure 3.13. The figure features two graphs plotting $p\text{O}_2$

versus irradiation time, each graph showing results for PPO and PS, respectively. The photosensitizer employed in these films is PtTPFPP (**P2**). The molar ratio P2:Q1 ranges from 1:0 (no $^1\text{O}_2$ quencher, black curve) to 1:10 (grey curves). DABCO (**Q1**) does not sufficiently quench $^1\text{O}_2$ in PPO at all, showing in the same zero level of oxygen all curves convert to after 10 minutes irradiation time. Seemingly, processes involving oxygen consumption by PPO are kinetically competing with (and faster compared to) the $^1\text{O}_2$ quenching by DABCO. In the PS plot, the physical quenching action of DABCO is proven by the increasing sustainment of oxygen concentration over irradiation time with increasing DABCO content in the sensor films. This measurement proves DABCO to be a physical $^1\text{O}_2$ quencher in PS, effectively “regenerating” oxygen from photosensitized $^1\text{O}_2$, which would, unquenched, have reacted with one of the other compounds present in the polymer film, thus leading to enhanced photodegradation. Further, the $^1\text{O}_2$ quenching efficiency of DABCO strongly depends on the type of polymer matrix it is immobilized in as well as its concentration.

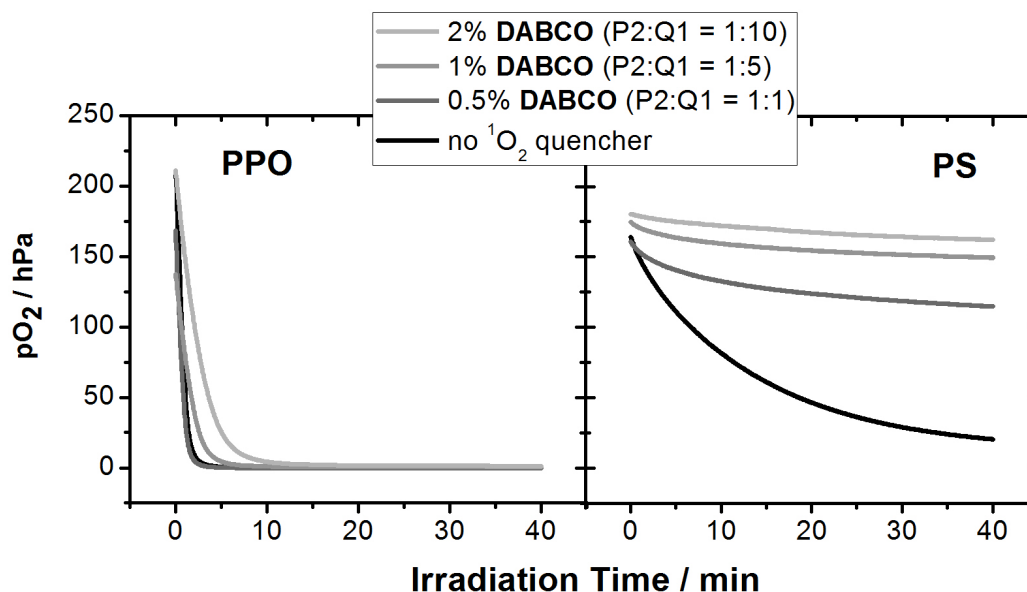
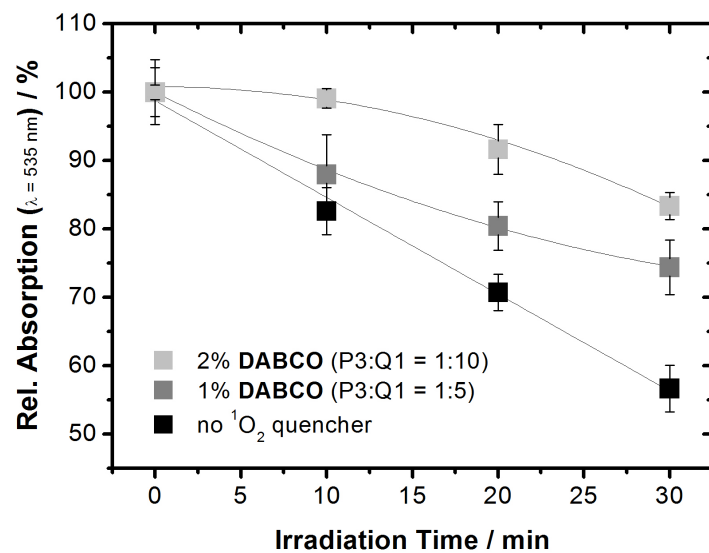
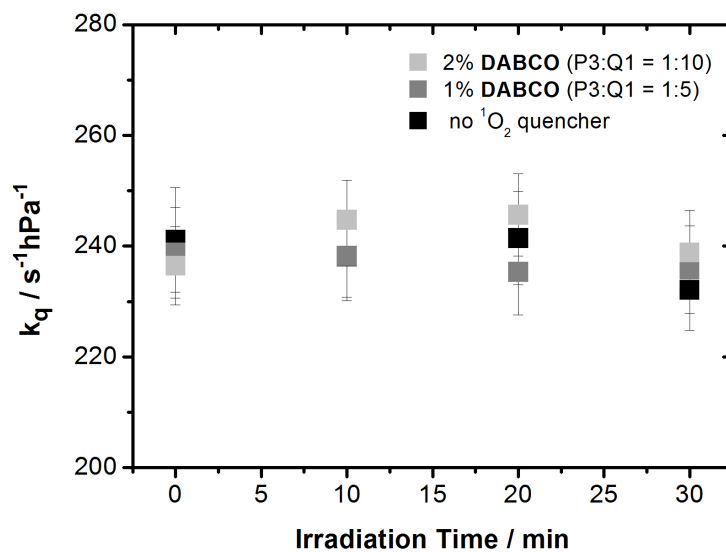


Figure 3.13: Oxygen concentration over irradiation time in polymer films PPO and PS, respectively. The molar ratio of P2:Q1 ranges from 1:0 (no $^1\text{O}_2$ quencher, black curves) to 1:10. DABCO (**Q1**) is shown to have no $^1\text{O}_2$ quenching effect in PPO whereas it serves as highly efficient physical $^1\text{O}_2$ quencher in PS, showing in the increasing sustainment of oxygen concentration over irradiation time with increasing DABCO content. The $^1\text{O}_2$ quenching efficiency of DABCO in PS depends on its concentration.



(a)



(b)

Figure 3.14: Absorption spectra of PS films with varied DABCO (**Q1**) concentration. (a) Relative absorption vs. irradiation time. (b) k_q vs. irradiation time. The stabilizing effect of DABCO strongly depends on its concentration in the sensor film. DABCO does not significantly alter k_q of **P3**.

In order to investigate the stabilizing effect of DABCO towards sensor dyes embedded in the polymer matrix of optical chemical sensor systems, common photobleaching experiments were conducted. Tested sensor films containing photosensitizer **P3** (PtOEP) were irradiated at a sufficient wavelength and absorption spectra were frequently taken over the course of irradiation time. Monitoring the absorption maximum of the dye over time allows direct observation of dye concentration.

Figure 3.14 (a) shows obtained absorption maxima of PtOEP (**P3**) over the course of irradiation time. The graph features three measurement curves, of which the black curve shows data obtained from a sensor film containing no $^1\text{O}_2$ quencher. The grey curves show data obtained from sensor films containing DABCO (**Q1**) in two different molar ratios **P3:Q1**: 1:5 (dark grey) and 1:10 (light grey). Since the relative absorption is directly proportional to dye concentration, the here plotted decrease of the absorption maximum over irradiation time shows the photodegradation of the sensor dye. Comparing photodegradation rates (that is, the steepness of the fitted measurement curves) clarifies that the degree to which the sensor dye is being destroyed by $^1\text{O}_2$ attack strongly depends on DABCO concentration in the sensor film. The relative dye content after 30 minutes irradiation time decreases in the order (**P3:Q1**) = (1:10) > (1:5) > (1:0). Accordingly, the stabilizing effect of DABCO towards the sensor dye depends on its concentration in the polymer film, which is in good agreement with data obtained in oxygen consumption measurements. Figure 3.14 (b) shows k_q of **P3** over irradiation time. This graph shows that k_q is not significantly altered over irradiation time, even when DABCO is present.

Influence of Different Polymers on DABCO Performance as $^1\text{O}_2$ Quencher

Since the $^1\text{O}_2$ quenching efficiency of DABCO obviously depends on the type of polymer matrix it is immobilized in, several polymers were investigated in terms of oxygen consumption and dye stability. Results of oxygen consumption measurements are depicted in figures 3.16 and 3.15. Figure 3.16 shows eight graphs, each plotting $p\text{O}_2$ versus irradiation time for one investigated polymer. Black curves show data obtained from polymer films containing no $^1\text{O}_2$ quencher, grey curves show data obtained from polymer films containing DABCO (**Q1**) in the molar ratio **P2:Q1** = 1:10. Figure 3.15 shows the oxygen concentration after one hour of irradiation time for each polymer containing

no $^1\text{O}_2$ quencher (black bars) and **Q1** (P2:Q1 = 1:10, grey bars). For certain polymers, there is virtually no difference in oxygen concentration after one hour irradiation time between films containing no $^1\text{O}_2$ quencher and films containing DABCO, that is: PMMA, PPO and RL. While in EC and PSAN, the effect of DABCO on oxygen consumption is relatively small, in D4, PS and PSS, it proves to be an efficient physical $^1\text{O}_2$ quencher. Some structural correlations can be made: PMMA and RL are poly metacrylates and in both polymers, DABCO does not have an effect on oxygen consumption upon irradiation. PS and PSAN are structurally related, PSAN carrying an additional acrylonitrile sidegroup obviously destabilizing the polymer against $^1\text{O}_2$ attack since the $^1\text{O}_2$ quenching effect of DABCO is significantly less pronounced in PSAN with respect to PS. In order to draw more structural related stability conclusions, more polymers need to be investigated.

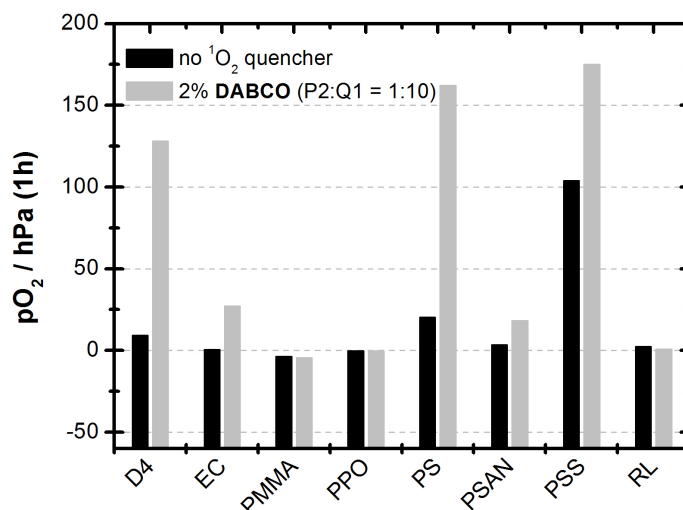


Figure 3.15: Oxygen concentration after one hour irradiation time for different polymers containing no $^1\text{O}_2$ quencher (black bars) and DABCO (**Q1**) in the molecular ratio P2:Q1 = 1:10 (grey bars), respectively.

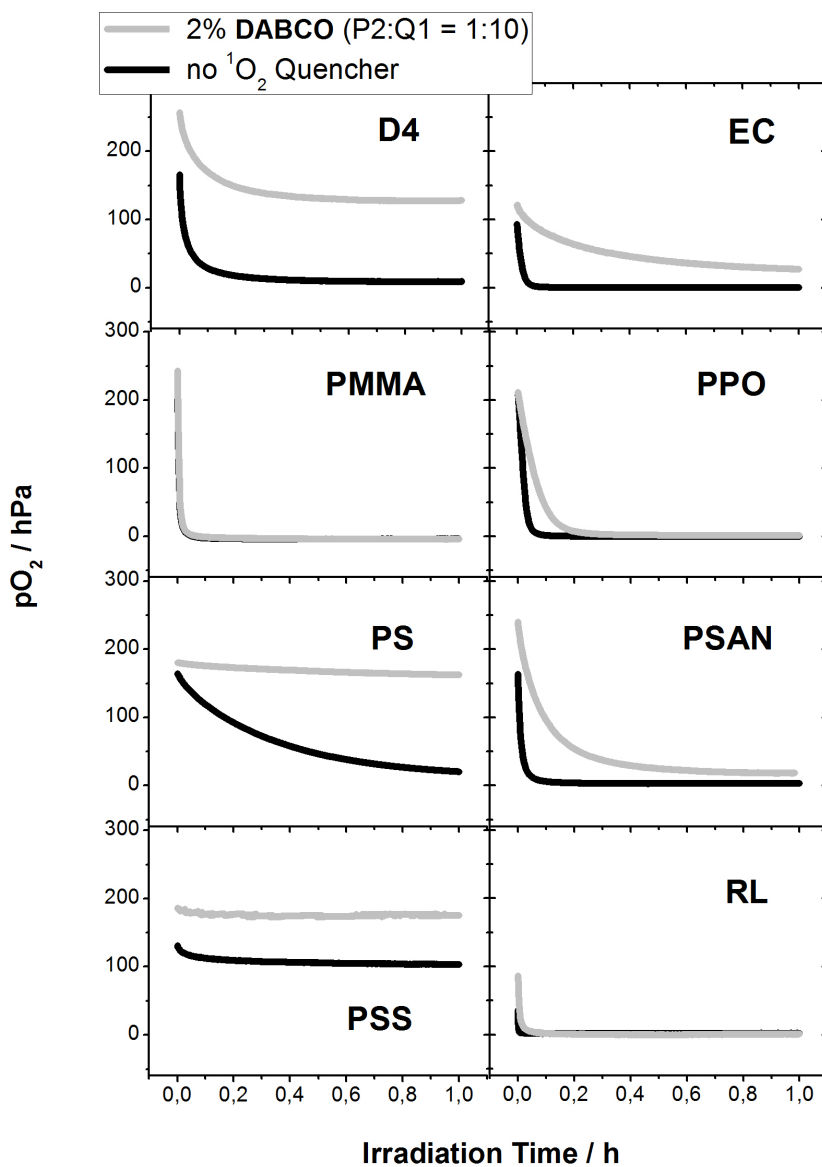


Figure 3.16: $p\text{O}_2$ versus irradiation time for different polymers containing no $^1\text{O}_2$ quencher (black curves) and DABCO (Q1) in the molecular ratio P2:Q1 = 1:10 (grey curves), respectively. The strongest effect of DABCO on oxygen consumption appears in D4, PS and PSS. In PMMA, PPO and RL, DABCO had no measurable $^1\text{O}_2$ quenching effect.

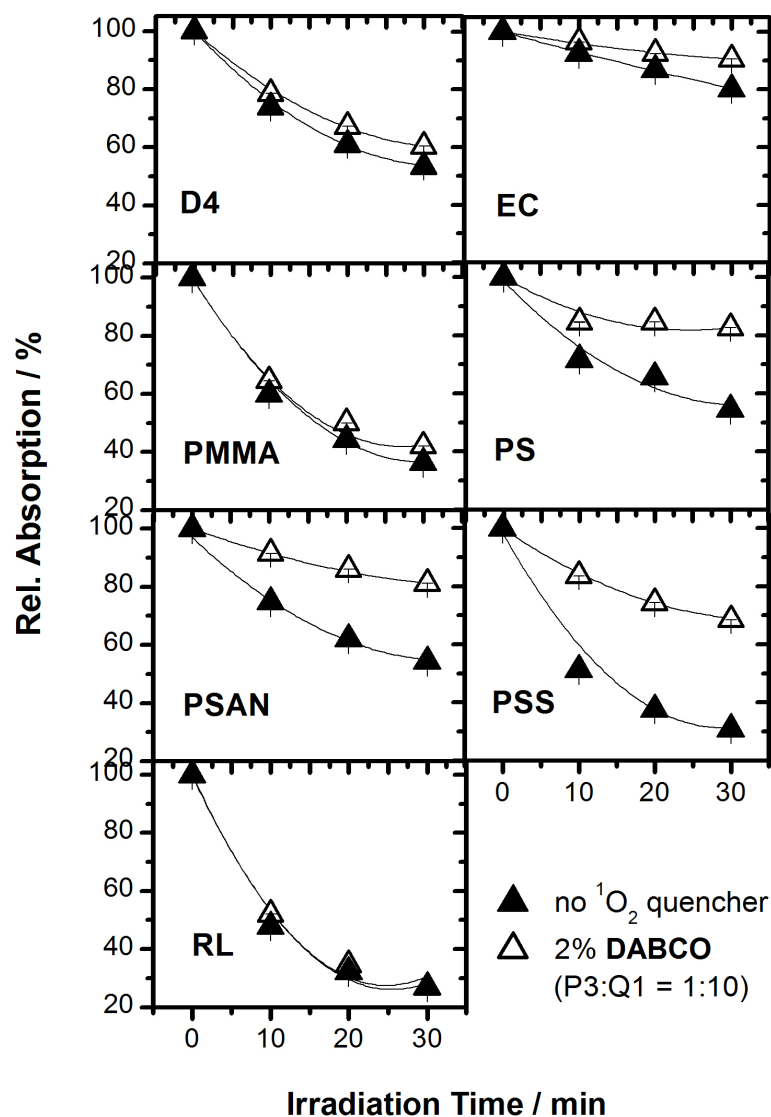


Figure 3.17: Relative absorption maximum of PtOEP (**P3**) versus irradiation time for all investigated polymers. Black triangles show data obtained from polymer films containing no $^1\text{O}_2$ quencher, grey triangles show data obtained from polymer films containing DABCO (**Q1**) in the molar ratio P3:Q1 = 1:10. The relative absorption maximum is directly proportional to dye content. The $^1\text{O}_2$ quencher shows a stabilizing effect on **P3** in all investigated polymers but RL, showing in the steepness difference of dye content decrease curves between grey (containing DABCO) and black (no $^1\text{O}_2$ quencher) triangles. In D4, EC and PMMA, the effect is relatively small with respect to PS, PSAN and PSS. Unfortunately, PPO films didn't give processable results.

Results of photobleaching experiments are depicted in figures 3.17 and 3.18. Figure 3.17 shows seven graphs, each plotting the relative absorption maximum of PtOEP (**P3**) versus irradiation time for one investigated polymer. Black triangles show data obtained from polymer films containing no $^1\text{O}_2$ quencher, grey triangles show data obtained from polymer films containing DABCO (**Q1**) in the molar ratio P3:Q1 = 1:10. Figure 3.18 shows the relative absorption maximum (directly proportional to dye concentration) after thirty minutes of irradiation time for each polymer containing no $^1\text{O}_2$ quencher (black bars) and **Q1** (P2:Q1 = 1:10, grey bars). The $^1\text{O}_2$ quencher shows a stabilizing effect on **P3** in all investigated polymers but RL, showing in the difference between grey (containing DABCO) and black (no $^1\text{O}_2$ quencher) bars. In D4, EC and PMMA, the effect is relatively small with respect to PS, PSAN and PSS. Unfortunately, PPO films didn't give processable results. Partially, these results correlate with results obtained in oxygen consumption experiments shown in figure 3.16: There's no effect of DABCO on oxygen consumption and little effect on dye stability in polymetacrylates PMMA and RL. In EC, both effects are also relatively small with respect to both effects being well pronounced in PS. Results obtained from D4 and PSAN films are inconsistent with oxygen consumption results. While in D4, DABCO has a relatively big effect on oxygen consumption, it's effect on dye stability is rather small. For PSAN, the opposite behaviour is true. These findings may be explained by variations in reactivity of the polymers and photosensitizers **P2** and **P3**, respectively. However, the conclusion of $^1\text{O}_2$ generation and attack as a more or less contributing mechanism to overall photodegradation (in which other reaction mechanisms discussed in chapter 1 are involved) is valid, too. In D4, $^1\text{O}_2$ obviously doesn't contribute substantially to dye lability whereas in PSAN, it ought to be the main source for photodegradation of the sensor dye, since the little amount of $^1\text{O}_2$ quenched by DABCO already shows a big effect concerning the dye stability. As the amount of potential reaction partners for oxygen and $^1\text{O}_2$ in sensor films leads to rather complicated probable and possible reaction kinetics, no quantitative conclusions can be drawn and evolving photodegradation mechanism theories need to be further investigated.

The effect of DABCO on Stern-Volmer plots of PtOEP (**P3**) in different polymers was investigated, too. Figure 3.19 shows two graphs, one plotting K_{SV} , the other k_q for each investigated polymer. Striped bars represent data obtained from sensor films containing no $^1\text{O}_2$ quencher before (black bars) and after (grey bars) 30 minutes irradiation time, filled bars show data obtained from sensor films containing DABCO (**Q1**) in the molar ratio P3:Q1 = 1:10. Both graphs show that the addition of DABCO does not significantly

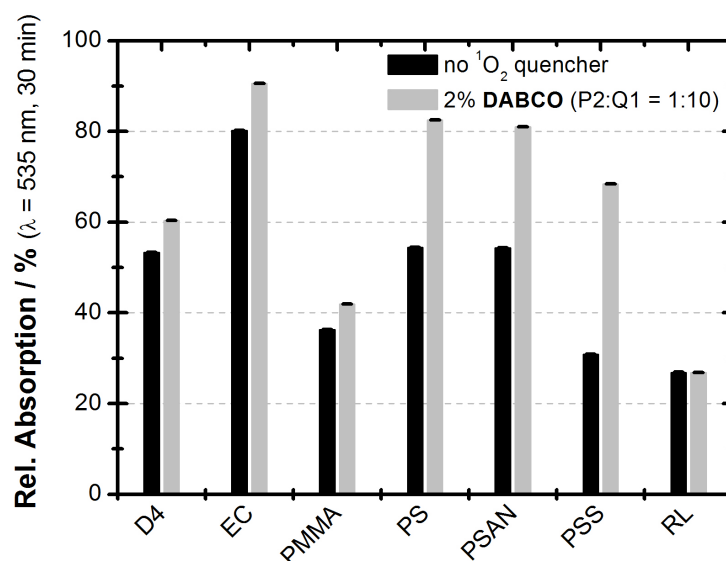


Figure 3.18: Relative absorption maximum (directly proportional to dye concentration) after thirty minutes of irradiation time for each polymer containing no $^1\text{O}_2$ quencher (black bars) and DABCO (**Q1**, P2:Q1 = 1:10, grey bars). The $^1\text{O}_2$ quencher shows a stabilizing effect on **P3** in all investigated polymers but RL, showing in the difference between grey (containing DABCO) and black (no $^1\text{O}_2$ quencher) bars. In D4, EC and PMMA, the effect is relatively small with respect to PS, PSAN and PSS.

effect either K_{SV} nor k_q .

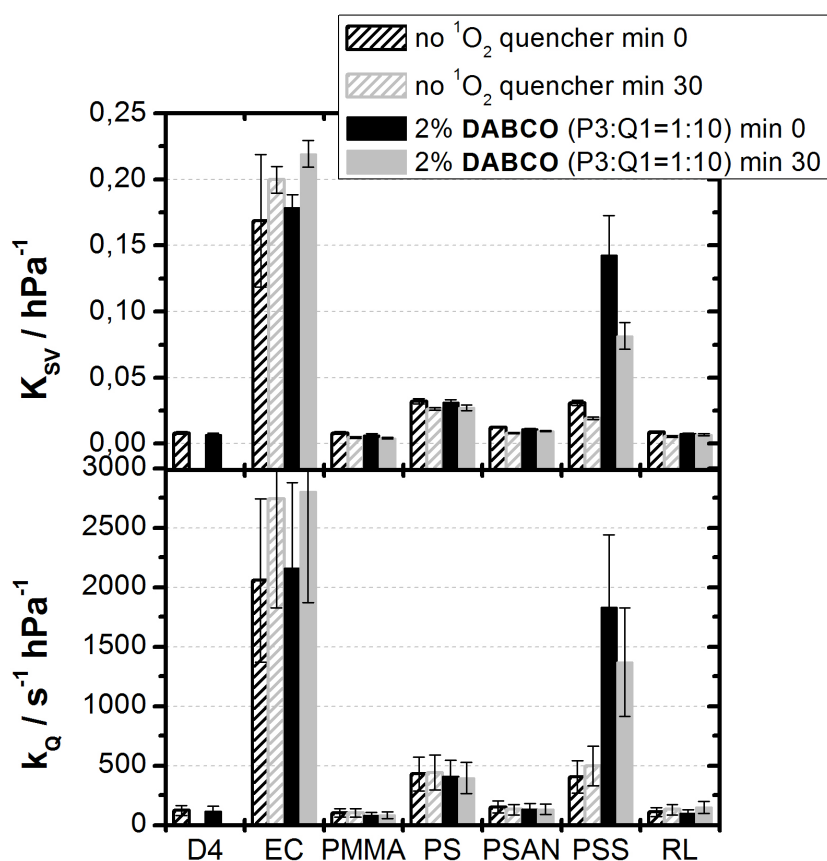


Figure 3.19: K_{SV} and k_q of PtOEP (**P3**) in PS containing no $^1\text{O}_2$ quencher (striped bars) and DABCO (**Q1**) in the molar ratio P3:Q1 = 1:10 (full bars) before (black bars) and after (grey bars) 30 minutes of irradiation. Both parameters are not significantly altered by DABCO over the course of irradiation time.

3.4.4 Investigating further Amino Compounds for $^1\text{O}_2$ Quenching Ability

Among all investigated $^1\text{O}_2$ quenching candidates, DABCO proved to be the only compound sufficiently stabilizing optical chemical sensors. However, DABCO possesses a relatively high vapor pressure and is soluble in water, two features potentially leading to evaporation and/or leaching of the compound out of the polymer matrix. These drawbacks motivate the testing of other tertiary amines for their $^1\text{O}_2$ quenching ability. The compounds investigated are:

- Modified DABCO compound: N-dodecyl-DABCO tetrafluoroborat (**Q2**),
- HMTA (**Q3**),
- Stearic acid salt of HMTA: HMTA stearat (**Q4**),
- Kryptofix 222B[®](**Q5**) and
- N,N,N-trioctadecylamine (**Q6**)

The compounds are depicted in figure 3.20

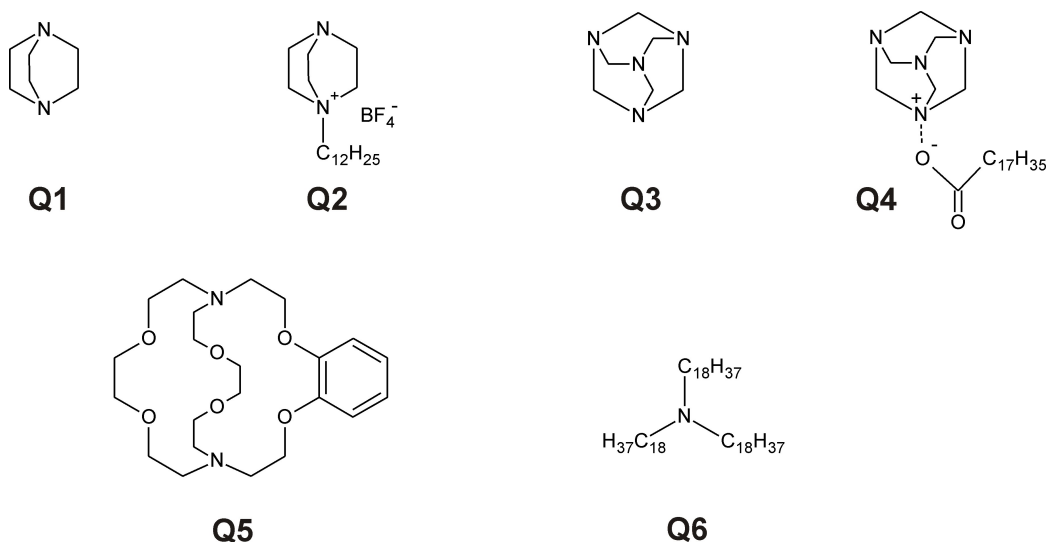


Figure 3.20: Investigated amino compounds for $^1\text{O}_2$ Quenching.

Additionally, DABCO and HMTA were covalently linked to PS and tested. Covalently linking these compounds to a polymer prevents potential leaching and/or evaporation of the $^1\text{O}_2$ quencher out of the polymer. Four polymers were prepared (their structures depicted in figure 3.21): Precursor

polymers **S1** and **S3** are atactic copolymers with the ratios of styrene:4-chloromethylstyrene 95:5 in **S1** and 98:2 **S3**, respectively. Modified polymers **S2** and **S4** contain covalently linked DABCO and HMTA, respectively. Unfortunately, **S3** and **S4** were not processable into sensor films needed for conducted measurements due to solubility issues.

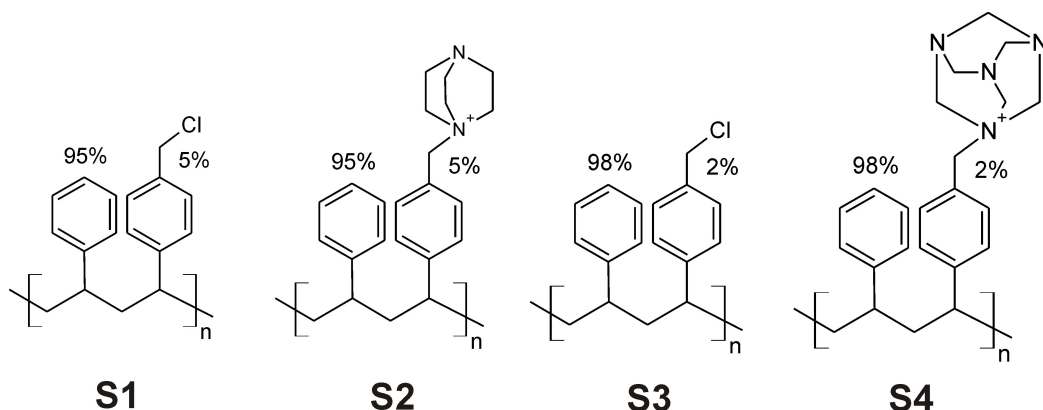


Figure 3.21: DABCO and HMTA covalently linked to polymers. Structures **S1-S4**.

Amino compounds **Q1-6** and modified polymers **S1** and **S2** were investigated by the means of oxygen consumption and dye stability measurements in different polymer films.

Oxygen Consumption Results are depicted in figure 3.22. The first excited triplet state lifetime τ_{T_1} of PtTPFP (P2) serves as parameter indicating oxygen concentration changes. An increase of τ_{T_1} indicates a decrease of oxygen concentration in the polymer film and vice versa. Figure 3.22 features two graphs plotting τ_{T_1} of P2 versus irradiation time for two polymers, EC and PS, each polymer containing $^1\text{O}_2$ quenchers **Q1-6** in the molar ratio P2:Q = 1:10. Curves of polymers containing no $^1\text{O}_2$ quencher are plotted in black. Additionally (featured in the PS plot), results for modified polymers **S1** and **S2** are shown.

In both polymers, all $^1\text{O}_2$ quenchers alter the increase rate and overall oxygen consumption of τ_{T_1} over irradiation time. A faster τ_{T_1} increase over irradiation time in polymer films containing a $^1\text{O}_2$ quencher **Q** with respect to polymer films containing no $^1\text{O}_2$ quencher indicates a chemical reaction of the $^1\text{O}_2$ quencher with ground state oxygen and/or $^1\text{O}_2$. On the contrary, a slower decrease of τ_{T_1} in the same comparison indicates effective physical

$^1\text{O}_2$ quenching, since obviously, oxygen is “regenerated” from photosensitized $^1\text{O}_2$ in the physical quenching process. In EC, this is the case for two investigated $^1\text{O}_2$ quenchers: DABCO (**Q1**) and N-dodecyl-DABCO (**Q2**) (the curve of Kryptofix222B®(**Q5**) also ends at a lower τ_{T_1} than the curve of the polymer film containing no $^1\text{O}_2$ quencher after one hour irradiation time, however, in this measurement, τ_{T_1} first increases to a certain level and then starts to decrease again, indicating a leakage in the PVOH barrier). In PS, all but two tested $^1\text{O}_2$ quenchers or modified polymers, respectively, have a quenching effect on $^1\text{O}_2$ (unfortunately, HMTA stearat (**Q4**) and N,N,N-trioctadecylamine (**Q6**) could not be processed into the polymer films due to poor solubility). Thus, of all investigated $^1\text{O}_2$ quenching agents, DABCO and N-dodecyl-DABCO (**Q1** and **Q2**, respectively) qualify in terms of physical $^1\text{O}_2$ quenching ability as effective $^1\text{O}_2$ quenchers potentially employable as stabilizing agents in optical chemical sensors. Modifying polymer **S1** by covalently linked DABCO yielding in **S2** didn’t lead to the desired effect, much on the contrary, the modified polymer is significantly more prone to oxygen and $^1\text{O}_2$ attack than it’s unmodified equivalent.

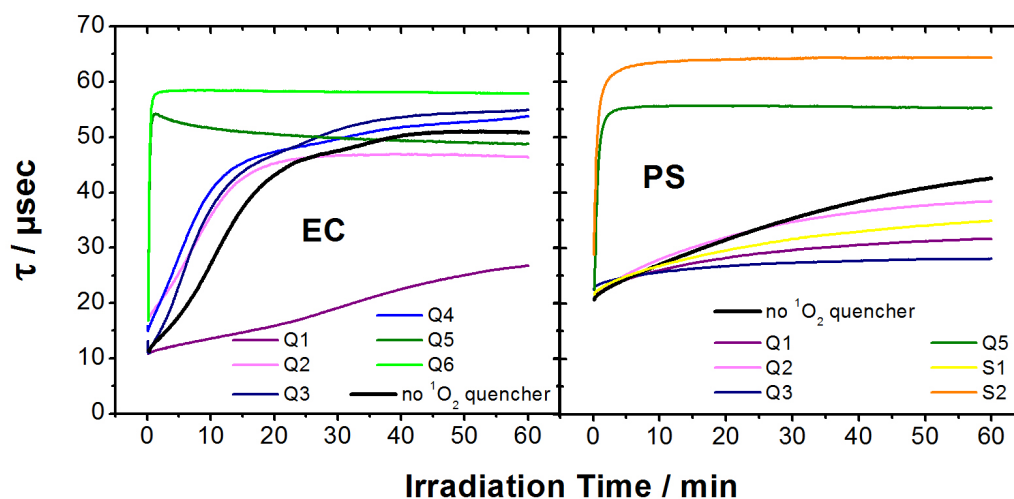


Figure 3.22: τ_{T_1} of PtTPFPP (**P2**) versus irradiation time measured in two polymers, EC and PS, containing different $^1\text{O}_2$ quenchers in the molar ratio P2:Q = 1:10. Black curves are obtained from polymer films containing no $^1\text{O}_2$ quencher. In EC, DABCO (**Q1**) and N-dodecyl-DABCO (**Q2**) are the only effective $^1\text{O}_2$ quenchers whereas in PS, all but two investigated compounds quench $^1\text{O}_2$. Modified polymer **S2** is highly reactive towards oxygen and/or $^1\text{O}_2$.

Dye Stability Results are depicted in figure 3.23, featuring one graph for each polymer. The amount of dye degraded after 30 minutes irradiation time is plotted for each investigated amino $^1\text{O}_2$ quencher. The only $^1\text{O}_2$ quencher significantly lowering photodegradation of PtOEP **P3** is DABCO (**Q1**). These results correlate with data obtained in oxygen consumption measurements (see also figure 3.22).

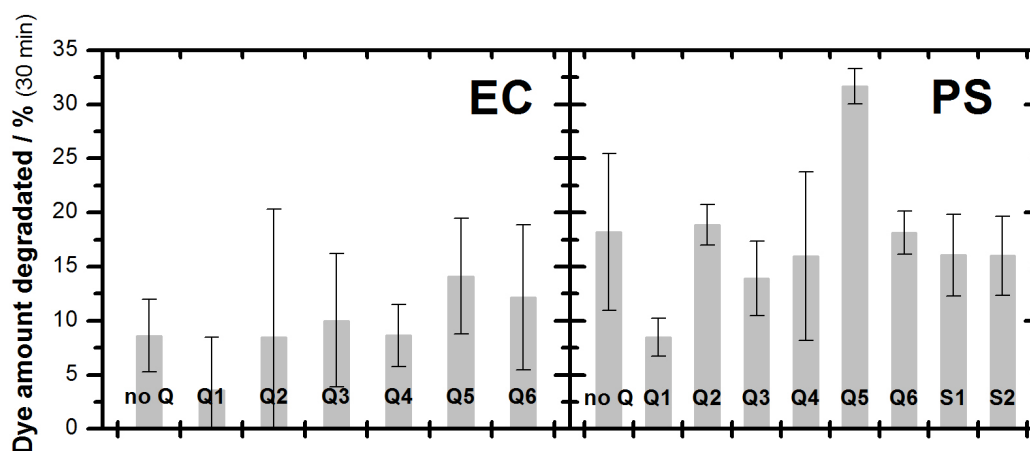


Figure 3.23: Degradated amount of PtOEP (**P3**) after 30 minutes irradiation time in PS and EC, containing different $^1\text{O}_2$ quenchers in the molar ratio P3:Q = 1:10. A stabilizing effect of the $^1\text{O}_2$ quencher shows in lower bars (less dye content degraded after 30 minutes irradiation) than the sensor films containing no $^1\text{O}_2$ quencher. The only $^1\text{O}_2$ quencher showing a stabilizing effect on the sensor dye is DABCO (**Q1**).

Investigating the Volatility of DABCO and N-dodecyl-DABCO in PS

$^1\text{O}_2$ quencher DABCO (**Q1**) possesses a relatively high vapor pressure (0.68 hPa at 21°C), thus the risk of leaching or evaporating (out of the polymer matrix) needs to be considered³⁴. An experiment storing polymer films containing DABCO and N-dodecyl-DABCO (**Q1** and **Q2**, respectively, P2:Q = 1:10) at 60°C for 72 hours investigates the $^1\text{O}_2$ quencher's volatility in the polymer matrix. Results are shown in figure 3.24. τ_{T_1} is plotted versus irradiation time. As in figure 3.22, an increase of τ_{T_1} over irradiation time indicates a decrease of oxygen concentration and vice versa. In both polymer films including $^1\text{O}_2$ quenchers DABCO (**Q1**) and N-dodecyl-DABCO (**Q2**),

the increase of τ_{T_1} is slower and less pronounced resulting in a viewer overall oxygen consumption with respect to the polymer film containing no $^1\text{O}_2$ quencher. In photobleaching experiments, the relative absorption maximum after 30 minutes irradiation time was found to be 94% in a sensor film containing DABCO (**Q1**) in the molar ratio P3:Q1 = 1:10 stored at 60°C for 72 hours while this parameter is 92% for the same sensor film processed under standard experimental conditions (figure 3.23) These results prove that even when stored under harsh conditions for relatively long time, the content of **Q** is still sufficiently quenching $^1\text{O}_2$. However, since shelf-lives of much longer time (in the range of years) are required in most applications, this aspect needs to be investigated in long-term storage experiments.

When comparing the oxygen consumption in PS containing no $^1\text{O}_2$ quencher measured after 1 hour storage at 60°C (curve displayed in figure 3.22) to that measured after 72 hours, the significantly lower rise of τ_{T_1} over irradiation time in the latter curve suggests that thermal conditioning generally improves the stability of the polymer towards $^1\text{O}_2$ attack.

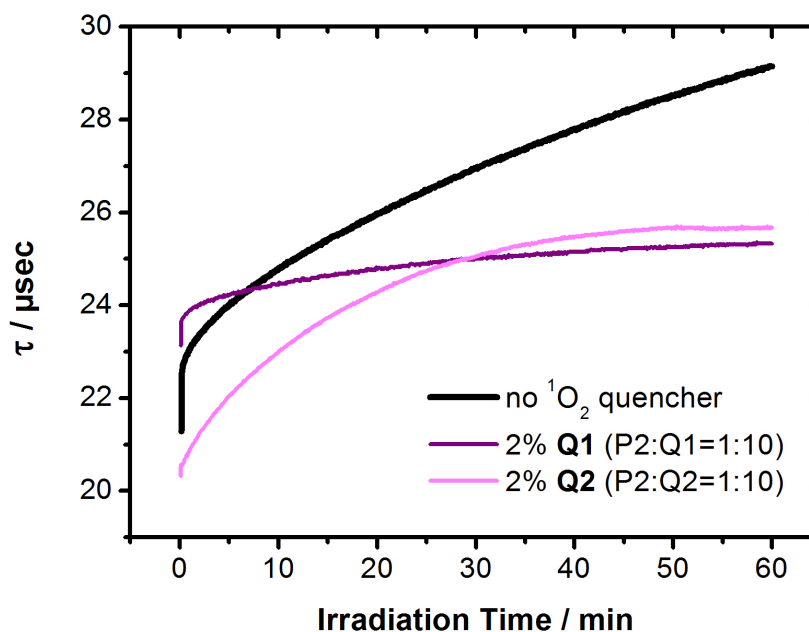


Figure 3.24: τ_{T_1} versus irradiation time for polymer films containing no $^1\text{O}_2$ quencher (black curve), **Q1** (DABCO, dark purple curve) and **Q2** (N-dodecyl-DABCO, light purple curve), respectively. Polymer films have been stored at 60°C for 72 hours. Even when stored under these conditions, **Q1** & **2** serve as physical $^1\text{O}_2$ quenchers.

3.5 Conclusion

In this chapter, investigations on the impact of different polymers and $^1\text{O}_2$ quenchers on photodegradation processes are presented. Investigation methods included measuring the total photon emission (TPE) of $^1\text{O}_2$, the oxygen consumption in the polymer film and the photodegradation of a sensor dye, respectively, in different polymers containing various $^1\text{O}_2$ quenchers.

3.5.1 Polymers

TPE of $^1\text{O}_2$ in different polymers decreases in the order: PS > EC > RL > PPO. However, TPE measurements do not allow to distinguish the as to which parameter mainly contributes to characteristic TPE of $^1\text{O}_2$.

Of all investigated polymers (listed in table 3.3), the effect of DABCO on oxygen consumption decreases in the order: D4 > PS > PSS > EC > PSAN, while virtually no effect was measured for PMMA, PPO and RL. Structurally, two conclusions can be drawn from these measurement series: (1) DABCO does not have an effect on oxygen consumption in polymetacrylates (PMMA and RL). (2) Structurally related PS and PSAN show a different effect of DABCO on oxygen consumption over irradiation time, PSAN obviously being more reactive towards oxygen or $^1\text{O}_2$, respectively. In order to draw more structurally related conclusions, more polymers need to be investigated. Further, oxygen consumption is not only influenced by the polymer structure, reactions of oxygen and $^1\text{O}_2$ in polymers are rather considered to be caused by side groups and impurities left from monomer synthesis and polymerisation processes.

The effect of DABCO on the photodegradation of PtOEP in different polymer matrices was measured by the means of absorption spectroscopy of irradiated sensor samples. The stabilizing effect of DABCO in different polymers decreases in the order: PSS > PS > PSAN > EC > D4 > PMMA. There was no effect whatsoever measured in RL and the effect in PMMA is very small compared to other polymers. The results for polymetacrylates PMMA and RL correlate with results obtained in oxygen consumption experiments, DABCO doesn't have any effect on either, dye stability and oxygen consumption. Oxygen consumption and photobleaching results for PS and PSS are also in good agreement. In contrary to polymetacrylates, the presence of DABCO has a strong impact on oxygen consumption and sensor dye stability in both, PS and PSS. Comparing dye stability measurement

results to oxygen consumption measurement results allow further interesting conclusions: In D4, for example, DABCO has a comparatively big effect on oxygen consumption in the polymer film whereas its effect on dye stability is relatively small with respect to other polymers. Apart from different reactivities of PtTPFPP and PtOEP (**P2** and **P3**, respectively) towards $^1\text{O}_2$ in different polymers, this may also point to the conclusion that in D4, other photodegradation mechanisms than $^1\text{O}_2$ generation and attack mainly contribute to photodegradation of the sensor dye. In PSAN, the opposite behaviour is the case. While DABCO doesn't seem to have a strong effect on $^1\text{O}_2$ consumption, it shows one of the bigger effects in comparison in photobleaching experiments. Accordingly, $^1\text{O}_2$ attack must be one of the main photodegradation mechanisms in PSAN regarding the sensor dye.

The inhomogeneous and varying results of experiments concerning different polymer matrices show the impact the polymer itself has on photodegradation of optical chemical sensors. These results underline the relevance of further investigations of more types of polymers.

3.5.2 $^1\text{O}_2$ Quenchers

Aiming at finding sufficient physical $^1\text{O}_2$ quenchers applicable in optical chemical sensors, a selection of potential $^1\text{O}_2$ quenching agents has been investigated. In TPE measurements, DABCO and 1,2,2,6,6-pentamethyl-4-piperidinol showed to be the most promising candidates, all other tested compounds had no quenching effect whatsoever on $^1\text{O}_2$.

DABCO and 1,2,2,6,6-pentamethyl-4-piperidinol were further investigated in oxygen consumption experiments, where 1,2,2,6,6-pentamethyl-4-piperidinol disqualified as being highly chemically reactive towards $^1\text{O}_2$ rather than a physical $^1\text{O}_2$ quencher. Varying the concentration of DABCO in PS and PPO showed that both, the concentration of the $^1\text{O}_2$ quencher as well as the type of polymer matrix influence the desired $^1\text{O}_2$ quenching effect significantly.

DABCO is a bridged tertiary diamine featuring a unique structure which lays the grounds for theories about the physical $^1\text{O}_2$ quenching mechanism of the compound. This mechanism is believed to be a charge-transfer mechanism, first reported by Ouannes & Wilson¹⁰⁹ and ever since cited in the majority of publications about DABCO as $^1\text{O}_2$ quencher^{105,107,111,138}. As the proposed $^1\text{O}_2$ quenching charge-transfer-complex mechanism between $^1\text{O}_2$

and the amino group is based on the geometrically exposed N-lone pair, other amines and derivatives of DABCO have been investigated as well. Additionally, DABCO was covalently bound into a PS polymer and also tested.

While in oxygen consumption experiments, DABCO and N-dodecyl-DABCO proved to efficiently quench $^1\text{O}_2$ in EC and PS, DABCO was the only component showing a significant stabilizing effect on the sensor dye in photobleaching experiments. Obviously, DABCO provides a unique structure allowing for a charge transfer complex to build with $^1\text{O}_2$ and it's kinetically sufficient dissociation. It is a cost-effective compound, easily processable into polymer sensor films and therefore potentially applicable as stabilizing agent in optical chemical sensors.

3.6 Appendix

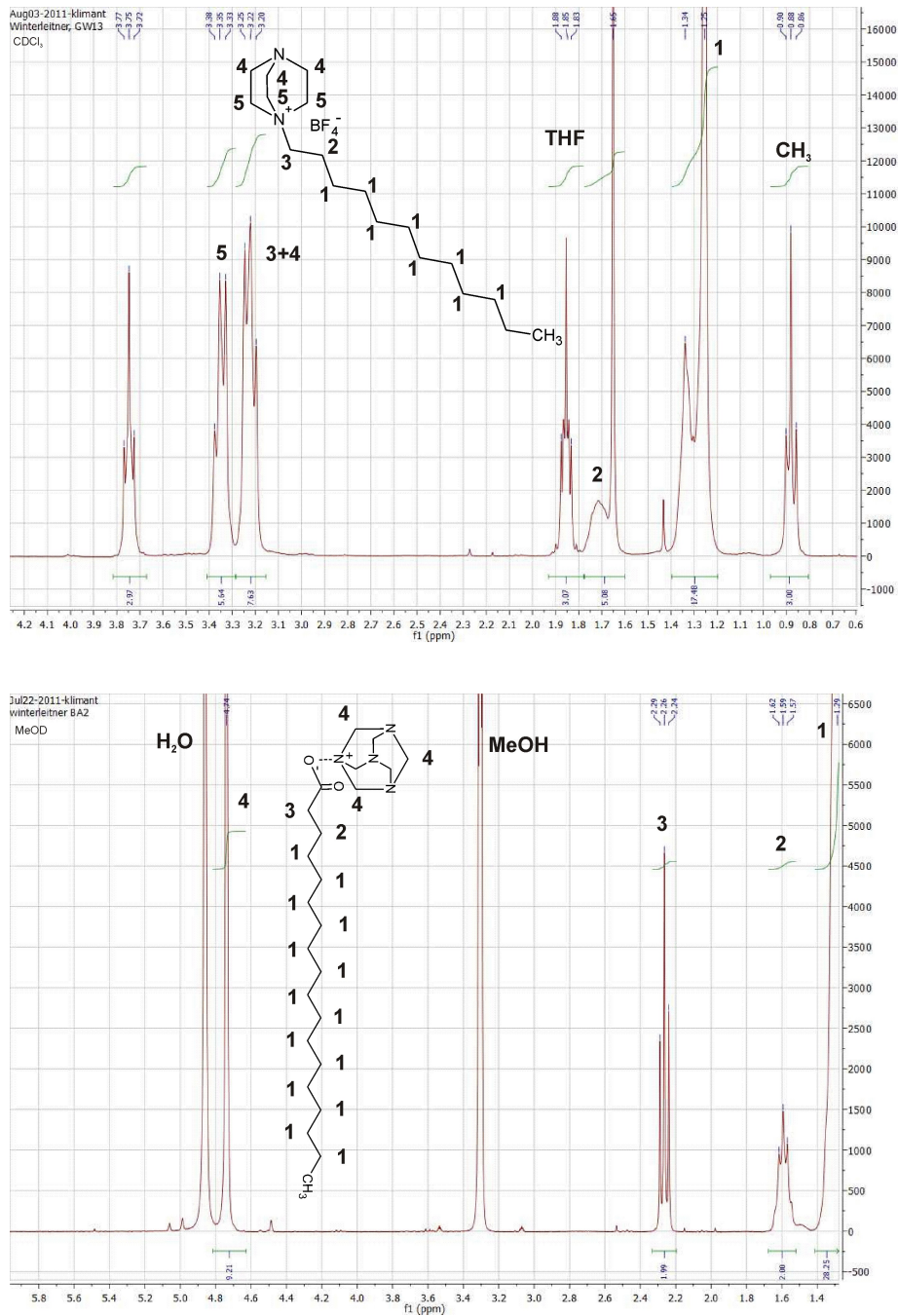
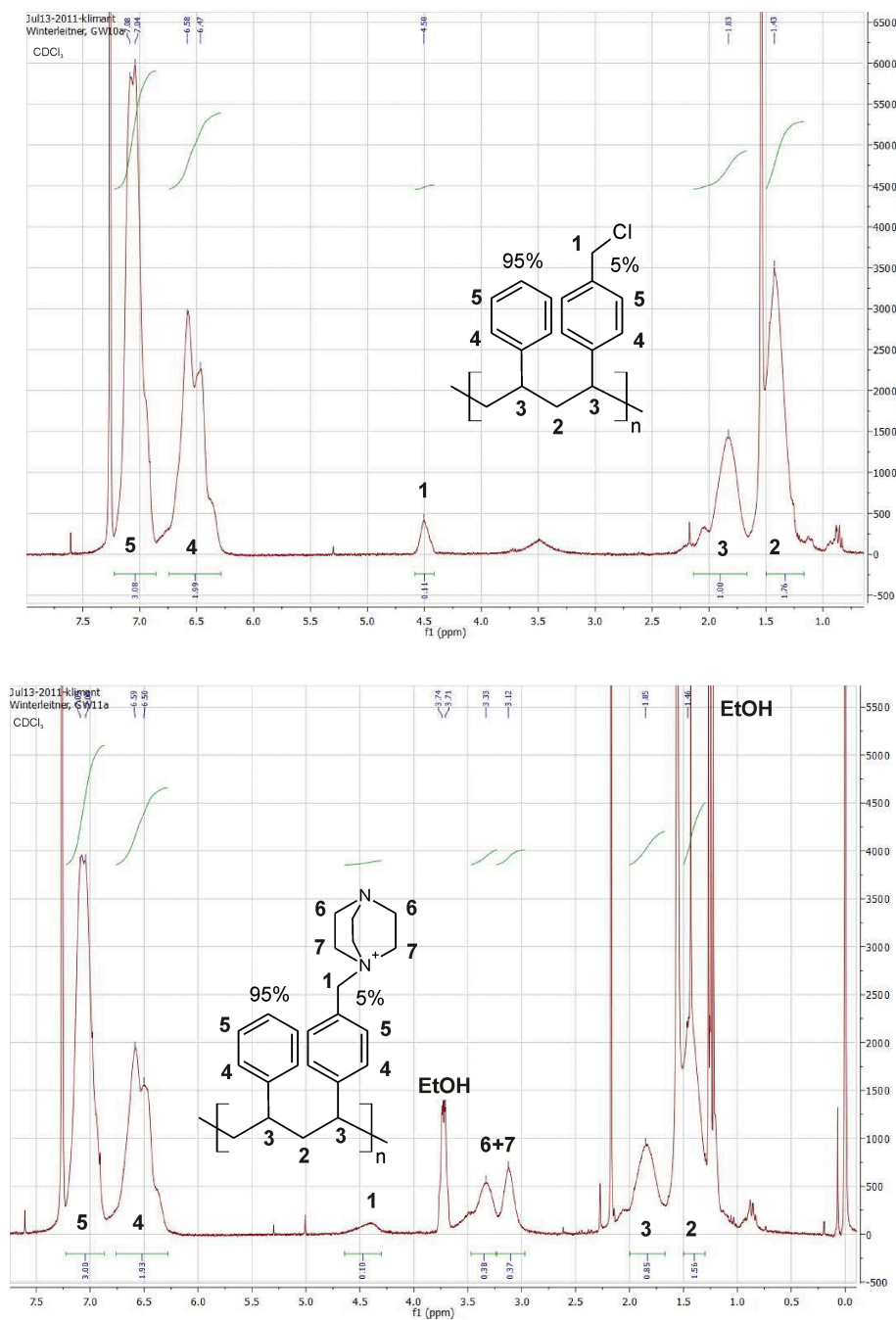


Figure 3.25: NMR spectra of Q2 and Q4.

Figure 3.26: NMR spectra of **S1** and **S2**.

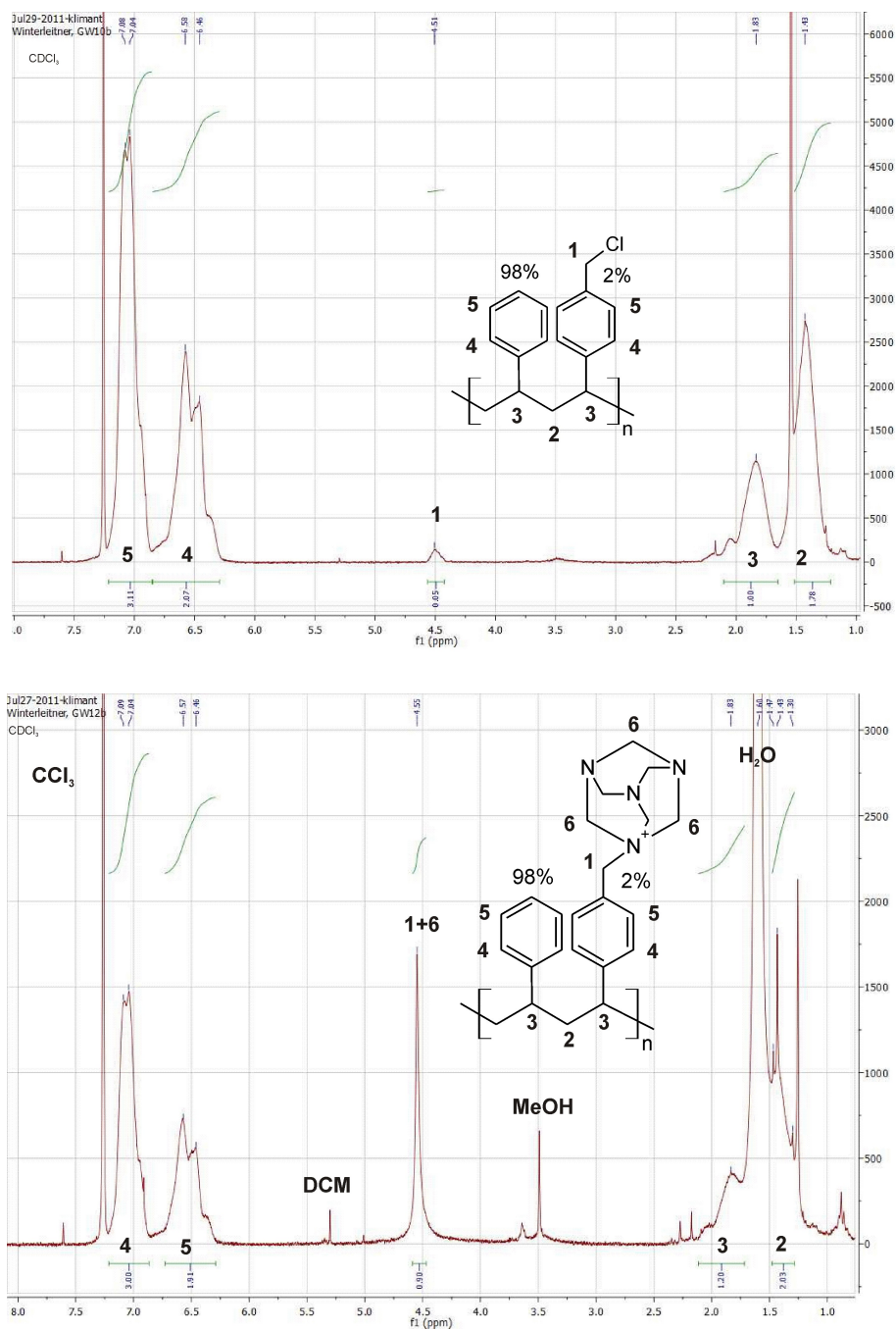


Figure 3.27: NMR spectra of S3 and S4.

“It’s an Earth food. They are called Swedish meatballs. It’s a strange thing, but every sentient race has its own version of these Swedish meatballs! I suspect it’s one of those great universal mysteries which will either never be explained, or which would drive you mad if you ever learned the truth.”

G’KAR
Babylon 5

Chapter 4

EPR Investigations of Organic Super-Acceptors

4.1 Introduction¹

The development of optoelectronic devices such as organic light-emitting diodes (OLEDs) and solar cells entails design and synthesis of functional compounds such as strong organic acceptors (super-acceptors), which are potentially applied as p-type dopants. Cyano-based derivatives represent the most prominent class of super-acceptors¹⁴⁰. Tetracyanoethene (TCNE)¹⁴¹ and 7,7,8,8-tetracyanoquinodimethane (TCNQ)¹⁴² together with their derivatives were shown to form charge-transfer complexes (CTCs) and salts with various organic and organo-metallic electron donors that often exhibit technologically interesting materials properties such as electric conductivity and magnetic phenomena. Employing such environmentally stable acceptors as p-type dopants in OLEDs and solar cells significantly improves the performance of these devices¹⁴³.

The cyano-based species investigated in this work are depicted in figure 4.1 consist of two moieties: (1) An electron-acceptor group featuring a conjugated pi-system substituted with a sufficient number of cyano-groups and (2) A N,N-dimethylanilino-group (DMA-group) serving as electron donor. While the donor moiety is the same in all investigated compounds, the acceptor group is chemically varied in terms of acceptor strength (introducing fluoro-groups), number of electron-withdrawing cyano functionalities and introduction of 2,5-diene-1,4-diylidene spacers. Accordingly, the electron-acceptor groups are derivatives of TCNE, TCNQ and F₄-TCNQ (2,3,5,6-tetrafluoro-7,7,8,8-tetracyanoquinodimethane), respectively. Despite the substitution with DMA donors, these compounds are potent electron acceptors that compete with TCNE and TCNQ in their ease of reversible electron uptake.

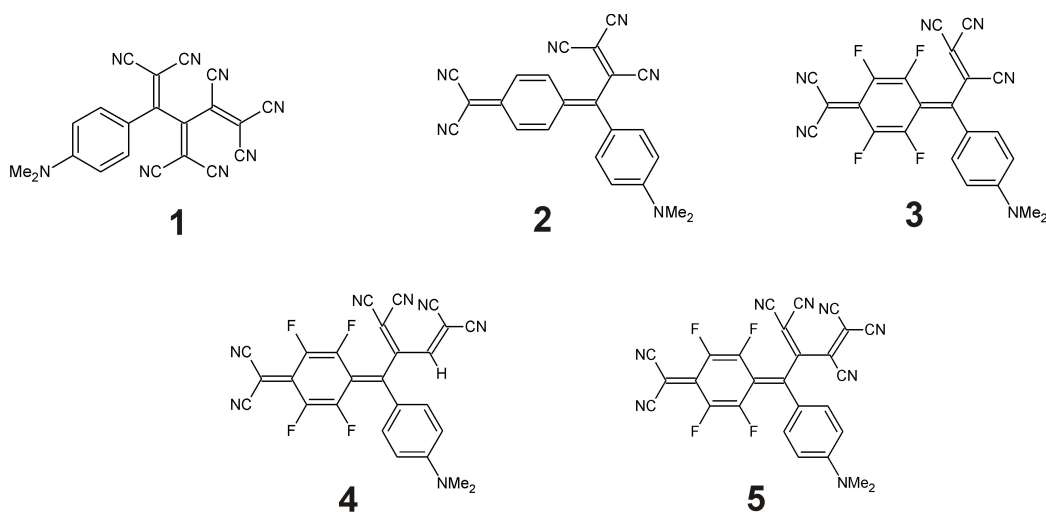


Figure 4.1: Investigated super-acceptors **1** to **5**.

The investigations presented in this work have been published by Kivala et al.¹, therefore this chapter is based on this paper.

4.2 Experimental

4.2.1 Sample Preparation

Solid State. 2-5 mg of the sample were filled into an EPR glass sample tube and mounted in the instrument for measurements.

Solutions in [D₆]acetone. The sample was dissolved in [D₆]acetone to give a 1 mM solution. The solution was deoxygenated thoroughly by argon bubbling through for 10 minutes.

Reduction. 1,2-Dimethoxyethane (DME) was heated to reflux over Na/K alloy, condensed under high vacuum and stored over Na/K alloy under high vacuum. The samples were prepared in custom made sample tubes under high vacuum. After dissolving the probe in DME, reduction was performed by contact of the DME solution of the parent compound with a K-metal mirror (sublimed in the sample tube) under high vacuum.

4.2.2 Measurements

All EPR spectra were recorded on a Bruker ESP 300 X-band spectrometer. All measurements were performed at ambient temperature (ca. 298 K), unless otherwise stated.

4.3 Results

Compounds **1**, **4** and **5** were measured in their solid state and dissolved in [D₆]acetone. Obtained EPR spectra are given in figures 4.2 to 4.4. Compounds **2** and **3** were dissolved in DME and reduced by contact of the DME solution with a K-metal mirror under high vacuum. Obtained EPR spectra are depicted in figures 4.5 to 4.7. The *g*-factors for all measured compounds are given in table 4.1.

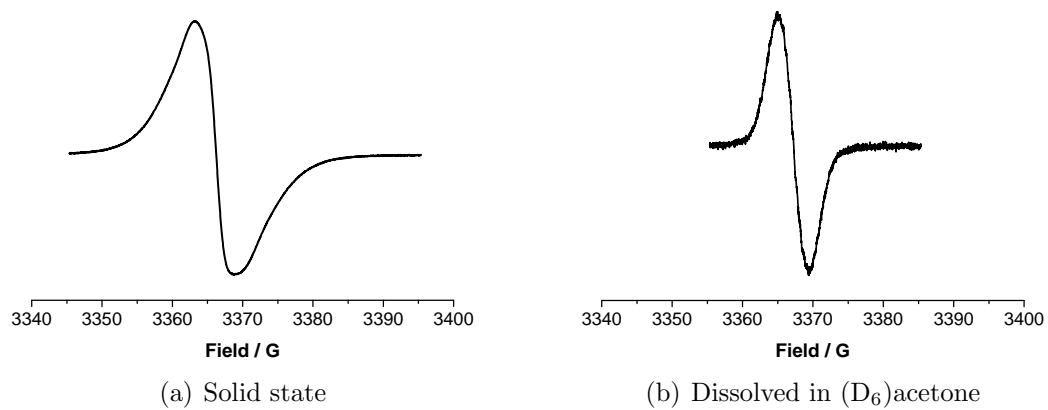


Figure 4.2: EPR spectra of compound 1.

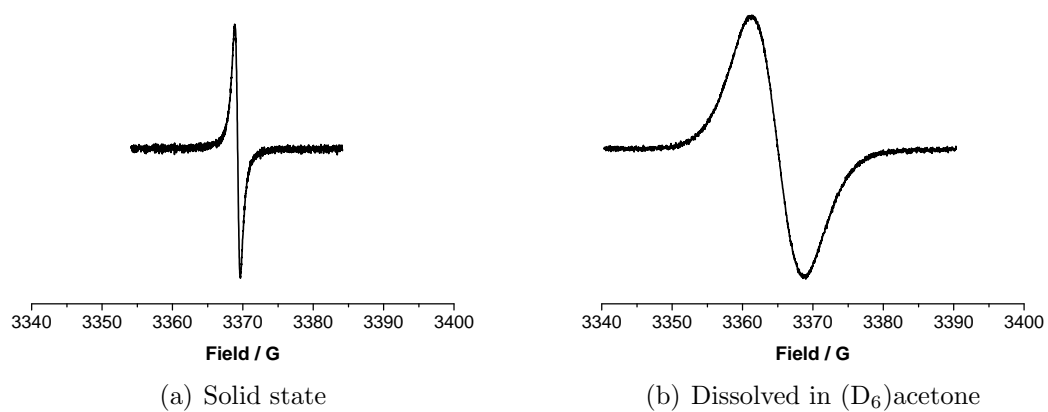


Figure 4.3: EPR spectra of compound 4.

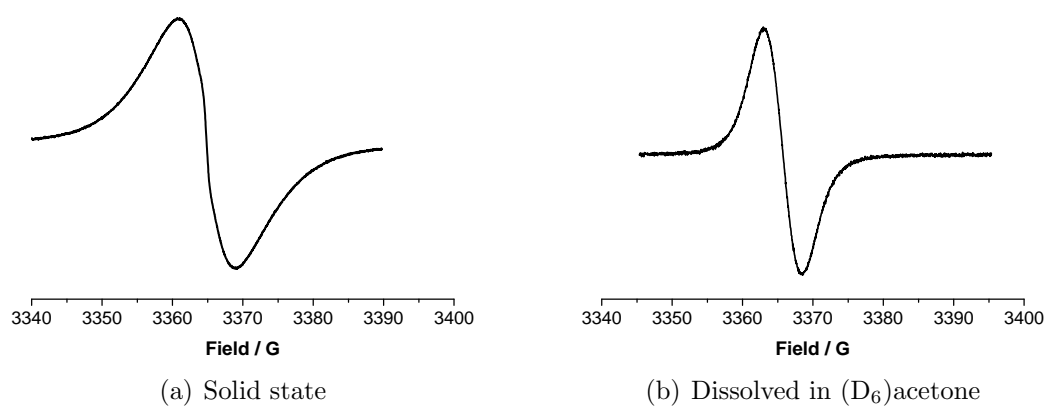


Figure 4.4: EPR spectra of compound 5.

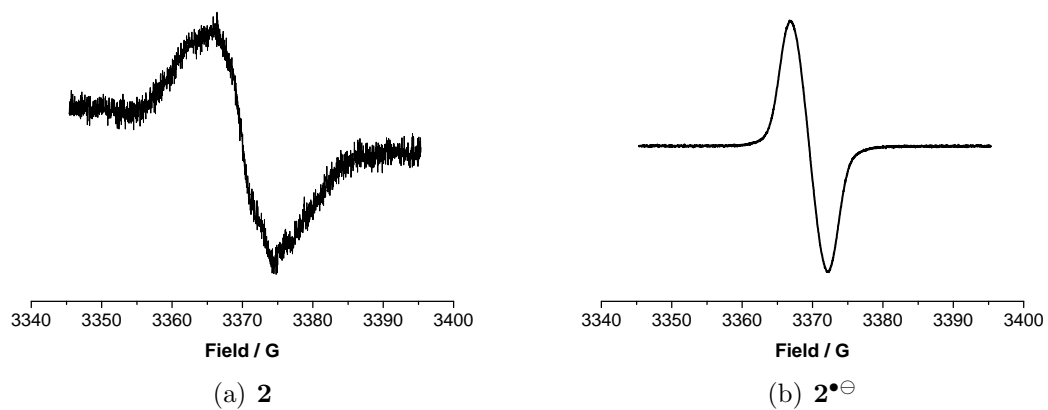
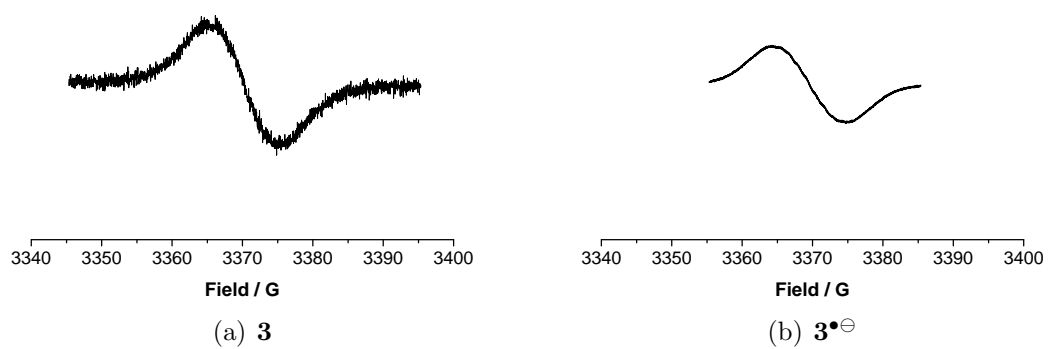
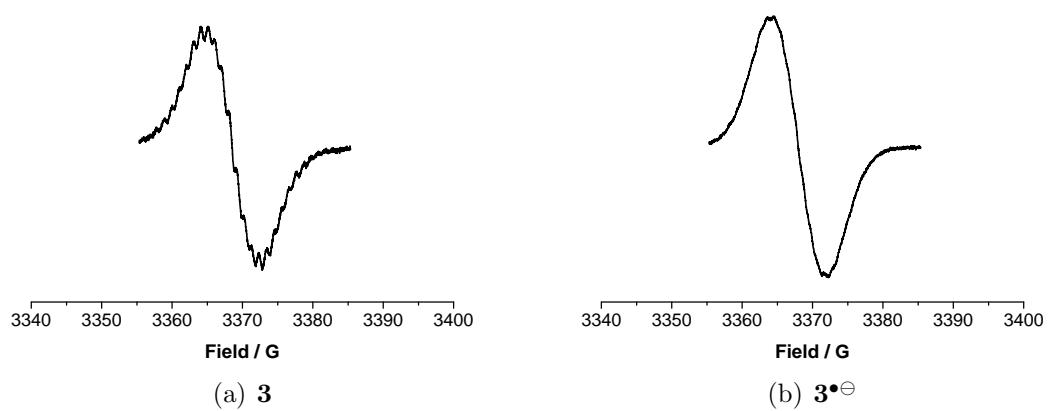
Figure 4.5: EPR spectra of compounds **2** and $2^{\bullet\ominus}$ in DME at 180 KFigure 4.6: EPR spectra of compounds **3** and $3^{\bullet\ominus}$ in DME at 180 K.Figure 4.7: EPR spectra of compounds **3** and $3^{\bullet\ominus}$ in DME at 270 K.

Table 4.1: g factors of investigated compounds.

	g factor
1 solid state	2.0036
1 [D ₆]acetone solution	2.0034
2 in DME at 180 K	2.0034
2 ^{•⊖} in DME at 180 K	2.0036
3 in DME at 180 K	2.0033
3 ^{•⊖} in DME at 180 K	2.0037
3 in DME at 270 K	2.0034
3 ^{•⊖} in DME at 270 K	2.0036
4 solid state	2.0037
4 [D ₆]acetone solution	2.0032
5 solid state	2.0033
5 [D ₆]acetone solution	2.0032
TCNE ^{•⊖} 144	2.0026 ± 0.0002
TCNQ ^{•⊖} 145	2.0027 ± 0.0002
F ₄ -TCNQ ^{•⊖} 145	2.0029 ± 0.0001

4.4 Conclusion

EPR measurements of the investigated compounds revealed the paramagnetic character of all samples. EPR spectra of remarkable intensity were obtained for solid samples of **1**, **4** and **5** at ambient temperature. Dissolving **1**, **4** and **5** in [D₆]acetone and **2** and **3** in DME again led to intense EPR spectra both in liquid and frozen solution. The obtained spectra are unresolved in all cases, whereas broader lines are observed due to anisotropic interactions in the solid state. Nevertheless, the virutally matching *g* factors indicate that the EPR singals observed for all compounds in the solid-state and solution result from compatible electronic structures.

Furthermore, reduction of **2** and **3** with K metal in DME at 270 K yielded in intense EPR spectra that are compatible in terms of its shape and *g* factor to that of the unreduced compounds in DME solution. The data is in good agreement with the published values for radical anions of TCNE, TCNQ and F₄-TCNQ. Owing to the very low first reduction potentials of the investigated compounds, it can be anticipated that the corresponding radical anions are at least partly present under the applied experimental conditions.

All compounds were furthermore analyzed by the means of NMR. The fact that no NMR spectra are observable is again in line with the paramagnetism revealed by EPR experiments.

Organic Super-Acceptors with Efficient Intramolecular Charge-Transfer Interactions by [2+2] Cycloadditions of TCNE, TCNQ, and F₄-TCNQ to Donor-Substituted Cyanoalkynes**

Milan Kivala,^[a] Corinne Boudon,^[b] Jean-Paul Gisselbrecht,^[b] Barbara Enko,^[c]
Paul Seiler,^[a] Imke B. Müller,^[d] Nicole Langer,^[d] Peter D. Jarowski,^[a]
Georg Gescheidt,^[c] and François Diederich*^[a]

Dedicated to Professor Seiji Shinkai on the occasion of his 65th birthday

Abstract: Thermal [2+2] cycloadditions of tetracyanoethene (TCNE), 7,7,8,8-tetracyanoquinodimethane (TCNQ), and 2,3,5,6-tetrafluoro-7,7,8,8-tetracyanoquinodimethane (F₄-TCNQ) to *N,N*-dimethylanilino-substituted (DMA-substituted) alkynes bearing either nitrile, dicyanovinyl (DCV; -CH=C(CN)₂), or tricyanovinyl (TCV; -C(CN)=C(CN)₂) functionalities, followed by retro-electrocyclization, afforded a new class of stable organic super-acceptors. Despite the non-planarity of these acceptors, as revealed by X-ray crystallographic analysis and theoretical calculations, efficient intramolecular charge-transfer (CT) interactions between the DMA donors and the CN-containing acceptor moieties are established. The corresponding CT bands appear strongly bathochromically shifted with maxima up to 1120 nm (1.11 eV) accompanied by an end-absorption in the near infrared around 1600 nm (0.78 eV) for F₄-TCNQ adducts. Electronic absorp-

tion spectra of selected acceptors were nicely reproduced by applying the spectroscopy oriented configuration interaction (SORCI) procedure. The electrochemical investigations of these acceptors by cyclic voltammetry (CV) and rotating disc voltammetry (RDV) in CH₂Cl₂ identified their remarkable propensity for reversible electron uptake rivaling the benchmark compounds TCNQ ($E_{\text{red},1} = -0.25$ V in CH₂Cl₂ vs. Fc⁺/Fc) and F₄-TCNQ ($E_{\text{red},1} = +0.16$ V in CH₂Cl₂ vs. Fc⁺/Fc). Furthermore, the electron-accepting power of these new compounds expressed as adiabatic electron affinity (EA) has been estimated by theoretical calculations and compared to the reference acceptor F₄-TCNQ, which is used as a p-type dopant in the fabrication of

organic light-emitting diodes (OLEDs) and solar cells. A good linear correlation exists between the calculated EAs and the first reduction potentials $E_{\text{red},1}$. Despite the substitution with strong DMA donors, the predicted EAs reach the value calculated for F₄-TCNQ (4.96 eV) in many cases, which makes the new acceptors interesting for potential applications as dopants in organic optoelectronic devices. The first example of a charge-transfer salt between the DMA-substituted TCNQ adduct ($E_{\text{red},1} = -0.27$ V vs. Fc⁺/Fc) and the strong electron donor decamethylferrocene ([FcCp*]₂); Cp* = pentamethylcyclopentadienide; $E_{\text{ox},1} = -0.59$ V vs. Fc⁺/Fc) is described. Interestingly, the X-ray crystal structure showed that in the solid state the TCNQ moiety in the acceptor underwent reductive σ -dimerization upon reaction with the donor.

Keywords: charge transfer • cycloaddition • electrochemistry • electron acceptors • electron affinity • EPR spectroscopy

[a] Dr. M. Kivala, P. Seiler, Dr. P. D. Jarowski, Prof. Dr. F. Diederich
Laboratorium für Organische Chemie
ETH Zürich
Hönggerberg, HCI, 8093 Zürich (Switzerland)
Fax: (+41)44 632 1109
E-mail: diederich@org.chem.ethz.ch

[b] Prof. Dr. C. Boudon, Dr. J.-P. Gisselbrecht
Laboratoire d'Electrochimie et de Chimie Physique du Corps Solide
Institut de Chimie—UMR 7177, CNRS, Université Louis Pasteur
4, rue Blaise Pascal, 67000, Strasbourg (France)

[c] B. Enko, Prof. Dr. G. Gescheidt
Institut für Physikalische und Theoretische Chemie, TU Graz
Technikerstrasse 4/I, 8010 Graz (Austria)

[d] Dr. I. B. Müller, Dr. N. Langer
BASF SE, GVP/C—A030, 67056 Ludwigshafen (Germany)

[**] TCNE = tetracyanoethene, TCNQ = 7,7,8,8-tetracyanoquinodimethane, F₄-TCNQ = 2,3,5,6-tetrafluoro-7,7,8,8-tetracyanoquinodimethane.

Supporting information for this article is available on the WWW under <http://dx.doi.org/10.1002/chem.200802563>.

Introduction

Among the large number of strong organic acceptors that have been described to date, cyano-based derivatives represent the most prominent class of compounds for optoelectronic device applications.^[1] Tetracyanoethene (TCNE)^[2,3] and 7,7,8,8-tetracyanoquinodimethane (TCNQ)^[4,5] together with their derivatives^[6] were shown to form charge-transfer (CT) complexes and salts with various organic and organometallic electron donors that often exhibit technologically interesting materials properties such as electric conductivity^[7,8] and magnetic phenomena.^[9] Furthermore, environmentally stable acceptors are increasingly applied as p-type dopants, significantly improving the performance of optoelectronic devices such as organic light-emitting diodes (OLEDs) and solar cells.^[10] Although 2,3,5,6-tetrafluoro-7,7,8,8-tetracyanoquinodimethane (F₄-TCNQ)^[6a] is widely used for this purpose, alternative dopants, such as the recently reported 3,6-difluoro-2,5,7,7,8,8-hexacyanoquinodimethane (F₂-HCNQ) with superior thermal stability,^[11] are currently being pursued by many researchers.

Recently, we have shown that formal [2+2] cycloadditions, followed by retro-electrocyclization of the initially formed cyclobutenes, of TCNE^[12,13] and TCNQ^[14,15] to “electronically confused” alkynes bearing one electron-donating group and one electron-withdrawing group, such as *N,N*-dimethylanilino-substituted (DMA-substituted) cyanoalkynes, yield donor-substituted 1,1,2,4,4-pentacyanobuta-1,3-dienes^[16] (PCBDs) and the corresponding cyclohexa-2,5-diene-1,4-diyliene-expanded derivative, respectively.^[17] Despite the substitution with DMA donors, these compounds are potent electron acceptors that compete with TCNE and TCNQ in their ease of reversible electron uptake. Furthermore, intense bathochromically shifted intramolecular CT bands are observed in their UV/Vis spectra. Based on these results, we expected that even stronger electron acceptors would be in reach upon i) incorporation of particularly strong acceptor moieties, such as F₄-TCNQ, and ii) increasing the number of electron-withdrawing cyano functionalities in the molecule.

Here, we introduce a new family of strong electron acceptors **1–7** obtained by reactions of TCNE, TCNQ, and F₄-TCNQ with DMA-substituted alkynes bearing either nitrile (**8**),^[17,18] dicyanovinyl (DCV; -CH=C(CN)₂) (**9**),^[13b] or tricyanovinyl (TCV; -C(CN)=C(CN)₂) (**10**) functionalities (Table 1).^[19] Initial attempts to prepare intermolecular CT complexes with strong electron donors, such as decamethylferrocene ([FeCp*₂]; Cp* = pentamethylcyclopentadienide)^[20] will be discussed as well.

Results and Discussion

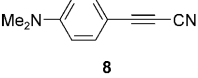
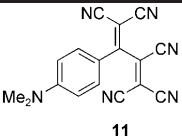
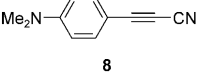
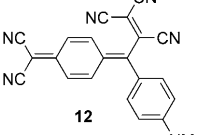
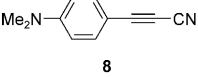
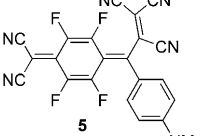
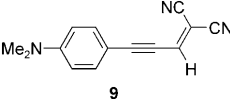
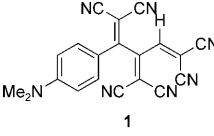
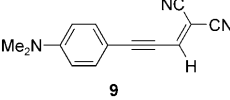
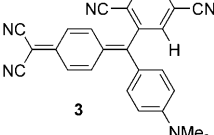
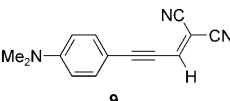
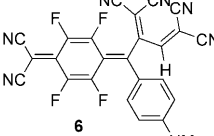
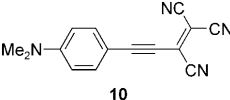
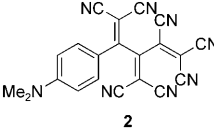
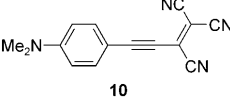
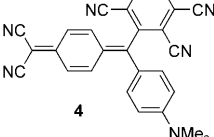
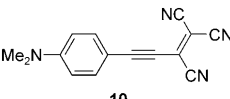
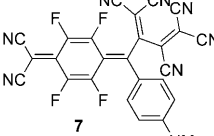
Synthesis and characterization: Whereas the previously reported reaction of TCNE with cyanoalkyne **8** to give DMA-substituted PCBD **11** proceeded in nearly quantitative yield in tetrahydrofuran (THF) at 20 °C,^[17] similar reaction with

DCV-substituted alkyne **9** and TCV-derivative **10** to yield the corresponding adducts **1** (26%) and **2** (66%), respectively, required heating in 1,2-dichloroethane or 1,1,4,4-tetrachloroethane up to 120 °C (Table 1). As already observed for **12**,^[17] TCNQ displays rather reduced reactivity, compared to TCNE, towards formal cycloadditions with alkynes. While an excess of TCNQ, prolonged reaction times, and elevated temperature (60 °C) were applied in the synthesis of **3**, complete consumption of the starting alkyne **9** could not be reached. Subsequent repeated chromatographic purifications on SiO₂ afforded **3** in a rather low yield of 14% due to partial decomposition during column chromatography (CC). Furthermore, reaction of TCNQ with TCV-substituted alkyne **10** under various conditions delivered only a trace amount of the corresponding heptacyano derivative **4**, accompanied by a mixture of unidentifiable products, as revealed by mass spectrometry. Gratifyingly, the stronger acceptor F₄-TCNQ showed significantly higher reactivity, compared to TCNQ, towards regioselective cycloadditions with alkynes. Thus, fluorinated adducts **5–7** were obtained in good yields ranging from 65 (**5**) to 88% (**7**), respectively, upon reaction with DMA-substituted cyanoalkynes **8–10** in CH₂Cl₂ at 25 °C (Table 1).

All newly prepared acceptors **1–3** and **5–7** are dark metallic-like solids that are stable at ambient temperature under air and reasonably soluble in common organic solvents such as CH₂Cl₂, acetone, and acetonitrile (except for nearly insoluble **6**). However, solutions of F₄-TCNQ adducts **5–7** were found to deteriorate gradually upon contact with glass surfaces to form green insoluble products. Thus, glassware previously deactivated by silylation with dimethyldichlorosilane (DMDCS) should be used for all manipulations involving **5–7**.^[21] Complete decomposition was observed during attempted chromatography (SiO₂ and C₁₈-reversed phase SiO₂) of **2** and **5–7**. Consequently, **2** and **5–7** were successfully purified by repeated crystallization by slow diffusion of *n*-hexane into CH₂Cl₂ solution of the compound at 25 °C. The identity of **1–7** was confirmed by high-resolution MALDI FT-ICR (for **1** and **2**) or MALDI-TOF mass spectrometry (for **3–7**), which displayed the corresponding molecular ion (see the Supporting Information), and/or NMR spectroscopy, X-ray crystallography (for **1**), and elemental analysis. For acceptors **2**, **6**, and **7**, the NMR spectra could not be recorded due to the presence of paramagnetic species in the sample, as confirmed by electron paramagnetic resonance (EPR) spectroscopy (vide infra), and low solubility of the solid (¹H and ¹⁹F NMR spectra for **5** were obtained in one case, however, they could not be reproduced). Similar behavior has previously been described for other TCNQ-derived strong acceptors.^[6a,11]

Single crystals of **1** suitable for X-ray crystallographic analysis were obtained by slow diffusion of *n*-hexane into CH₂Cl₂ solution at 25 °C (Figure 1a). As already observed,^[13c] in the crystal packing of highly distorted **1**, two neighboring molecules undergo several dipolar CN⋯CN interactions (Figure 1b). The CN groups of one molecule interact with the C(CN)₂ moiety of its neighbor with the shortest

Table 1. Summary of the reactions of cyano-substituted alkynes **8–10** with TCNE, TCNQ, and F₄-TCNQ.

Cyanoalkyne	Acceptor	Product	Reaction conditions	Time	Yield [%]
	TCNE		[a]	4 days	97 ^[b]
	TCNQ		[c]	12 h	27 ^[b]
	F ₄ -TCNQ		[d]	17 h	65
	TCNE		[c]	16 h	26
	TCNQ		[c]	5 days	14
	F ₄ -TCNQ		[d]	16 h	84
	TCNE		[c]	2 days	66
	TCNQ		[f]	[f]	n.d.
	F ₄ -TCNQ		[d]	5 days	88

[a] In THF, 20 °C. [b] See reference [17]. [c] In 1,1,2,2-tetrachloroethane, 120 °C. [d] In CH₂Cl₂, 25 °C. [e] In 1,2-dichloroethane, 60 °C. [f] Under various reaction conditions, only traces of **4** were formed (MALDI-TOF MS).

contact of 3.02 Å observed between N16' and the central vinylic carbon atom C4. Consequently, two nearly orthogonal intermolecular CN...CN contacts between N16' and C7 or

atoms in **6**, an additional red shift of both CT bands to $\lambda_{\max} = 697$ nm (1.78 eV; $\epsilon = 40600$ M⁻¹ cm⁻¹) and $\lambda_{\max} = 942$ nm (1.32 eV; $\epsilon = 17000$ M⁻¹ cm⁻¹) occurs (Figure 2). Increasing

C5 of 3.17 and 3.12 Å, respectively, are formed. Similarly to DMA-substituted 1,1,4,4-tetracyanobuta-1,3-dienes (TCBDs)^[13b,c] and TCNQ adducts,^[15a] the DMA ring in **1** exhibits significant bond alternation, as expressed by its quinoid character (δr ; for its definition^[22] and bond lengths, see caption to Figure 1) of 0.052, indicative of efficient intramolecular CT interactions in the ground state.

The thermal stability of selected acceptors, that is essential for potential practical applications, was investigated by thermogravimetric analysis (TGA). The first observable decomposition temperatures, as determined by derivative thermogravimetry, ranged from 176 (for **7**) to 482 °C (for **2**) and presumably correspond to the loss of co-crystallized solvents. These decompositions are followed by a gradual weight loss in most cases (see the Supporting Information).

UV/Vis spectroscopy: Most of the DMA-substituted acceptors show in CH₂Cl₂ intense CT bands with end-absorptions reaching into the near infrared region (Figure 2). The UV/Vis absorption spectrum of hexacyano derivative **1** features the lowest-energy intramolecular CT band at 486 nm (2.55 eV; $\epsilon = 43300$ M⁻¹ cm⁻¹). Introduction of the cyclohexa-2,5-diene-1,4-diylidene spacer in **3** shifts the CT band to 633 nm (1.96 eV; $\epsilon = 13900$ M⁻¹ cm⁻¹), with a second, weaker CT band of lower energy appearing at $\lambda_{\max} = 930$ nm (1.33 eV; $\epsilon = 1400$ M⁻¹ cm⁻¹). Upon substitution of the TCNQ-derived moiety with the strongly electron-withdrawing fluorine

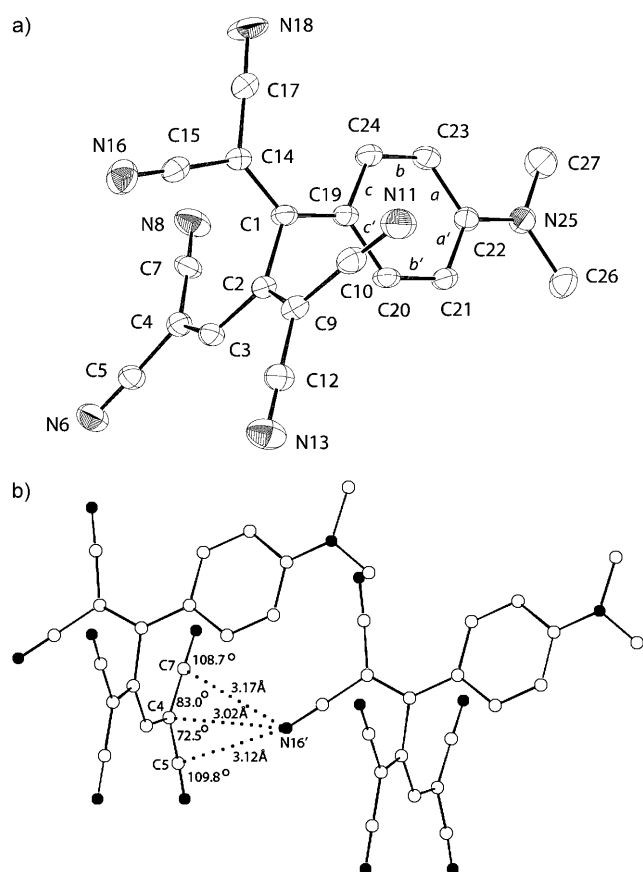


Figure 1. a) Molecular structure of **1** (ORTEP plot), arbitrary numbering, hydrogen atoms are omitted for clarity. Atomic displacement parameters obtained at 220 K are drawn at the 30% probability level. Selected bond lengths [Å] and bond angles [°]: C1–C2 1.516(5), C2–C3 1.448(5), C3–C4 1.366(5), C4–C5 1.433(5), C4–C7 1.412(6), C5–N6 1.140(5), C7–N8 1.146(5), C1–C14 1.376(5), C14–C17 1.442(5), C14–C15 1.427(6), C15–N16 1.153(5), C17–N18 1.134(5), C2–C9 1.358(5), C9–C12 1.429(6), C12–N13 1.139(5), C1–C19 1.417(5), C9–C10 1.442(6), C10–N11 1.141(5), C19–C20 1.415(5), C20–C21 1.363(5), C21–C22 1.405(5), C22–C23 1.413(5), C23–C24 1.362(5), C19–C24 1.423(5), C22–N25 1.354(5), N25–C27 1.460(5), N25–C26 1.470(5); C14–C1–C2 113.3(3), C15–C14–C17 112.9(3), C7–C4–C5 116.1(3), C12–C9–C10 115.7(3). Selected torsion angles [°]: C14–C1–C19–C24 $-2.9(6)$, C14–C1–C2–C9 $-93.2(4)$, C26–N25–C22–C21 $-0.3(6)$. Quinoid character: $\delta r = (((a+a')/2 - (b+b')/2) + ((c+c')/2 - (b+b')/2))/2$.^[22] $\delta r = 0.052$. b) Arrangement of neighboring molecules in the crystal packing of **1**.

the number of the accepting CN groups, for example when going from fluorinated **5** to **7**, further lowers the energy of the CT bands. Indeed, absorption maxima at 753 nm (1.65 eV) and 1120 nm (1.11 eV), with an end-absorption near 1600 nm (0.78 eV), are observed for **7**. This low optical gap is quite remarkable for a small chromophore such as **7**.^[23] Protonation of the DMA moiety in **7** with trifluoroacetic acid (TFA) in CH_2Cl_2 eliminated these long-wavelength bands, whereas neutralization with K_2CO_3 regenerated partially (due to decomposition) the original spectrum, thus indicating the CT character of these bands (see the Supporting Information).

Electronic absorption spectra of **1–3**, **5**, **11**, and **12** were calculated by applying the spectroscopy oriented configura-

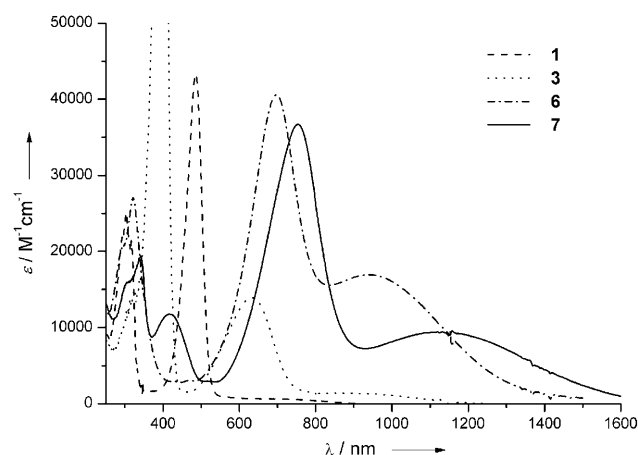


Figure 2. UV/Vis absorption spectra of acceptors **1**, **3**, **6**, and **7** in CH_2Cl_2 at 298 K. The high-intensity band of **3** at $\lambda_{\text{max}} = 400$ nm ($\epsilon = 108400 \text{ M}^{-1} \text{ cm}^{-1}$) is cut to allow enlargement of the weaker CT transitions.

tion interaction (SORCI)^[24] procedure implemented in the ORCA program suite.^[25] For acceptors **1–3** and **11**, the SORCI excitation energies are in good agreement with the experimental UV/Vis spectra recorded in CH_2Cl_2 (Table 2). However, the computational analysis for **5** and **12** did not reproduce the experimental values well (see the Supporting Information). According to theoretical data for **1–3** and **11**, the lowest energy excitation with high extinction coefficient (ϵ) and calculated high oscillator strength (f) can be assigned as a transition from the DMA-located HOMO to the LUMO+1 level located predominantly on the CN-containing acceptor moieties (for calculated HOMOs and LUMOs, see the Supporting Information). The oscillator strength of the HOMO→LUMO transition is rather small which is in agreement with weak or no extinction observed experimentally. The red shift of 1.22 eV of the longest-wavelength CT band observed in the UV/Vis spectra upon introduction of the cyclohexa-2,5-diene-1,4-diylidene spacer when moving from **1** (486 nm (2.55 eV)) to **3** (930 nm (1.33 eV)) is nicely reproduced in the SORCI spectra and amounts to 1.54 eV, with the deviation from the experimental value being within the usual error range of the method.

Whereas the optimized geometries of acceptors of **1–3** and **11** show almost perpendicular CN-containing moieties with respect to the DMA ring, and the cyclohexa-2,5-diene-1,4-diylidene spacer in **3**, it is not the case for **5** and **12** (see the Supporting Information). Consequently, the LUMO and LUMO+1 are no longer localized on either the central C atom connecting the DMA ring with the CN-containing moieties (LUMO+1) or the CN-acceptor itself (LUMO), which results in a more difficult configuration interaction problem and less accurate SORCI spectra (unless this problem is explicitly taken care of in the choice of the reference space). Thus, the first excited state with high oscillator strength for **5** and **12** is assigned to a mixture of a HOMO→LUMO+1 single excitation and an excitation of both electrons of the HOMO to the LUMO. The

Table 2. Experimental electronic transitions for **1–3** and **11**, derived from the UV/Vis spectra in CH₂Cl₂, and computed SORCI excitation spectra.

	Experimental		Computed values ^[a]		Composition of band	CI coefficients ^[b]
	λ [nm (eV)]	ϵ [M ⁻¹ cm ⁻¹]	λ [nm (eV)]	f		
1	486 (2.55)	43 300	454 (2.73)	0.81	H→L+1	0.94
	317 (3.91)	21 400				
	304 (4.08)	2500	303 (4.09)	0.92	H→L+1	0.37
2	657 (1.89)	5600	676 (1.83)	0.12	H→L	0.59
	469 (2.65)	16 300	466 (2.66)	0.33	H→L+1	0.92
			364 (3.41)	0.20	H→L+1	0.89
	295 (4.21)	15 400	311 (3.99)	0.25	H→L+1	0.75
3	930 (1.33)	1400	1045 (1.19)	0.10	H→L+1	0.54
			639 (1.94)	0.80	H→L+1	0.31
	633 (1.69)	13 900	632 (1.96)	0.16	H→L	0.88
	400 (3.10)	10 8400	414 (3.00)	0.13	H→L+1	0.79
11 ^[c]	643 (1.93)	3200	545 (2.27)	0.21	H→L+1	0.81
	450 (2.76)	30 000	418 (2.96)	0.51	H→L	0.95

[a] Only excitations with oscillator strength larger than 0.10 are shown for the calculated spectra; f =oscillator strength; H=HOMO; L=LUMO; CI=configuration interaction. [b] Correspond to the final state. [c] Taken from ref. [17].

HOMO→LUMO+1 excitation of compounds **5** and **12** is calculated at higher energies.

Electrochemistry: The redox properties of acceptors **1–3**, **5–7**, and the reference compounds TCNE, TCNQ,^[26] and F₄-TCNQ were investigated by cyclic voltammetry (CV) and rotating-disc voltammetry (RDV) in CH₂Cl₂ (+0.1 M *n*Bu₄NPF₆, all potentials vs. the ferricinium/ferrocene couple (Fc⁺/Fc)) and are summarized in Table 3. The DMA donor moiety in all studied acceptors undergoes a one-electron oxidation step that is irreversible (CV), except for **1**, **6**, and previously reported **11**, and **13**. An anodic shift of 140 mV is observed for the oxidation step upon introduction of the additional CN group into the buta-1,3-diene-1,4-diyl moiety when going from DMA-substituted 1,1,4,4-tetracyanobuta-1,3-diene (TCBD) derivative **13** ($E_{\text{ox},1} = +0.86$ V),^[13c] to PCBD **11** (+1.00).^[17] In contrast, the effect of substitution with stronger DCV (–CH=C(CN)₂) (in **1**) or TCV (–C(CN)=C(CN)₂) (in **2**) acceptor moieties is much less pronounced and TCNE adducts **1** and **2** are oxidized at lower potentials of +0.97 and +0.91 V, respectively. The extra CN group in cyclohexa-2,5-diene-1,4-diyliene-expanded PCBD **12** (+0.52 V) shifted its oxidation step anodically by 100 mV, compared to TCNQ adduct **14**, which is irreversibly oxidized at +0.42 V. Again, DCV-substituted **3** undergoes its oxidation step at +0.50 V, which corresponds to a shift of only 80 mV compared to **14**. An anodic shift of 90 mV is observed for the oxidation step upon F-substitution of the TCNQ moiety in **5** (+0.61 V) and **6** (+0.59 V) compared to their TCNQ counterparts **12** and **3**, respectively. Overall, the oxidations of TCNQ adducts **3**, **12**, and **14** (or fluorinated **5–7**) are occurring at significantly lower potentials compared to the TCNE adducts **1**, **2**, and **13**, which indicates less efficient ground state CT interactions between the DMA donor moiety and the CN accepting groups in these chromophores (vide infra).

More importantly, the studied compounds undergo two (**5**) or three (**1–3**, **6**, and **7**) reversible one-electron reduction steps centered on the CN-containing moieties, eventually followed by the fourth irreversible electron transfer for fluorinated **6** and **7**. We have previously found that the additional CN group in PCBD **11** ($E_{\text{red},1} = -0.30$ V)^[17] facilitated the first reduction step by 390 mV when compared to TCBD **13**, which is reversibly reduced at –0.69 V.^[13c,27] As expected, the incorporation of stronger acceptor moieties in DCV-substituted **1** and TCV-substituted **2** further shifts the observed reduction steps towards more

positive potentials. Thus, the introduction of the additional DCV moiety upon moving from TCBD **13** to TCNE adduct **1** (–0.22 V) shifts the first reduction step anodically by 470 mV to occur at more positive potential than that of TCNE (–0.32 V) or TCNQ (–0.25 V). Although only poorly resolved CV traces were obtained for TCV-substituted TCNE adduct **2**, the first reversible electron uptake occurs at +0.12 V, which represents an unprecedented anodic shift of 810 mV with respect to parent **13**. On the other hand, only less pronounced effects are observed between TCNQ-derivative **14** (–0.50 V)^[15a] and expanded PCBD **12** reduced at –0.27 V^[17] or DCV-substituted **3** (–0.28 V).

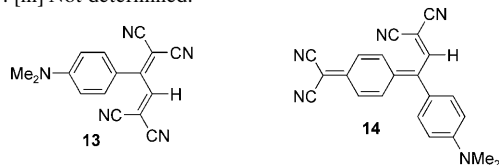
Noticeable for the new chromophores **1–3** and **5–7** is the facility of the second one-electron reduction step ($E_{\text{red},2}$ between –0.92 (for **1**) and –0.17 V (for **7**)) which is irreversible for chromophore **1**. In addition, unprecedented third reversible one-electron reduction steps are observed for **1–3**, **6**, and **7** ranging from –2.30 V (for **1**) to –1.19 V (for **7**).

As a result of F-substitution in derivatives **5–7**, the reversible reduction steps became notably facilitated with respect to their TCNQ analogues.^[28] Thus, the two reversible reduction steps of fluorinated cyclohexa-2,5-diene-1,4-diyliene-expanded PCBD derivative **5** occur anodically shifted by 270 and 260 mV at ±0.00 and –0.27 V, respectively, compared to TCNQ derivative **12** (–0.27 and –0.53 V).^[17] Furthermore, spectroelectrochemical studies of **5** performed in a optically transparent thin-layer electrode (OTTLE) suggest that the electrogenerated reduced species (i.e. radical anion and dianion) are persistent at the time scale of spectroelectrochemistry, namely at least for 60 s (see the Supporting Information). The three one-electron transfers of DCV-substituted **6** occurring at –0.10, –0.25, and –1.76 V appear shifted, compared to **3**, to more positive potentials by 180, 220, and 100 mV, respectively. The introduction of the additional CN group upon moving from **6** to **7** further

Table 3. Cyclic voltammetry (CV; scan rate $\nu=0.1 \text{ V s}^{-1}$) and rotating disk voltammetry (RDV) data of **1–3**, **5–7**, and **11–14**, and the reference compounds TCNE, TCNQ, and $\text{F}_4\text{-TCNQ}$ in CH_2Cl_2 ($+0.1 \text{ M } n\text{Bu}_4\text{NPF}_6$).^[a] Calculated adiabatic electron affinity (EA), based on the BP86/def-TZVP COSMO($\epsilon=4.5$)/BP86/def-SV(P) method.

	CV			RDV		EA [eV]
	E° [V] ^[b]	ΔE_p [mV] ^[c]	E_p [V] ^[d]	$E_{1/2}$ [V] ^[e]	Slope [mV] ^[f]	
1	+0.97	90		+0.95 (1 e ⁻)		4.49
	-0.22	80		-0.26 (1 e ⁻)	60	
2	-2.30	120		-0.99 (1 e ⁻)	90	4.87
	+0.12	60	+0.91	+0.12 (1 e ⁻)	65	
3	-1.88	60				4.51
	+0.50			+0.47 (1 e ⁻)	80	
5	-0.28	60		-0.32 (1 e ⁻)	65	4.66
	-0.47	70		-0.54 (1 e ⁻)	65	
6	-1.86	60		-1.94 (1 e ⁻)	60	4.69
	+0.61					
7 ^[g]	± 0.00	75		± 0.00 (1 e ⁻)	68	4.98
	-0.27	70		-0.29 (1 e ⁻)	61	
11 ^[i]	+0.59	80				4.36
	-0.10	60		-0.11 (1 e ⁻)	55	
12 ^[j]	-0.25	60		-0.26 (1 e ⁻)	55	4.42
	-1.76	70				
13 ^[k]			-2.26			4.98
			+0.64			
14 ^[l]	+0.16	80		+0.16 (1 e ⁻)	60	4.36
	-0.17	60		-0.19 (1 e ⁻)	60	
TCNE	-1.19	80		-1.24 (1 e ⁻)		4.57
	+1.00	90		+1.00 (1 e ⁻)	65	
TCNQ	-0.30	90		-0.30 (1 e ⁻)	65	4.59
	-0.85	100		-0.85 (1 e ⁻)	100	
$\text{F}_4\text{-TCNQ}$			+0.52	+0.54 (1 e ⁻)	50	4.96
				-0.28 (1 e ⁻)	60	
1	-0.27	80		-0.56 (1 e ⁻)	60	4.69
	-0.53	85		+0.87 (1 e ⁻)	70	
2	+0.86	80		-0.70 (1 e ⁻)	70	4.66
	-0.69	80		-1.38 (1 e ⁻)	140	
3	-1.26	90		+0.44 (1 e ⁻)	60	4.51
			+0.42	-0.55 (1 e ⁻)	70	
5	-0.50	80		-0.86 (1 e ⁻)	70	4.66
	-0.76	80				
6	-0.32					4.57
	-1.35					
7	-0.25	90		-0.26 (1 e ⁻)	75	4.59
	-0.81	90		-0.87 (1 e ⁻)	75	
11			+1.11	+0.19 (1 e ⁻)	75	4.96
				-0.48 (1 e ⁻)	85	

[a] All potentials are given versus the Fc^+/Fc couple used as internal standard. [b] $E^\circ = (E_{pc} + E_{pa})/2$, where E_{pc} and E_{pa} correspond to the cathodic and anodic peak potentials, respectively. [c] $\Delta E_p = E_{ox} - E_{red}$, where the subscripts ox and red refer to the conjugated oxidation and reduction steps, respectively. [d] E_p = Irreversible peak potential. [e] $E_{1/2}$ = Half-wave potential. [f] Slope = Slope of the linearized plot of E versus $\log[I/(I_{lim} - I)]$, where I_{lim} is the limiting current and I the current. [g] Electrode inhibition during oxidation. [h] Poorly resolved second reduction. [i] Contains a small amount of 7^- (see the Supporting Information). [j] Taken from ref. [17]. [k] Taken from ref. [13c]. [l] Taken from ref. [15a]. [m] Not determined.



shifts the first electron uptake to more positive potentials by 260 mV.^[27] While the first reduction potential for **7** is the same as that of $\text{F}_4\text{-TCNQ}$ ($+0.16 \text{ V}$), the second is, similarly to our previous observations^[17] significantly facilitated (-0.17 (**7**) vs. -0.46 V ($\text{F}_4\text{-TCNQ}$)) and is followed by two reversible one-electron transfers at -1.19 and -1.94 V . It has to be mentioned that a trace of one-electron reduced species (radical anion) has been detected by RDV in freshly prepared CH_2Cl_2 solutions of **7**, thus underscoring its exceptional electron-accepting power (see the Supporting Information).

An electron-withdrawing group involved in a donor-acceptor π -conjugated system generally hampers the oxidation, as it decreases the electron density on the oxidizable donor moieties, and conversely, an electron-donating group hinders the electron reduction by delivering electrons into the acceptor. In this respect, our findings might be rather surprising, as gradual shifts of both the oxidation and the reduction steps towards more positive potentials are expected upon increasing the electron-accepting power of the CN-containing substituents. Nevertheless, at the same time as the acceptor strength increases, as expressed by Hammett constants σ_p of $+0.66$ ($-\text{CN}$), $+0.84$ ($-\text{CH}=\text{C}(\text{CN})_2$), and $+0.98$ ($-\text{C}(\text{CN})=\text{C}(\text{CN})_2$),^[29] the substituents become sterically more demanding. This consequently, together with electrostatic repulsion between the negatively polarized N-atoms in neighboring CN groups, renders the whole molecule highly twisted (as revealed by X-ray crystallography and theoretical calculations). Under these conditions, efficient π -conjugation between the donor and acceptor moieties becomes impaired to a certain extent, as already previously observed,^[13c] which makes any straightforward correlation between the observed redox potentials and the acceptor strength rather difficult.

The optical HOMO-LUMO gaps, determined from the end-absorption λ_{end} of the longest-wavelength UV/Vis band, correlate reasonably well ($R^2 = 0.895$) with the electrochemical gaps $\Delta(E_{\text{ox},1} - E_{\text{red},1})$ suggesting that the same orbitals are involved in both optical and electrochemical gaps for **1–3**, **5–7**, and **11–14** (Table 4 and Figure 3). Furthermore, the

Table 4. Optical and electrochemical gaps of TCNE, TCNQ, and $\text{F}_4\text{-TCNQ}$ adducts **1–3**, **5–7**, and **11–14** determined from UV/Vis spectroscopy and CV in CH_2Cl_2 .

	λ_{max} [nm (eV)]	λ_{end} [nm (eV)]	$\Delta(E_{\text{ox},1} - E_{\text{red},1})$ [V]
1	486 (2.55)	920 (1.35)	1.19
2	657 (1.89)	1100 (1.13)	0.79
3	930 (1.33)	1270 (0.98)	0.78
5	993 (1.25)	1500 (0.83)	0.61
6	942 (1.32)	1400 (0.89)	0.69
7	1120 (1.11)	1640 (0.76)	0.48
11 ^[a]	643 (1.93)	820 (1.51)	1.30
12 ^[a]	859 (1.44)	1300 (0.95)	0.79
13 ^[b]	570 (2.18)	860 (1.44)	1.55
14 ^[c]	759 (1.63)	1050 (1.18)	0.99

[a] Taken from ref. [17]. [b] Taken from ref. [13c]. The originally reported λ_{end} of 960 nm (1.29 eV) was apparently overestimated. [c] Taken from ref. [15a].

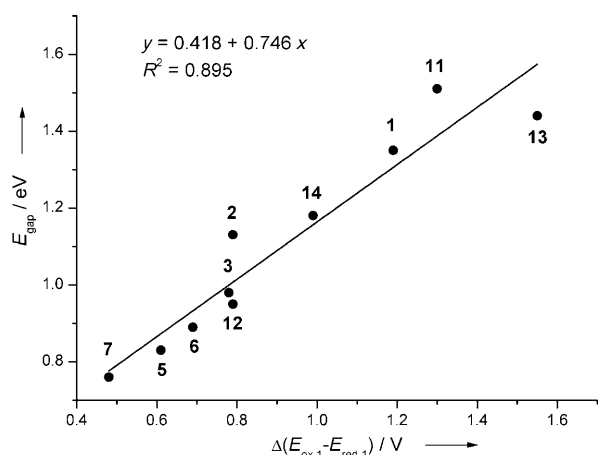


Figure 3. Linear correlation between the optical gap E_{gap} , determined from λ_{cnd} , and electrochemical gap $\Delta(E_{\text{ox},1} - E_{\text{red},1})$ for acceptors **1–3**, **5–7**, and **11–14**.

electrochemical gap decreases in the sequence **13** > **11** > **1** > **2** reflecting the increased acceptor strength of the CN-containing substituents as mentioned above.

The electron-accepting power, expressed as adiabatic electron affinity (EA), has been calculated (BP86/def-TZVP COSMO($\epsilon=4.5$)/BP86/def-SV(P))^[30] for acceptors **1–7**, **11** and **12** as well as for the reference compound F₄-TCNQ (Table 3).^[31] A good linear correlation ($R^2=0.857$) exists between the calculated EAs and the first reduction potentials $E_{\text{red},1}$ (Figure 4). Despite the substitution with strong DMA

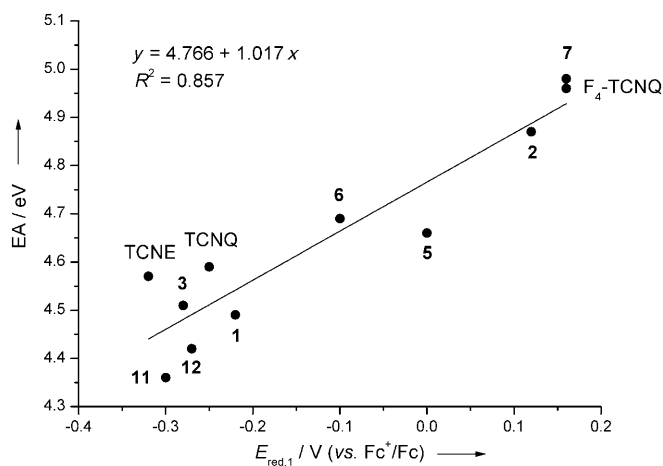


Figure 4. Linear correlation between the calculated adiabatic electron affinity EA (BP86/def-TZVP COSMO($\epsilon=4.5$)/BP86/def-SV(P)) for **1–3**, **5–7**, **11**, and **12**, F₄-TCNQ, TCNQ, and TCNE against $E_{\text{red},1}$ determined by CV.

donors, the predicted EAs for **2** (4.87 eV) and **7** (4.98 eV) rival the value calculated for the state-of-the-art p-type dopant F₄-TCNQ (4.96 eV),^[10] which makes them interesting for potential applications in optoelectronic devices.

Initial EPR investigations: Due to difficulties encountered during attempted NMR characterization (vide supra), the samples of acceptors **2** and **5–7** were investigated by means of EPR spectroscopy. Indeed, paramagnetic character of the samples both in the solid state and solution was found in all cases. EPR spectra of remarkable intensity were obtained for solid samples of **2** and **5–7** at ambient temperature. Dissolving **2**, **6**, and **7** in [D₆]acetone and **5** in 1,2-dimethoxyethane (DME) again led to intense EPR spectra both in liquid and frozen solution (for EPR spectra of **2** and **7**, see Figure 5; for **6**, see the Supporting Information). The obtained spectra are unresolved in all cases, whereas broader lines are observed due to anisotropic interactions in the solid state. Nevertheless, the virtually matching *g* factors indicate that the EPR signals observed for **2** and **5–7** in the solid-state and solution result from compatible electronic structures (Table 5).

Furthermore, reduction of **5** with K metal in DME at 270 K yielded an intense EPR spectrum that is compatible in terms of its shape and *g* factor to that of **5** recorded both in the solid state and DME solution (see the Supporting Information). The data is in good agreement with the published values for radical anions of TCNE, TCNQ, and F₄-TCNQ.^[32] Owing to the very low first reduction potentials of **2**, and **5–7**, it can be anticipated that the corresponding radical anions are at least partly present under the applied experimental conditions, as observed by others.^[6a,11]

Charge-transfer salt {[FeCp*₂]⁺]₂[12]₂²⁻ (15**):** While exploring the ability of the TCNQ-derived acceptor **12** to form charge-transfer complexes with various electron donors, we found that the TCNQ moiety in **12** undergoes reductive σ -dimerization upon reaction with the strong electron donor dcamethylferrocene ([FeCp*₂]⁺; $E_{\text{ox},1} = -0.59$ V),^[20] as previously observed for TCNQ.^[33]

Thus, an intense green solution was obtained upon addition of yellow [FeCp*₂] in CH₂Cl₂ to the originally deep-purple solution of **12** in dry acetonitrile at 25 °C. The solid obtained after evaporation of the solvents was recrystallized by slow diffusion of *n*-hexane into CH₂Cl₂ solution to afford dark-green crystals of {[FeCp*₂]⁺]₂[12]₂²⁻ (**15**) in 68% yield. The obtained crystals of **15** incorporated, even after prolonged drying in vacuo, remaining co-crystallized CH₂Cl₂ molecules, as indicated by elemental analysis and TGA that are in good agreement with the formula {[FeCp*₂]⁺]₂[12]₂²⁻·1.4 CH₂Cl₂ (see the Supporting Information).

The X-ray crystal structure of **15** consists of two independent [12]₂²⁻ ions (designated as molecule **A** and **B**), four [FeCp*₂]⁺ molecules, one of which is disordered, and three disordered CH₂Cl₂ molecules (Figure 6, for details, see the Experimental Section; for molecule **B**, see the Supporting Information).^[34] The two dimeric ions [12]₂²⁻ feature long central C–C bonds (C105–C106 and C156–C157) of 1.63 Å which are comparable to those in reported (TCNQ)₂²⁻ σ -dimers.^[33] Consequently, the involved C-atoms are practically tetrahedral with the bond angles ranging from 105.3° (C135–C105–C106) to 113.0° (C102–C105–C106). The uni-

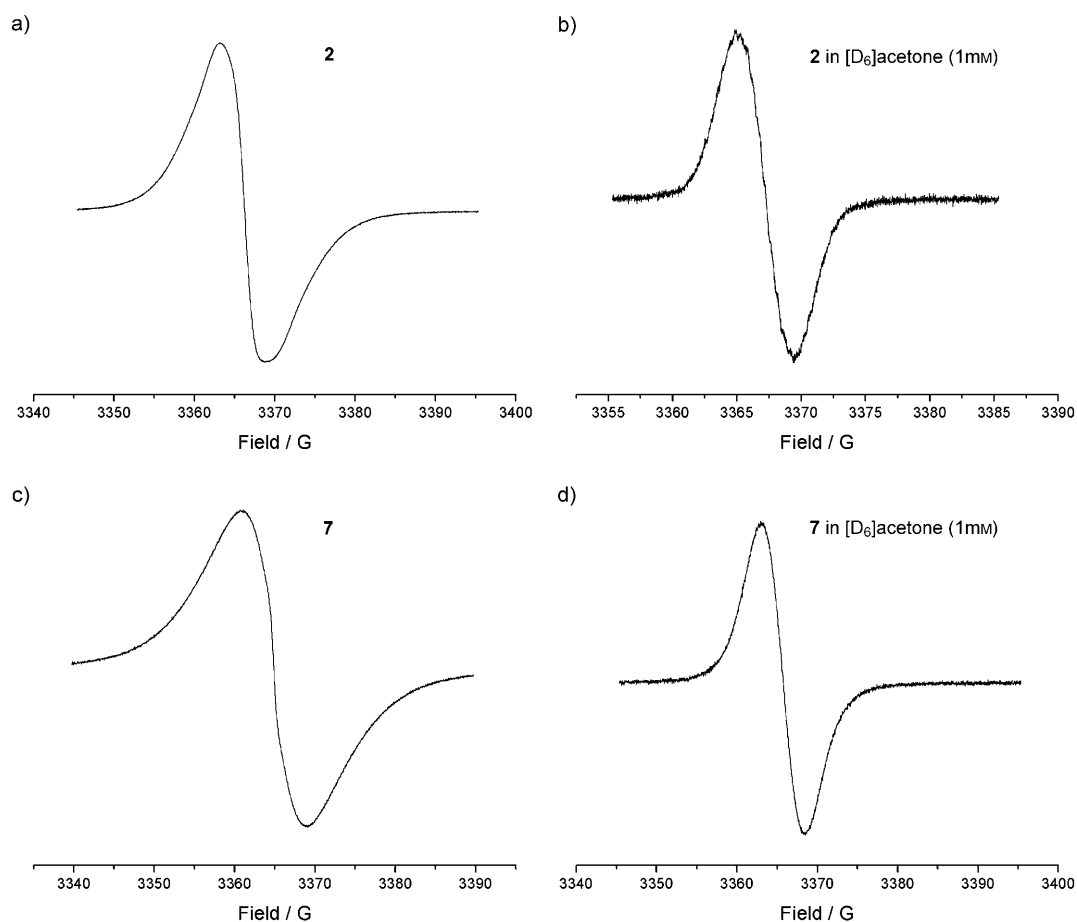


Figure 5. EPR spectra of **2** and **7** in the solid state (a and c) and in $[D_6]$ acetone solution (b and d) recorded at ambient temperature (ca. 298 K).

Table 5. The g factors extracted from the EPR spectra of **2**, **5**, and **7**, recorded under various conditions, and the g factors for the reference compounds TCNE, TCNQ, and F_4 -TCNQ.

Compound	Conditions	g factor
2	solid state	2.0036
	$[D_6]$ acetone solution (1 mm)	2.0034
5	solid state	2.0032
	DME solution (270 K)	2.0034
	after K metal reduction in DME (270 K)	2.0035
7	solid state	2.0033
	$[D_6]$ acetone solution (1 mm)	2.0032
TCNE ^{•-}	[a]	2.0026 ± 0.0002
TCNQ ^{•-}	[b]	2.0027 ± 0.0002
F_4 -TCNQ ^{•-}	[b]	2.0029 ± 0.0001

[a] Taken from ref. [32a]. [b] Taken from ref. [32b].

formity of the distances in the originally quinoid TCNQ rings in $[12]_2^{2-}$, averaging to 1.39 Å for both independent molecules, suggests that their aromatization occurred upon σ -dimer formation. Furthermore, the significant lengthening of the C=C bonds in the TCV ($-C(CN)=C(CN)_2$) moieties to an average value of 1.44 Å with the concurrent shortening of the adjacent C–C bonds to 1.37 Å indicate delocalization of the negative charge over the entire TCV unit, hence forming tricyano-substituted allylic anions (Figure 6 a). Simi-

lar effects have previously been described for other anionic TCNV-substituted systems.^[35] This is further supported by calculations at the B3LYP/6-31G(d) level^[36] performed on the $[12]_2^{2-}$ σ -dimer. The bond lengths and torsional angles of the calculated dianionic structure compare well to those obtained by X-ray analysis (see caption to Figure 6 a). The calculated HOMO of the dianionic species has most of the electron density on the TCNV moieties with only small coefficients on the central C–C bond (see the Supporting Information).

In the crystal packing of **15**, multiple short contacts with $N \cdots C$ distances ranging from 3.35 to 3.58 Å between the $[12]_2^{2-}$ ions (**A** and **B**) and the neighboring $[FeCp^*_2]^+$ molecules are observed. For example, molecule **A** is surrounded by eight $[FeCp^*_2]^+$ units with ten intermolecular $N \cdots C$ contacts between 3.36 and 3.61 Å (Figure 6 b; for molecule **B**, see the Supporting Information). The average Fe–C bond lengths of 2.097 Å, based on the three ordered $[FeCp^*_2]^+$ units, are consistent with the presence of Fe^{III} atoms.^[37]

Naturally, the σ -bond formation between two radical centers results in disappearance of paramagnetic properties. In analogy to the reported TCNQ σ -dimers, the central C–C bond in diamagnetic $[12]_2^{2-}$ is expected to be rather weak due to the long bond length, considerable delocalization of

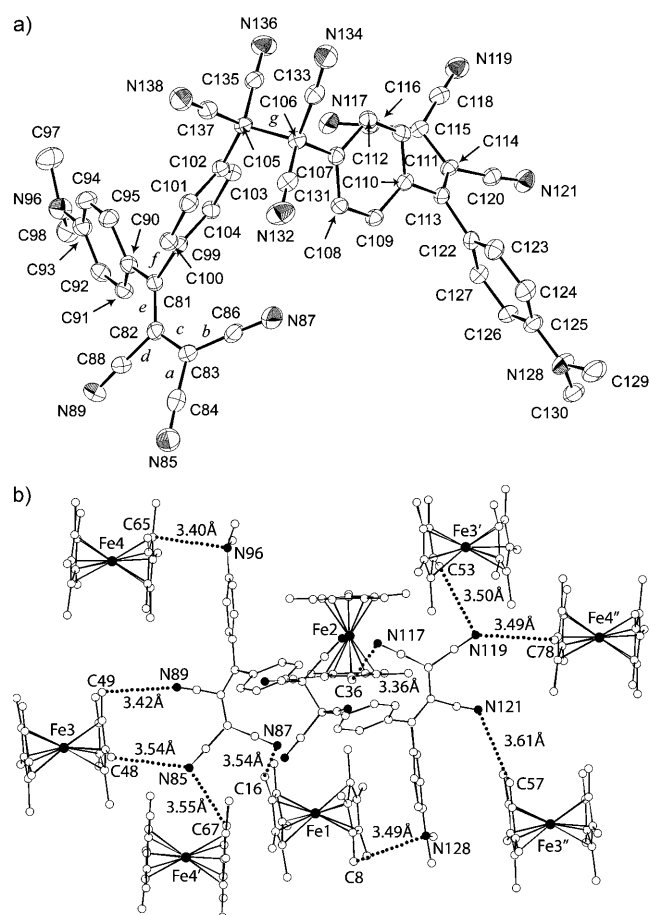
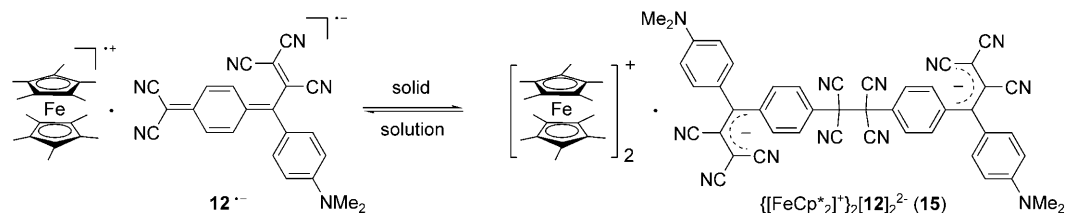


Figure 6. a) ORTEP plot of dianion $[12]_2^{2-}$ (molecule **A**) in the X-ray crystal structure of **15**. Atomic displacement parameters obtained at 220 K are drawn at the 30% probability level. Hydrogen atoms and CH_2Cl_2 molecules are omitted for clarity. Selected experimental^[34] and calculated (in parentheses; B3LYP/6-31G(d))^[36] bond lengths [Å]: *a* 1.41 (1.41), *b* 1.41 (1.42), *c* 1.44 (1.45), *d* 1.45 (1.45), *e* 1.37 (1.39), *f* 1.48 (1.48), *g* 1.63 (1.67). Selected experimental^[34] and calculated (in parentheses; B3LYP/6-31G(d))^[36] torsion angles [°]: C81-C82-C83-C84 162.7 (163.5), C99-C81-C82-C83 167.7 (161.2), C82-C81-C90-C95 140.6 (137.8), C82-C81-C99-C104 135.2 (141.0). b) Arrangement of neighboring molecules in the crystal packing of **15** showing ten intermolecular N...C contacts between $[12]_2^{2-}$ (molecule **A**) and the eight surrounding $[\text{FeCp}^*]_2^+$ molecules. The shortest contact between two neighboring molecules of type **A** (N117–C129 3.16 Å) is not shown.

the bonding electrons, and electrostatic repulsions.^[33c,38] Breaking this bond by external stimuli should yield two radical anions $12^{\cdot-}$ (Scheme 1). Indeed, the solid-state IR spectrum of **15** displays two bands in the $\nu(\text{C}\equiv\text{N})$ region at 2169



Scheme 1. Formation and dissociation of dimeric $\{[\text{FeCp}^*]_2^+\}_2[12]_2^{2-}$ (**15**).

and 2129 cm^{-1} , accompanied by a band at 806 cm^{-1} resulting from the $\delta(\text{C-H})$ bend, which are attributable to the σ -bonded TCNQ moieties.^[39] The IR spectrum recorded in CHCl_3 solution of **15** on the other hand features a single band at $\nu(\text{C}\equiv\text{N})=2178\text{ cm}^{-1}$ and a weak band at 839 cm^{-1} , which most likely results from the $\delta(\text{C-H})$ mode (see the Supporting Information), thus indicating dissociation of the central σ -bond to form two radical anions $12^{\cdot-}$ in solution. Moreover, the solid obtained upon evaporation of the CHCl_3 solution gave identical IR spectrum to that of pristine **15**. This is further supported by preliminary EPR investigations both in the solid state and solution. Whereas the solid sample of **15** containing diamagnetic σ -dimers $[12]_2^{2-}$ is EPR silent both at 290 and 180 K, dissolving **15** in DME results in appearance of intense EPR spectra apparently resulting from radical anion $12^{\cdot-}$ (see the Supporting Information). This is in agreement with the fact that no NMR spectra of **15** could be obtained in CD_2Cl_2 or $[\text{D}_6]$ acetone solution.

The influence of the counter cation, solvent polarity, concentration, and temperature on the σ -dimerization process is currently under investigation.^[38]

Conclusions

A series of stable organic super-acceptors has been synthesized by thermal [2+2] cycloadditions of TCNE, TCNQ, and F_4 -TCNQ to DMA-substituted alkynes bearing either nitrile, dicyanovinyl, or tricyanovinyl functions, followed by retro-electrocyclization of the initially formed cyclobutenes. Despite the nonplanarity of these acceptors, as revealed by X-ray crystallographic analysis (for **1**) and theoretical calculations, efficient intramolecular charge-transfer (CT) interactions are established. The corresponding CT bands appear strongly bathochromically shifted with an end-absorption reaching far into the near infrared region, down to 1600 nm (0.78 eV) for F_4 -TCNQ adduct **7**. Electronic absorption spectra of **1–3**, **5**, **11**, and **12** were calculated by applying the spectroscopy oriented configuration interaction (SORCI) procedure. In most cases the SORCI excitation energies are in good agreement with the experimental UV/Vis spectra recorded in CH_2Cl_2 . The electrochemical investigations of these acceptors by CV and RDV in CH_2Cl_2 identified their remarkable propensity for reversible electron uptake rivaling in some cases even the benchmark compound F_4 -TCNQ ($E_{\text{red},1}=+0.16\text{ V vs. Fc}^+/\text{Fc}$). Furthermore, the electron-

accepting power of the new compounds expressed as adiabatic electron affinity has been estimated by theoretical calculations. Despite the substitution with strong DMA donors, the predicted EAs for acceptors **2** and **7** reach the value calculated for F₄-TCNQ (4.96 eV), which makes these compounds interesting for potential applications as p-type dopants in the fabrication of OLEDs or solar cells.

The first example of a charge-transfer salt between the DMA-substituted TCNQ adduct **12** and strong electron donor decamethylferrocene has been prepared. The X-ray crystallographic analysis revealed that the TCNQ moiety in the acceptor underwent reductive σ -dimerization upon reaction with the donor. Initial investigations by EPR and IR spectroscopy both in the solid state and solution suggest, that the dimeric species dissociates in solution. Detailed investigations of this phenomenon as well as attempts to prepare conductive or magnetic charge-transfer salts between these potent acceptors and various organic and organometallic donors are currently being pursued. We believe that even stronger acceptors are in reach upon careful choice of reacting partners in the [2+2] cycloadditions.

Experimental Section

Materials and general methods: Reagents and solvents were purchased at reagent grade from Acros, Aldrich, and Fluka, and used as received. CH₂Cl₂ was freshly distilled from CaH₂ under N₂. All reactions were performed under an inert atmosphere by applying a positive pressure of N₂. Column chromatography (CC) and plug filtrations were carried out with SiO₂ 60 (particle size 0.040–0.063 mm, 230–400 mesh ASTM; Fluka) or SiO₂ 60 (particle size 0.063–0.200 mm, 70–230 mesh ASTM; Merck) and distilled technical solvents. 3-[4-(Dimethylamino)phenyl]-2-propynenitrile (**8**),^[17,18] 3-[4-(dimethylamino)phenyl]-2-propyn-1-ylidene]propanedinitrile (**9**),^[13b] 4-[4-(dimethylamino)phenyl]-1-buten-3-yne-1,1,2-tricarbonitrile (**10**),^[19] and 3-(dicyanomethylidene)-2-[4-(dimethylamino)phenyl]-1,4-pentadiene-1,1,5,5-tetracarbonitrile (**12**),^[17] were prepared according to literature procedures. Thin-layer chromatography (TLC) was conducted on aluminum sheets coated with SiO₂ 60 F₂₅₄ obtained from Macherey–Nagel; visualization with a UV lamp (254 or 366 nm). Melting points (m.p.) were measured on a Büchi B-540 melting-point apparatus in open capillaries and are uncorrected. ¹H NMR, ¹³C NMR, and ¹⁹F NMR spectra were measured on a Varian Gemini 300 or on a Bruker DRX400 or on a Bruker DRX500 spectrometer at 298 K. Chemical shifts (δ) are reported in ppm relative to the signal of tetramethylsilane (TMS). Residual solvent signals in the ¹H and ¹³C NMR spectra were used as an internal reference. Coupling constants (*J*) are given in Hz. The apparent resonance multiplicity is described as s (singlet), br s (broad singlet), d (doublet), t (triplet), q (quartet), and m (multiplet). Infrared spectra (IR) were recorded on a Perkin–Elmer BX FT-IR spectrometer; signal designations: s (strong), m (medium), w (weak). UV/Vis spectra were recorded on a Varian Cary-5 spectrophotometer. The spectra were measured in CH₂Cl₂ in a quartz cuvette (1 cm) at 298 K. The absorption maxima (λ_{max}) are reported in nm with the extinction coefficient (ϵ) m⁻¹cm⁻¹ in brackets; shoulders are indicated as sh. High-resolution (HR) EI-MS spectra were measured on a Micromass AutoSpec-Ultima spectrometer. HR FT-ICR-MALDI spectra were measured on an IonSpec Ultima Fourier transform (FT) instrument with [(2E)-3-(4-*tert*-butylphenyl)-2-methylprop-2-enylidene]malononitrile (DCTB) or 3-hydroxypicolinic acid (3-HPA) as matrix. HR MALDI-TOF spectra were recorded on a Bruker Ultraflex II mass spectrometer using 7,7,8,8-tetracyanoquinodimethane (TCNQ) as matrix and internal calibration (Bruker High Precision Calibration Mode) with TCNQ ([M]⁺, C₁₂H₄N₄⁺, *m/z* calc. 204.0430; Fluka), terthiophene ([M]⁺, C₁₂H₈S₃⁺, *m/z* calcd 247.9783; Fluka), and hexahy-

dro-2,6-bis(2,2,6,6-tetramethyl-4-piperidinyl)-1,4,4,5,5,8,8H-2,3a,4a,6,7a,8a-hexaazacyclopenta[def]fluor-ene-4,8-dione ([M+H]⁺, C₂₆H₄₆N₈O₂⁺, *m/z* calcd 503.3816; Uvinul 4049 H Ciba Speciality Chemicals). The most important peaks are reported in *m/z* units with *M* as the molecular ion. Thermogravimetric analyses (TGA) were carried out on a TA Instruments TGA Q500 V5.3 instrument in air, at a heating rate of 20°Cmin⁻¹ between 50°C and 900°C. Elemental analyses were performed by the Mikrolabor at the Laboratorium für Organische Chemie, ETH Zürich, with a LECO CHN/900 instrument, fluorine was estimated by ionchromatography on a Metrohm 761 Compact IC instrument, chlorine was estimated by argentometric titration.

Electrochemistry: The electrochemical measurements were carried out at 20°C in CH₂Cl₂, containing 0.1 M *n*Bu₄NPF₆ in a classical three-electrode cell. CH₂Cl₂ was purchased in spectroscopic grade from Merck, dried over molecular sieves (4 Å), and stored under Ar prior to use. *n*Bu₄NPF₆ was purchased in electrochemical grade from Fluka and used as received. The working electrode was a glassy carbon disk electrode (3 mm in diameter) used either motionless for cyclic voltammetry (0.1 to 10 Vs⁻¹) or as rotating-disk electrode for rotating disk voltammetry (RDV). The auxiliary electrode was a Pt wire, and the reference electrode was either an aqueous Ag/AgCl electrode or a platinum wire used as a pseudo-reference electrode. All potentials are referenced to the ferricinium/ferrocene (Fc⁺/Fc) couple, used as an internal standard, and are uncorrected from ohmic drop. The cell was connected to Autolab PGSTAT30 potentiostat (Eco Chemie BV, Utrecht, The Netherlands) controlled by the GPSE software running on a personal computer.

EPR measurements: EPR spectra were recorded on a Bruker ESP 300 X-band spectrometer. All measurements were performed at ambient temperature (ca. 298 K), unless otherwise stated. 1,2-Dimethoxyethane (DME) was heated to reflux over Na/K alloy and stored over Na/K alloy under high vacuum. [D₆]acetone was used as received. Compounds **2**, **6**, and **7** were dissolved in [D₆]acetone and deoxygenated thoroughly by argon bubbling through for 10 min. Reduction of **5** was performed by contact of the DME solution of the parent compound with a K-metal mirror under high vacuum.

Calculations: Electronic absorption spectra of **1–3**, **5**, **11**, and **12** were calculated by applying the spectroscopy oriented configuration interaction (SORCI)^[24] procedure implemented in the ORCA program suite.^[25] The geometries of all molecules were optimized by using the TURBOMOLE program suite, version 5.10^[40] at the BP86/def-SV(P) level. A single-point Hartree–Fock calculation using the TZVP basis set^[41] was performed to generate the input for the SORCI calculation. The active space was constructed from all Slater determinants distributing altogether six electrons in the HOMO–2, HOMO–1, HOMO, LUMO, and LUMO+1 of the Hartree–Fock calculation, preserving the HF-occupation of all other orbitals. The three configuration selection parameters were set to 10⁻⁶ (tsel), 10⁻⁴ (tpre), and 10⁻⁵ (tnat), respectively.

X-ray analysis: The structures were solved by direct methods (SIR-97)^[42] and refined by full-matrix least-squares analysis (SHELXL-97)^[43] using an isotropic extinction correction. All non hydrogen atoms were refined anisotropically; hydrogen atoms were refined isotropically, whereby hydrogen positions are based on stereochemical considerations.

X-ray crystal structure of 1: Crystal data at 220(2) K for C₂₀H₁₁N₇, *M*_r = 349.36, triclinic, space group *P* $\bar{1}$, ρ_{calcd} = 1.278 g cm⁻³, *Z* = 2, *a* = 7.0331(18), *b* = 7.7652(19), *c* = 16.756(2) Å, α = 86.996(14), β = 83.408(15), γ = 88.385(16)°, *V* = 907.6(3) Å³. Bruker–Nonius Kappa-CCD diffractometer, MoK α radiation, λ = 0.7107 Å, μ = 0.082 mm⁻¹. A black crystal of **1** (linear dimensions ca. 0.16 × 0.07 × 0.06 mm) was obtained by slow diffusion of *n*-hexane into a solution of **1** in CH₂Cl₂. Numbers of measured and unique reflections are 3942 and 2466, respectively (*R*_{int} = 0.062). Final *R*(*F*) = 0.072, *wR*(*F*²) = 0.168 for 247 parameters and 1636 reflections with *I* > 2 σ (*I*) and 2.92 < θ < 23.23° (corresponding *R* values based on all 2466 reflections are 0.112 and 0.193, respectively).

X-ray crystal structure of 15: Crystal data at 220(2) K for 2(C₄₆H₂₈N₁₂)-4-(C₂₀H₃₀Fe)-2.5(CH₂Cl₂), *M*_r = 3010.04, monoclinic, space group *P*2₁/*c* (no. 14), ρ_{calcd} = 1.226 g cm⁻³, *Z* = 4, *a* = 21.8649(13), *b* = 31.0432(15), *c* = 26.3554(14) Å, β = 114.293(11)°, *V* = 16305(2) Å³. Bruker–Nonius Kappa-CCD diffractometer, MoK α radiation, λ = 0.7107 Å, μ =

0.489 nm⁻¹. A green crystal of **15** (linear dimensions ca. 0.15 × 0.09 × 0.05 mm) was obtained by slow diffusion of *n*-hexane into a solution of **15** in CH₂Cl₂. Numbers of measured and unique reflections are 33275 and 19452, respectively ($R_{\text{int}}=0.044$). Final $R(F)=0.072$, $wR(F^2)=0.165$ for 1949 parameters and 14056 reflections with $I > 2\sigma(I)$ and $1.66 < \theta < 21.98^\circ$ (corresponding R values based on all 19452 reflections are 0.106 and 0.186, respectively). CCDC-711841 (**1**) and CCDC-711842 (**15**) contain the supplementary crystallographic data for this paper. These data can be obtained free of charge from The Cambridge Crystallographic Data Centre via www.ccdc.cam.ac.uk/data_request/cif.

Silylation of glass surfaces with dimethyldichlorosilane (DMDCS).^[21] The glassware was soaked in a toluene solution of DMDCS (5% v/v) for 15 min at 25 °C. Subsequently, the glassware was rinsed twice with toluene, soaked for 15 min in MeOH, rinsed with MeOH, and finally dried in a nitrogen stream.

3-[(Dicyanomethylidene)-2-[4-(dimethylamino)phenyl]-1,4-pentadiene-1,1,5,5-tetracarboxitrile (1): TCNE (48 mg, 0.380 mmol) was added to a solution of **9** (42 mg, 0.190 mmol) in 1,2-dichloroethane (35 mL). The mixture was stirred for 16 h at 60 °C. The solvent was evaporated in vacuo to afford a black solid that was purified by repeated (3 ×) slow diffusion of *n*-hexane into CH₂Cl₂ solution at 25 °C. Subsequent CC (SiO₂, CH₂Cl₂→CH₂Cl₂/EtOAc 95:5; decomp) afforded **1** (17 mg, 26%) as a black metallic-like solid. $R_f=0.48$ (SiO₂, CH₂Cl₂/EtOAc 95:5; decomp); m.p. > 250 °C (decomp); ¹H NMR (500 MHz, CD₂Cl₂): $\delta=3.21$ (s, 6H), 6.80 (d, $J=9.4$ Hz, 2H), 7.67 (d, $J=9.4$ Hz, 2H), 8.02 ppm (s, 1H); ¹³C NMR (125 MHz, CD₂Cl₂): $\delta=40.83, 74.33, 97.59, 100.24, 109.54, 109.82, 110.22, 112.27, 113.36, 114.22, 114.32, 117.29, 132.97, 147.72, 155.16, 155.85, 158.85$ ppm; IR (neat): $\tilde{\nu}=3031$ (w), 2923 (w), 2852 (w), 2214 (s), 1603 (s), 1476 (s), 1457 (s), 1382 (s), 1359 (s), 1275 (m), 1218 (s), 1167 (s), 1059 (m), 943 (m), 898 (w), 825 cm⁻¹ (s); UV/Vis (CH₂Cl₂): $\lambda_{\text{max}}(\epsilon)=317$ (21400), 304 (25000), 486 nm (43300 M⁻¹ cm⁻¹); HR-MALDI-MS (DCTB): m/z calcd for C₂₀H₁₁N₇⁺ [M]⁺: 349.1081; found: 349.1084.

3-[(Dicyanomethylidene)-4-[4-(dimethylamino)phenyl]-1,4-pentadiene-1,1,2,5,5-pentacarboxitrile (2): TCNE (13 mg, 0.101 mmol) was added to a solution of **10** (25 mg, 0.101 mmol) in 1,1,2,2-tetrachloroethane (15 mL), and the mixture was stirred for two days at 120 °C. After that time, *n*-hexane (20 mL) was added slowly forming a second layer on the top of the reaction solution and the mixture was allowed to stand for two days at 25 °C. The mother liquor was carefully removed using a Pasteur pipette, and the solid was washed with *n*-hexane. Repeated (3 ×) crystallization by slow diffusion of *n*-hexane into CH₂Cl₂ solution at 25 °C afforded **2** (25 mg, 66%) as a black solid. R_f not determined due to rapid decomposition on SiO₂; m.p. > 232 °C (decomp); ¹H NMR and ¹³C NMR not available due to contamination with paramagnetic species and low solubility of the solid; IR (neat): $\tilde{\nu}=2923$ (w), 2214 (m), 1601 (s), 1485 (s), 1437 (m), 1375 (s), 1191 (s), 1171 (s), 1121 (m), 1064 (w), 941 (w), 822 cm⁻¹ (w); UV/Vis (CH₂Cl₂): $\lambda_{\text{max}}(\epsilon)=295$ (15400), 469 (16300), 657 nm (5600, M⁻¹ cm⁻¹); HR-MALDI-MS (DCTB): m/z calcd for C₂₁H₁₀N₈⁺ [M]⁺: 374.1023; found: 374.1028.

2-[[4-(Dicyanomethylidene)-2,5-cyclohexadien-1-ylidene][4-(dimethylamino)phenyl]methyl]-1,3-butadiene-1,1,4,4-tetracarboxitrile (3): TCNQ (92 mg, 0.450 mmol) was added to a solution of **9** (50 mg, 0.226 mmol) in 1,2-dichloroethane (35 mL). The mixture was stirred for five days at 60 °C. The solvent was evaporated in vacuo and the residue purified by repeated (3 ×) slow diffusion of *n*-hexane into CH₂Cl₂ solution at 20 °C. The obtained solid was divided into four portions, which were individually purified by multiple CC (SiO₂, 3 × CH₂Cl₂→CH₂Cl₂/EtOAc 1:1; decomp) to afford **3** (13 mg, 14%) as a deep-blue metallic-like solid. $R_f=0.43$ (SiO₂, CH₂Cl₂/EtOAc 1:1; decomp); m.p. 140–142 °C; ¹H NMR (400 MHz, 1,1,2,2-[D₂]tetrachloroethane): $\delta=3.11$ (s, 6H), 6.70–6.74 (m, 3H), 7.13 (d, $J=9.2$ Hz, 2H), 7.21 (dd, $J=9.5, 1.9$ Hz, 1H), 7.27 (dd, $J=9.5, 1.9$ Hz, 1H), 7.40 (dd, $J=9.5, 1.9$ Hz, 1H), 7.96 ppm (s, 1H); ¹³C NMR (125 MHz, 1,1,2,2-[D₂]tetrachloroethane): $\delta=40.59, 97.26, 98.05, 109.48, 110.49, 110.62, 111.99, 113.40, 114.89, 122.14, 126.21, 126.71, 133.18, 133.29, 135.09, 135.65, 143.32, 151.10, 153.65, 153.77, 161.78$ ppm; IR (neat): $\tilde{\nu}=2857$ (w), 2198 (s), 1607 (w), 1575 (s), 1519 (m), 1395 (m), 1367 (s), 1347 (s), 1162 (s), 1002 (w), 940 (m), 909 (m), 820 cm⁻¹ (m);

UV/Vis (CH₂Cl₂): $\lambda_{\text{max}}(\epsilon)=379$ (sh, 68000), 400 (108400), 633 (13900), 930 nm (1400 M⁻¹ cm⁻¹); HR-MALDI-TOF-MS (TCNQ): m/z calcd for C₂₆H₁₅N₇⁺ [M]⁺: 425.1383; found: 425.1374.

3-[4-(Dicyanomethylidene)-2,3,5,6-tetrafluoro-2,5-cyclohexadien-1-ylidene]-3-[4-(dimethylamino)phenyl]-1-propene-1,1,2-tricarboxitrile (5): F₄-TCNQ (57 mg, 0.206 mmol) was added to a solution of **8** (35 mg, 0.206 mmol) in CH₂Cl₂ (50 mL) in a flask deactivated with DMDCS. The mixture was stirred for 17 h at 25 °C. After that time, *n*-hexane (50 mL) was added slowly forming a second layer on the top of the reaction solution and the mixture was allowed to stand for two days at 25 °C. The mother liquor was carefully removed using a Pasteur pipette, and the solid was washed with *n*-hexane. Repeated (3 ×) crystallization by slow diffusion of *n*-hexane into CH₂Cl₂ solution at 25 °C afforded **5** (60 mg, 65%) as a black metallic-like solid. $R_f=0.13$ (SiO₂, CH₂Cl₂/EtOAc 95:5; decomp); m.p. > 410 °C (decomp); ¹H NMR (300 MHz, CD₂Cl₂): $\delta=3.39$ (s, 6H), 6.95 (d, $J=9.4$ Hz, 2H), 7.33 ppm (d, $J=9.4$ Hz, 2H); ¹³C NMR (125 MHz, CD₂Cl₂): not available due to low solubility of the solid; ¹⁹F NMR (282 MHz, CD₂Cl₂): $\delta=-140.53$ (m), -133.24 ppm (brs); IR (neat): $\tilde{\nu}=2652$ (w), 2197 (s), 2181 (m), 1635 (m), 1602 (s), 1532 (m), 1387 (s), 1271 (s), 1200 (s), 1161 (s), 1072 (m), 978 (m), 960 (m), 869 (w), 834 (s), 822 cm⁻¹ (m); UV/Vis (CH₂Cl₂): $\lambda_{\text{max}}(\epsilon)=330$ (12400), 370 (sh, 9300), 391 (12200), 539 (25600), 993 nm (22300 M⁻¹ cm⁻¹); HR-MALDI-TOF-MS (TCNQ): m/z calcd for C₂₃H₁₀N₆F₄⁺ [M]⁺: 446.0898; found: 446.0886; elemental analysis calcd (%) for C₂₃H₁₀N₆F₄ (446.37): C 61.89, H 2.26, N 18.83, F 17.02; found: C 61.92, H 2.43, N 18.65, F 17.12.

2-[[4-(Dicyanomethylidene)-2,3,5,6-tetrafluoro-2,5-cyclohexadien-1-ylidene][4-(dimethylamino)phenyl]methyl]-1,3-butadiene-1,1,4,4-tetracarboxitrile (6): F₄-TCNQ (62 mg, 0.225 mmol) was added to a solution of **9** (50 mg, 0.226 mmol) in CH₂Cl₂ (40 mL) in a flask deactivated with DMDCS. The mixture was stirred for 16 h at 25 °C. After that time, *n*-hexane (50 mL) was added and the mixture was allowed to stand for two days at 25 °C. The mother liquor was carefully removed, the solid was washed with *n*-hexane (3 ×) and dried in vacuo to give **6** (94 mg, 84%) as a copper-like solid. $R_f=0.12$ (SiO₂, CH₂Cl₂/EtOAc 95:5; decomp); m.p. > 270 °C (decomp); ¹H NMR, ¹³C NMR, and ¹⁹F NMR not available due to contamination with paramagnetic species and low solubility of the solid; IR (neat): $\tilde{\nu}=3039$ (w), 2925 (w), 2662 (w), 2189 (s), 2162 (s), 1635 (m), 1603 (s), 1505 (s), 1480 (m), 1401 (s), 1357 (s), 1222 (s), 1179 (s), 1079 (m), 1002 (s), 964 (s), 920 (m), 859 (m), 833 cm⁻¹ (s); UV/Vis (CH₂Cl₂): $\lambda_{\text{max}}(\epsilon)=289$ (sh, 20600), 321 (27000), 697 (40600), 942 nm (17000 M⁻¹ cm⁻¹); HR-MALDI-TOF-MS (TCNQ): m/z calcd for C₂₆H₁₁N₇F₄⁺ [M]⁺: 497.1007; found: 497.1019; elemental analysis calcd (%) for C₂₆H₁₁N₇F₄ (497.41): C 62.78, H 2.23, N 19.71, F 15.28; found: C 62.28, H 2.37, N 19.27, F 15.34.

3-[[4-(Dicyanomethylidene)-2,3,5,6-tetrafluoro-2,5-cyclohexadien-1-ylidene][4-(dimethylamino)phenyl]methyl]-1,3-butadiene-1,1,2,4,4-pentacarboxitrile (7): F₄-TCNQ (17 mg, 0.061 mmol) was added to a solution of **10** (15 mg, 0.061 mmol) in CH₂Cl₂ (10 mL) in a flask deactivated with DMDCS. The mixture was stirred for five days at 25 °C. After that time, *n*-hexane (10 mL) was added slowly forming a second layer on the top of the reaction solution and the mixture was allowed to stand for three days at 25 °C. The mother liquor was carefully removed using a Pasteur pipette, and the solid was washed with *n*-hexane. Repeated (3 ×) crystallization by slow diffusion of *n*-hexane into CH₂Cl₂ solution at 25 °C afforded **7** (28 mg, 88%) as a black metallic-like solid. R_f not determined due to rapid decomposition on SiO₂; m.p. > 360 °C (decomp); ¹H NMR, ¹³C NMR, and ¹⁹F NMR not available due to contamination with paramagnetic species and low solubility of the solid; IR (neat): $\tilde{\nu}=2196$ (s), 2171 (m), 1633 (m), 1595 (s), 1502 (m), 1476 (m), 1352 (s), 1304 (s), 1200 (s), 1171 (s), 1111 (m), 1030 (m), 972 (m), 869 (w), 836 cm⁻¹ (w); UV/Vis (CH₂Cl₂): $\lambda_{\text{max}}(\epsilon)=306$ (sh, 15900), 342 (19400), 420 (11800), 753 (36700), 1120 nm (9400 M⁻¹ cm⁻¹); HR-MALDI-TOF-MS (TCNQ): m/z calcd for C₂₇H₁₀N₈F₄⁺ [M]⁺: 522.0959; found: 522.0960.

Charge-transfer salt ([FeCp*₂]⁺)₂[12]₂²⁻·1.4 CH₂Cl₂ (15): To a solution of **12** (50.0 mg, 0.133 mmol) in dry MeCN (20 mL), [FeCp*₂]⁺ (43.4 mg, 0.133 mmol) in dry CH₂Cl₂ (10 mL) was added dropwise. The originally purple solution became intense green while stirred for 30 min at 25 °C. The solvent was evaporated in vacuo and the dark residue dissolved in

CH₂Cl₂ (15 mL). *n*-Hexane (ca. 15 mL) was added slowly on the top of the CH₂Cl₂ solution forming a second layer, and the mixture was allowed to stand for five days at 0°C. The formed solid was collected by filtration, washed with *n*-hexane, and dried in vacuo (2×10^{-6} mbar) to give an analytical sample of **15** (69.2 mg, 68%) as dark green crystals readily soluble in CH₂Cl₂. Crystals of **15** in equilibrium with the supernatant were used for X-ray crystallographic analysis to prevent loss of co-crystallized solutes. Interestingly, red-brown crystals that were obtained in comparable yields in different runs, featured identical elemental composition and crystallographic parameters as the original sample of **15**. M.p. > 170°C (decomp); IR (neat): $\tilde{\nu}$ = 2961 (w), 2920 (w), 2853 (w), 2796 (w), 2169 (s), 2129 (s), 1601 (s), 1581 (s), 1519 (s), 1476 (m), 1444 (m), 1424 (m), 1338 (s), 1283 (s), 1172 (s), 1124 (m), 1061 (m), 1022 (m), 945 (m), 905 (w), 834 (m), 822 (m), 806 cm⁻¹ (m); IR (CHCl₃): $\tilde{\nu}$ = 3010 (m), 2920 (w), 2868 (w), 2178 (s), 1601 (m), 1582 (s), 1525 (w), 1505 (w), 1477 (w), 1424 (m), 1356 (s), 1334 (s), 1182 (m), 1174 (m), 1022 (w), 989 (w), 946 (w), 904 (w), 839 cm⁻¹ (w); UV/Vis (CH₂Cl₂): λ_{max} (ϵ) = 277 (52500), 320 (sh, 37700), 437 (33700), 470 (sh, 29000), 620 (39600), 690 (sh, 26000), 1307 nm (28300 M⁻¹cm⁻¹); elemental analysis calcd (%) for C₆₆H₈₈N₁₂Fe₂·1.4 CH₂Cl₂ (1520.29): C 69.05, H 6.02, N 11.06, Cl 6.53; found: C 69.11, H 6.31, N 11.11, Cl 6.54.

Acknowledgement

This research was supported by the ETH Research Council, the NCCR "Nanoscale Science", Basel, and FWF (Austria, project no. P20019). B. E. thanks the "Doktorandinnenkolleg FreChe Materie" for her scholarship. Prof. Dr. P. Walde and Dr. T. Schweizer (ETH Zurich) are gratefully acknowledged for the TGA measurements, and L. Bertschi (ETHZ) for the measurements of the challenging MALDI-TOF spectra. We thank Prof. Dr. J. S. Miller (University of Utah) for many fruitful discussions.

- [1] For selected reviews on cyano-based acceptors, see: a) T. L. Cairns, B. C. McKusick, *Angew. Chem.* **1961**, *73*, 520–525; b) W. R. Hertler, W. Mahler, L. R. Melby, J. S. Miller, R. E. Putscher, O. W. Webster, *Mol. Cryst. Liq. Cryst.* **1989**, *171*, 205–216; c) O. W. Webster, *J. Polym. Sci. Part A: Polym. Chem.* **2002**, *40*, 210–221.
- [2] T. L. Cairns, R. A. Carboni, D. D. Coffman, V. A. Engelhardt, R. E. Heckert, E. L. Little, E. G. McGeer, B. C. McKusick, W. J. Middleton, *J. Am. Chem. Soc.* **1957**, *79*, 2340–2341.
- [3] For selected reviews on the chemistry of TCNE, see: a) A. J. Fatiadi, *Synthesis* **1986**, 249–284; b) A. J. Fatiadi, *Synthesis* **1987**, 749–789; c) A. J. Fatiadi, *Synthesis* **1987**, 959–978; d) J. S. Miller, *Angew. Chem.* **2006**, *118*, 2570–2588; *Angew. Chem. Int. Ed.* **2006**, *45*, 2508–2525.
- [4] a) D. S. Acker, R. J. Harder, W. R. Hertler, W. Mahler, L. R. Melby, R. E. Benson, W. E. Mochel, *J. Am. Chem. Soc.* **1960**, *82*, 6408–6409; b) D. S. Acker, W. R. Hertler, *J. Am. Chem. Soc.* **1962**, *84*, 3370–3374.
- [5] For selected reviews on the chemistry of TCNQ, see: a) B. P. Bespalov, V. V. Titov, *Russ. Chem. Rev.* **1975**, *44*, 1091–1108; b) W. Kaim, M. Moscherosch, *Coord. Chem. Rev.* **1994**, *129*, 157–193.
- [6] a) R. C. Wheland, E. L. Martin, *J. Org. Chem.* **1975**, *40*, 3101–3109; b) N. Martín, J. L. Segura, C. Seoane, *J. Mater. Chem.* **1997**, *7*, 1661–1676; c) S. Hünig, E. Herberth, *Chem. Rev.* **2004**, *104*, 5535–5563; d) R. Gómez, C. Seoane, J. L. Segura, *Chem. Soc. Rev.* **2007**, *36*, 1305–1322.
- [7] For reviews on organic conductors, see: a) Special issue on Molecular Conductors: *Chem. Rev.* **2004**, *104*, 4887–5782, edited by P. Batail; b) T. Otsubo, K. Takimiya, *Bull. Chem. Soc. Jpn.* **2004**, *77*, 43–58; c) G. Saito, Y. Yoshida, *Bull. Chem. Soc. Jpn.* **2007**, *80*, 1–137.
- [8] For some specific references to organic conductors, see: a) J. Ferraris, D. O. Cowan, V. Walatka, Jr., J. H. Perlstein, *J. Am. Chem. Soc.* **1973**, *95*, 948–949; b) R. C. Wheland, J. L. Gillson, *J. Am. Chem. Soc.* **1976**, *98*, 3916–3925; c) T. Imakubo, M. Kibune, H. Yoshino, T. Shirahata, K. Yoza, *J. Mater. Chem.* **2006**, *16*, 4110–4116; d) T. Murata, Y. Morita, Y. Yakiyama, K. Fukui, H. Yamochi, G. Saito, K. Nakasuji, *J. Am. Chem. Soc.* **2007**, *129*, 10837–10846; e) H. Alves, A. S. Molinari, H. Xie, A. F. Morpurgo, *Nat. Mater.* **2008**, *7*, 574–580.
- [9] a) J. S. Miller, J. C. Calabrese, H. Rommelmann, S. R. Chittipeddi, J. H. Zhang, W. M. Reiff, A. J. Epstein, *J. Am. Chem. Soc.* **1987**, *109*, 769–781; b) J. S. Miller, *Inorg. Chem.* **2000**, *39*, 4392–4408; c) J. A. Crayston, J. N. Devine, J. C. Walton, *Tetrahedron* **2000**, *56*, 7829–7857; d) N. Lopez, H. Zhao, A. V. Prosvirin, A. Chouai, M. Shatruck, K. R. Dunbar, *Chem. Commun.* **2007**, 4611–4613.
- [10] a) M. Pfeiffer, K. Leo, X. Zhou, J. S. Huang, M. Hofmann, A. Werner, J. Blochwitz-Nimoth, *Org. Electron.* **2003**, *4*, 89–103; b) K. Walzer, B. Maennig, M. Pfeiffer, K. Leo, *Chem. Rev.* **2007**, *107*, 1233–1271.
- [11] Z. Q. Gao, B. X. Mi, G. Z. Xu, Y. Q. Wan, M. L. Gong, K. W. Cheah, C. H. Chen, *Chem. Commun.* **2008**, 117–119.
- [12] M. I. Bruce, J. R. Rodgers, M. R. Snow, A. G. Swincer, *J. Chem. Soc. Chem. Commun.* **1981**, 271–272.
- [13] For some recent work on TCNE cycloadditions, see: a) Y. Morioka, N. Yoshizawa, J.-i. Nishida, Y. Yamashita, *Chem. Lett.* **2004**, *33*, 1190–1191; b) T. Michinobu, J. C. May, J. H. Lim, C. Boudon, J.-P. Gisselbrecht, P. Seiler, M. Gross, I. Biaggio, F. Diederich, *Chem. Commun.* **2005**, 737–739; c) T. Michinobu, C. Boudon, J.-P. Gisselbrecht, P. Seiler, B. Frank, N. N. P. Moonen, M. Gross, F. Diederich, *Chem. Eur. J.* **2006**, *12*, 1889–1905; d) M. Kivala, C. Boudon, J.-P. Gisselbrecht, P. Seiler, M. Gross, F. Diederich, *Angew. Chem.* **2007**, *119*, 6473–6477; *Angew. Chem. Int. Ed.* **2007**, *46*, 6357–6360; e) J. L. Alonso-Gómez, P. Schanen, P. Rivera-Fuentes, P. Seiler, F. Diederich, *Chem. Eur. J.* **2008**, *14*, 10564–10568; f) J. Xu, X. Liu, J. Lv, M. Zhu, C. Huang, W. Zhou, X. Yin, H. Liu, Y. Li, J. Ye, *Langmuir* **2008**, *24*, 4231–4237; g) T. Shoji, S. Ito, K. Toyota, M. Yasunami, N. Morita, *Chem. Eur. J.* **2008**, *14*, 8398–8408; h) D. J. Armit, M. I. Bruce, B. W. Skelton, A. H. White, *Organometallics* **2008**, *27*, 3556–3563; i) T. Michinobu, *J. Am. Chem. Soc.* **2008**, *130*, 14074–14075.
- [14] K.-i. Onuma, Y. Kai, N. Yasuoka, N. Kasai, *Bull. Chem. Soc. Jpn.* **1975**, *48*, 1696–1700.
- [15] For some recent work on TCNQ cycloadditions, see: a) M. Kivala, C. Boudon, J.-P. Gisselbrecht, P. Seiler, M. Gross, F. Diederich, *Chem. Commun.* **2007**, 4731–4733; b) W. Zhou, J. Xu, H. Zheng, H. Liu, Y. Li, D. Zhu, *J. Org. Chem.* **2008**, *73*, 7702–7709; c) K. Tahara, T. Fujita, M. Sonoda, M. Shiro, Y. Tobe, *J. Am. Chem. Soc.* **2008**, *130*, 14339–14345.
- [16] R. L. Cordiner, M. E. Smith, A. S. Batsanov, D. Albesa-Jové, F. Hartl, J. A. K. Howard, P. J. Low, *Inorg. Chim. Acta* **2006**, *359*, 946–961.
- [17] P. Reutenauer, M. Kivala, P. D. Jarowski, C. Boudon, J.-P. Gisselbrecht, M. Gross, F. Diederich, *Chem. Commun.* **2007**, 4898–4900.
- [18] G. D. McAllister, C. D. Wilfred, R. J. K. Taylor, *Synlett* **2002**, 1291–1292.
- [19] N. N. P. Moonen, W. C. Pomerantz, R. Gist, C. Boudon, J.-P. Gisselbrecht, T. Kawai, A. Kishioka, M. Gross, M. Irie, F. Diederich, *Chem. Eur. J.* **2005**, *11*, 3325–3341. Well-reproducible yields of **10** (19%) were obtained with freshly prepared copper(I) acetate only, see: D. A. Edwards, R. Richards, *J. Chem. Soc. Dalton Trans.* **1973**, 2463–2468.
- [20] N. G. Connelly, W. E. Geiger, *Chem. Rev.* **1996**, *96*, 877–910.
- [21] F. Deyhimi, J. A. Coles, *Helv. Chim. Acta* **1982**, *65*, 1752–1759.
- [22] C. Dehu, F. Meyers, J. L. Brédas, *J. Am. Chem. Soc.* **1993**, *115*, 6198–6206.
- [23] For examples of organic molecules with exceptionally small HOMO–LUMO gaps, see: a) A. Tsuda, A. Osuka, *Adv. Mater.* **2002**, *14*, 75–79; b) D. Bonifazi, G. Accorsi, N. Armaroli, F. Song, A. Palkar, L. Echegoyen, M. Scholl, P. Seiler, B. Jaun, F. Diederich, *Helv. Chim. Acta* **2005**, *88*, 1839–1884; c) D. F. Perepichka, M. R. Bryce, *Angew. Chem.* **2005**, *117*, 5504–5507; *Angew. Chem. Int. Ed.* **2005**, *44*, 5370–5373.
- [24] F. Neese, *J. Chem. Phys.* **2003**, *119*, 9428–9443.

- [25] F. Neese, ORCA—An ab initio, DFT, and semiempirical SCF-MO package, Version 2.5, revision 20 (29.01.2007), Max Planck Institute für Strahlenchemie, Mülheim, **2003**.
- [26] C. Diaz, A. Arancibia, *Polyhedron* **2000**, *19*, 137–145.
- [27] Comparable anodic shifts were observed upon CN-substitution in porphyrins, see: a) A. Giraudeau, I. Ezahr, M. Gross, H. J. Callot, J. Jordan, *Bioelectrochem. Bioenerg.* **1976**, *3*, 519–527; b) H. J. Callot, A. Giraudeau, M. Gross, *J. Chem. Soc. Perkin Trans. 2* **1975**, 1321–1324.
- [28] For redox properties of TCNQ vs. F₄-TCNQ, see: A. F. Garito, A. J. Heeger, *Acc. Chem. Res.* **1974**, *7*, 232–240.
- [29] C. Hansch, A. Leo, R. W. Taft, *Chem. Rev.* **1991**, *91*, 165–195.
- [30] A. Klamt, G. Schüürmann, *J. Chem. Soc. Perkin Trans. 2* **1993**, 799–805.
- [31] The calculated EA for F₄-TCNQ (4.96 eV) using the BP86/def-TZVP COSMO($\epsilon=4.5$)/BP86/def-SV(P) method is in good agreement with the reported value obtained experimentally (5.24 eV) by inverse photoemission spectroscopy (IPES). For the experimental EA of F₄-TCNQ, see: W. Gao, A. Kahn, *Appl. Phys. Lett.* **2001**, *79*, 4040–4042.
- [32] a) W. D. Phillips, J. C. Rowell, S. I. Weissman, *J. Chem. Phys.* **1960**, *33*, 626–627; b) F. Gerson, R. Heckendorn, D. O. Cowan, A. M. Kini, M. Maxfield, *J. Am. Chem. Soc.* **1983**, *105*, 7017–7023.
- [33] For selected examples of TCNQ σ -dimers, see: a) V. Dong, H. Endres, H. J. Keller, W. Moroni, D. Nöthe, *Acta. Crystallogr. Sect. B.* **1977**, *33*, 2428–2431; b) B. Morosin, H. J. Plastas, L. B. Coleman, J. M. Stewart, *Acta. Crystallogr. Sect. B.* **1978**, *34*, 540–543; c) S. K. Hoffmann, P. J. Corvan, P. Singh, C. N. Sethulekshmi, R. M. Metzger, W. E. Hatfield, *J. Am. Chem. Soc.* **1983**, *105*, 4608–4617; d) H. Zhao, R. A. Heintz, K. R. Dunbar, *J. Am. Chem. Soc.* **1996**, *118*, 12844–12845; e) S. Mikami, K.-i. Sugiura, J. S. Miller, Y. Sakata, *Chem. Lett.* **1999**, 413–414; f) C. Alonso, L. Ballester, A. Gutiérrez, M. F. Perpiñán, A. E. Sánchez, M. T. Azcondo, *Eur. J. Inorg. Chem.* **2005**, 486–495; g) S. Shimomura, S. Horike, R. Matsuda, S. Kitagawa, *J. Am. Chem. Soc.* **2007**, *129*, 10990–10991.
- [34] The estimated standard deviations (ESDs) from least squares refinement are nearly the same for both independent [12]₂²⁻ molecules (**A** and **B**) and range from 0.004 to 0.006 Å. For the three ordered [FeCp*₂]⁺ molecules, the ESDs for Fe–C and C–C bond lengths range from 0.003 to 0.005 Å and from 0.004 to 0.007 Å, respectively. The experimental bond lengths correspond to the average of both independent [12]₂²⁻ molecules **A** and **B**.
- [35] a) M. Decoster, F. Conan, M. Kubicki, Y. Le Mest, P. Richard, J. S. Pala, L. Toupet, *J. Chem. Soc. Perkin Trans. 2* **1997**, 265–271; b) S. Duclos, F. Conan, S. Triki, Y. Le Mest, M. L. Gonzales, J. S. Pala, *Polyhedron* **1999**, *18*, 1935–1939.
- [36] Gaussian 03, Revision C.02, M. J. Frisch, G. W. Trucks, H. B. Schlegel, G. E. Scuseria, M. A. Robb, J. R. Cheeseman, J. Montgomery, Jr., T. Vreven, K. N. Kudin, J. C. Burant, J. M. Millam, S. S. Iyengar, J. Tomasi, V. Barone, B. Mennucci, M. Cossi, G. Scalmani, N. Rega, G. A. Petersson, H. Nakatsuji, M. Hada, M. Ehara, K. Toyota, R. Fukuda, J. Hasegawa, M. Ishida, T. Nakajima, Y. Honda, O. Kitao, H. Nakai, M. Klene, X. Li, J. E. Knox, H. P. Hratchian, J. B. Cross, C. Adamo, V. Bakken, C. Adamo, J. Jaramillo, R. Gomperts, R. E. Stratmann, O. Yazyev, A. J. Austin, R. Cammi, C. Pomelli, J. W. Ochterski, P. Y. Ayala, K. Morokuma, G. A. Voth, P. Salvador, J. J. Dannenberg, V. G. Zakrzewski, S. Dapprich, A. D. Daniels, M. C. Strain, O. Farkas, D. K. Malick, A. D. Rabuck, K. Raghavachari, J. B. Foresman, J. V. Ortiz, Q. Cui, A. G. Baboul, S. Clifford, J. Cioslowski, B. B. Stefanov, G. Liu, A. Liashenko, P. Piskorz, I. Komaromi, R. L. Martin, D. J. Fox, T. Keith, M. A. Al-Laham, C. Y. Peng, A. Nanayakkara, M. Challacombe, P. M. W. Gill, B. Johnson, W. Chen, M. W. Wong, C. Gonzalez, J. A. Pople, Gaussian, Inc., Wallingford CT, **2004**.
- [37] A. H. Reis, Jr., L. D. Preston, J. M. Williams, S. W. Peterson, G. A. Candela, L. J. Swartzendruber, J. S. Miller, *J. Am. Chem. Soc.* **1979**, *101*, 2756–2758.
- [38] a) J.-M. Lü, S. V. Rosokha, J. K. Kochi, *J. Am. Chem. Soc.* **2003**, *125*, 12161–12171; b) T. Nishinaga, K. Komatsu, *Org. Biomol. Chem.* **2005**, *3*, 561–569.
- [39] a) H. Zhao, R. A. Heintz, X. Ouyang, K. R. Dunbar, C. F. Campana, R. D. Rogers, *Chem. Mater.* **1999**, *11*, 736–746; b) L. Ballester, A. Gutiérrez, M. F. Perpiñán, M. T. Azcondo, A. E. Sánchez, *Synth. Met.* **2001**, *120*, 965–966.
- [40] Electronic Structure Calculations on Workstation Computers: The Program System TURBOMOLE, see: R. Ahlrichs, M. Bär, M. Häser, H. Horn, C. Kölmel, *Chem. Phys. Lett.* **1989**, *162*, 165–169.
- [41] A. Schäfer, C. Huber, R. Ahlrichs, *J. Chem. Phys.* **1994**, *100*, 5829–5835.
- [42] A. Altomare, M. C. Burla, M. Camalli, G. L. Cascarano, C. Giacovazzo, A. Guagliardi, A. G. G. Moliterni, G. Polidori, R. Spagna, *J. Appl. Crystallogr.* **1999**, *32*, 115–119.
- [43] G. M. Sheldrick, SHELXL-97, Program for the Refinement of Crystal Structures, University of Göttingen, Germany, **1997**.

Received: December 6, 2008
Published online: March 5, 2009

List of Figures

1.1	General mechanism of polymer photo-oxidative degradation	5
1.2	Intramolecular photoaddition of Riboflavin ⁸	6
1.3	Photolysis reactions of Riboflavin ⁸	7
1.4	General mechanism of the photocatalysis on TiO ₂ nanomaterials ¹⁴	8
1.5	Overview of generation and application of ¹ O ₂	9
1.6	Jablonski Diagram.	10
1.7	2,2,6,6-Tetramethylpiperidine.	14
1.8	Acid-base equilibrium between Ammonia and Eosin ⁵⁰	18
1.9	Stern-Volmer relation.	19
1.10	Fluorescein.	25
1.11	Coumarin.	25
1.12	“On-off” sensing mechanism for Cu ²⁺ ⁷³	26
1.13	HPTS.	26
1.14	Transition metal complexes.	27
2.1	Absorption spectroscopy measurement setup.	31
2.2	Reaction of TEMP and ¹ O ₂ , giving TEMPO.	32
2.3	EPR signal of TEMPO.	33
2.4	¹ O ₂ sensitizers.	35
2.5	Normalized absorption spectra of A	35
2.6	Investigated dyes (B).	37
2.7	Relative absorption maximum of B vs. irradiation time.	39
2.8	Absorption spectra of B ; Irradiation of A : ¹ O ₂ surplus, B in ground state. (continued on next page)	41
2.8	(continued) Absorption spectra of B ; Irradiation of A : ¹ O ₂ surplus, B in ground state. (continued on next page)	42
2.9	Relative absorption maximum of B vs. irradiation time.	44
2.10	Relative absorption maxima after 30 minutes exposure to ¹ O ₂ surplus.	45
2.11	EPR spectra of TEMPO.	48

2.12	Relative integral surface of EPR spectra (of TEMPO) vs. irradiation time of A	49
3.1	Energy diagram showing photosensitized generation and photon emission of $^1\text{O}_2$	56
3.2	Principle of oxygen consumption measurements.	58
3.3	Choice of materials: Tested $^1\text{O}_2$ quenchers.	65
3.4	DABCO and HMTA covalently linked to polymers.	65
3.5	Employed photosensitizers P	67
3.6	Choice of materials: Tested Polymers.	67
3.7	69
3.8	TPE of $^1\text{O}_2$ in investigated polymers containing $^1\text{O}_2$ Quencher DABCO (Q1) in different molar ratios.	70
3.9	TPE of $^1\text{O}_2$ in investigated polymers containing $^1\text{O}_2$ quenchers Q7-9	71
3.10	Oxygen consumption measurements.	72
3.11	Oxygen concentration (pO_2) vs. irradiation time.	73
3.12	Stern-Volmer plots of PPO and PS polymer films containing no $^1\text{O}_2$ quencher and DABCO.	75
3.13	Oxygen concentration over irradiation time in polymer films PPO and PS.	76
3.14	Varying the DABCO concentration in PS - absorption spectra.	77
3.15	Oxygen concentration after one hour irradiation time for different polymers.	79
3.16	pO_2 versus irradiation time for different polymers.	80
3.17	Relative absorption maximum of P3 versus irradiation time for all investigated polymers.	81
3.18	Relative absorption maximum after thirty minutes of irradiation time for each polymer.	83
3.19	K_{SV} and k_q of P3 in PS.	84
3.20	Investigated amino comopunds for $^1\text{O}_2$ Quenching.	85
3.21	DABCO and HMTA covalently linked to polymers.	86
3.22	τ_{T_1} of P2 versus irradiation time measured in two polymers, EC and PS.	87
3.23	Degradated amount of P3 after 30 minutes irradiation time in PS and EC, containing different $^1\text{O}_2$ quenchers.	88
3.24	τ_{T_1} versus irradiation time for polymer films stored at 60°C for 72 hours.	89
3.25	NMR spectra of Q2 and Q4	93
3.26	NMR spectra of S1 and S2	94
3.27	NMR spectra of S3 and S4	95

4.1	Investigated super-acceptors 1 to 5	98
4.2	EPR spectra of compound 1	100
4.3	EPR spectra of compound 4	100
4.4	EPR spectra of compound 5	100
4.5	EPR spectra of compound 2	101
4.6	EPR spectra of compound 3 at 180 K.	101
4.7	EPR spectra of compound 3 at 270 K.	101

List of Tables

1.1	Polymers investigated in this work.	28
2.1	Investigated sensor dyes B , representing dye classes commonly used in optical chemical sensor systems.	36
3.1	Choice of materials: $^1\text{O}_2$ Quenchers.	66
3.2	Choice of materials: Photosensitizers.	66
3.3	Choice of materials: Polymers.	68
4.1	g factors of investigated compounds.	102

List of Abbreviations

$^1\text{O}_2$	Singlet Oxygen
[Q]	Quencher Concentration
ϵ	Absorption Coefficient
λ_{max}	Absorption Maximum
*R	Electronically Excited Molecule
ν	Frequency
Φ_F	Fluorescence Quantum Yield
τ	Luminescence Emission Lifetime
τ_0	Luminescence Emission Lifetime in the Absence of Quencher
K_{SV}	Stern-Volmer Constant
*Ru(bpy) $_3^{2+}$	Excited state Ruthenium tris(bipyridine)
CTCs	Charge-Transfer Complexes
DABCO	1,4-Diazabicyclo[2.2.2]octane
DMA	N,N-DiMethylAnilino
DME	1,2-Dimethoxyethane
EPR	Electron Paramagnetic Resonance
EPR	Electron Paramagnetic Resonance
F $_4$ -TCNQ	2,3,5,6-tetrafluoro-7,7,8,8-tetracyanoquinodimethane
FRET	Förster Resonance Energy Transfer

h	Planck's constant
HALS	Hindered Amine Light Stabilizers
HMTA	HexaMethyleneTetramine
HOMO	Highest Occupied Molecular Orbital
I	Luminescence Emission Intensity
I_0	Luminescence Emission Intensity in the Absence of Quencher
Ind	Indicator
ISC	Intersystem Crossing
LUMO	Lowest Unoccupied Molecular Orbital
MC	Metal-Centered excited state
MLTC	Metal-to-Ligand Charge Transfer
OCS	Optical Chemical Sensor
OLEDs	Organic Light-Emitting Diodes
P	Isolated Product (or Products)
PDMS	Polydimethyl Siloxanes
PdNTBP	Pd(II)6-Aza-13,20,27-trophenyltetrabenzoporphyrin
PdTPTBPF	Pd(II)meso-tetra(4-fluorophenyl)tetrabenzoporphyrin
PET	Photoinduced Electron Transfer
PMMA	Polymethyl Methacrylate
pO_2	partial pressure of oxygen, equivalent to oxygen concentration under standard conditions
PS	Polystyrene
PTFE	Polytetrafluoroethylenes
PVC	Polyvinyl Chloride
PVOH	PolyVinyl Alcohol

R	organic molecule
ROS	Reactive Oxygen Species
S ₀	Singlet Ground State
S ₁	First Excited Singlet State
S _Δ	Efficiency for Singlet Oxygen Generation
T ₁	First Excited Triplet State
TCNE	tetracyanoethene
TCNQ	7,7,8,8-tetracyanoquinodimethane
TEMP	4-hydroxy-2,2,6,6-tetramethylpiperidine
TEMPO	4-hydroxy-2,2,6,6-tetramethylpiperidine-N-oxyl
TPE	Total Photon Emission

Bibliography

1. M. Kivala, C. Boudon, J.-P. Gisselbrecht, B. Enko, P. Seiler, I. B. Müller, N. Langer, P. D. Jarowski, G. Gescheidt, F. Diederich, *Chemistry (Weinheim an der Bergstrasse, Germany)* **2009**, *15*, 4111–23.
2. IUPAC, *Journal of Pure Applied Chemistry* **2007**, *79*, 293–465.
3. N. J. Turro, V. Ramamurthy, J. Scaiano, *Modern Molecular Photochemistry of Organic Molecules*, University Science Books, **2010**.
4. J. F. Rabek, *Photodegradation of Polymers*, Springer, **1996**.
5. R. Kuhn, H. Rudy, T. Wagner-Jauregg, *Berichte der deutschen chemischen Gesellschaft* **1933**, *66*, 1950–1956.
6. M. Rauf, S. S. Ashraf, *Chemical Engineering Journal* **2009**, *151*, 10–18.
7. G. Schöllnhammer, P. Hemmerich, *European journal of biochemistry / FEBS* **1974**, *44*, 561–77.
8. M. Schuman Jorns, G. Schöllnhammer, P. Hemmerich, *European Journal of Biochemistry* **1975**, *48*, 35–48.
9. A. Juris, V. Balzani, F. Barigelletti, S. Campagna, P. Belser, A. von Zelewsky, *Coordination Chemistry Reviews* **1988**, *84*, 85–277.
10. P. Hartmann, *Analytical chemistry* **2000**, *72*, 2828–34.
11. Z. J. Fuller, W. D. Bare, K. a. Kneas, W. Y. Xu, J. N. Demas, B. a. DeGraff, *Analytical chemistry* **2003**, *75*, 2670–7.
12. B. Milosavljevic, J. K. Thomas, *Journal of Physical Chemistry* **1983**, *87*, 616–621.
13. T. Kennelly, H. D. Gafney, M. Braun, *Journal of the American Chemical Society* **1985**, *107*, 4431–4440.

14. a.R. Khataee, M. Kasiri, *Journal of Molecular Catalysis A: Chemical* **2010**, *328*, 8–26.
15. A. Houas, H. Lachheb, M. Ksibi, E. Elaloui, C. Guillard, J.-m. Herrmann, *Applied Catalysis B: Environmental* **2001**, *31*, 145–157.
16. I. K. Konstantinou, T. A. Albanis, *Applied Catalysis B: Environmental* **2004**, *49*, 1–14.
17. H. Lachheb, E. Puzenat, A. Houas, M. Ksibi, E. Elaloui, C. Guillard, J.-M. Herrmann, *Applied Catalysis B: Environmental* **2002**, *39*, 75–90.
18. A. L. Linsebigler, G. Lu, J. T. Yates, *Chemical reviews* **1995**, *95*, 735–758.
19. C. Schweitzer, R. Schmidt, *Chemical reviews* **2003**, *103*, 1685–757.
20. Ranby B., J. F. Rabek, *Singlet Oxygen Reactions with Organic Compounds & Polymers*, Wiley, **1978**.
21. . Krasnovsky, *Journal of Photochemistry and Photobiology A: Chemistry* **2008**, *196*, 210–218.
22. B. Valeur, *Molecular Fluorescence: Principles and Applications*, Wiley-VCH, Weinheim, **2011**.
23. E. L. Clennan, A. Pace, *Tetrahedron* **2005**, *61*, 6665–6691.
24. M. DeRosa, *Coordination Chemistry Reviews* **2002**, *233-234*, 351–371.
25. P. R. Ogilby, *Photochemical & photobiological sciences : Official journal of the European Photochemistry Association and the European Society for Photobiology* **2010**, *9*, 1543–60.
26. D. R. Kearns, *Chemical Reviews* **1971**, *71*, 395–427.
27. D. J. Carlsson, D. M. Wiles, *Journal of Macromolecular Sciences, Part C: Polymer Reviews* **1976**, *14*, 65–106.
28. A. P. Darmanyan, C. S. Foote, P. Jardon, *The Journal of Physical Chemistry* **1995**, *99*, 11854–11859.
29. J. F. Rabek, B. Rånby, *Photochemistry and Photobiology* **1978**, *28*, 557–569.

30. C. S. Foote, J. Wexler, *Journal of the American Chemical Society* **1964**, *86*, 3880–3881.
31. F. Wilkinson, W. P. Helman, A. B. Ross, *Journal of Physical and Chemical Reference Data* **1995**, *24*, 663.
32. E. Corey, W. c. Taylor, *Journal of the American Chemical Society* **1964**, *86*, 3881–3882.
33. G. S. Egerton, *British Polymer Journal* **1971**, *3*, 63–67.
34. P. Hartmann, *Sensors and Actuators B: Chemical* **1998**, *51*, 196–202.
35. E. R. Carraway, J. N. Demas, B. a. DeGraff, J. R. Bacon, *Analytical Chemistry* **1991**, *63*, 337–342.
36. J. Pospisil, S. Nespurek, J. Pilar, *Polymer Degradation and Stability* **2008**, *93*, 1681–1688.
37. S. Borisov, G. Nuss, W. Haas, R. Saf, M. Schmuck, I. Klimant, *Journal of Photochemistry and Photobiology A: Chemistry* **2009**, *201*, 128–135.
38. X. Zhang, J. Rodgem, *Journal of Physical Chemistry* **1995**, *99*, 12797–12803.
39. H. Zweifel, *Macromolecular Symposia* **1997**, *115*, 181–201.
40. P. Gijssman, *Polymer* **2002**, *43*, 1573–1579.
41. R. Ballardini, G. Beggiato, P. Bortolus, A. Faucitano, A. Buttafava, F. Gratani, *Polymer Degradation and Stability* **1984**, *7*, 41–53.
42. B. M. Weidgans, C. Krause, I. Klimant, O. S. Wolfbeis, *The Analyst* **2004**, *129*, 645–650.
43. M. Ogawa, M. Sohmiya, Y. Watase, *Chemical communications (Cambridge, England)* **2011**, *47*, 8602–4.
44. Y. Kohno, R. Kinoshita, S. Ikoma, K. Yoda, M. Shibata, R. Matsushima, Y. Tomita, Y. Maeda, K. Kobayashi, *Applied Clay Science* **2009**, *42*, 519–523.
45. IUPAC, *Pure and Applied Chemistry* **1991**, *63*, 1247.
46. K. Camman, G. Guibault, E. Hall, R. Kellner, H. Schmidt, O. S. Wolfbeis **1996**.

47. C. McDonagh, C. S. Burke, B. D. MacCraith, *Chemical reviews* **2008**, *108*, 400–22.
48. J. Lin, D. Liu, *Analytica chimica acta* **2000**, *408*, 49–55.
49. B. Timmer, W. Olthuis, a. Berg, *Sensors and Actuators B: Chemical* **2005**, *107*, 666–677.
50. K. Waich, T. Mayr, I. Klimant, *Talanta* **2008**, *77*, 66–72.
51. P. Levillain, D. Fompeydie, *Analytical Chemistry* **1985**, *57*, 2561–2563.
52. S. M. Borisov, I. Klimant, *Analytical chemistry* **2007**, *79*, 7501–9.
53. O. Stern, M. Volmer, *Physikalische Zeitschrift* **1919**, *20*, 183–188.
54. O. S. Wolfbeis, *Analytical chemistry* **2006**, *78*, 3859–74.
55. O. S. Wolfbeis, *Journal of Materials Chemistry* **2005**, *15*, 2657.
56. D. Carlsson, *Makromol. Chem.* **1984**, *8*, 79–88.
57. S. Fairgrieve, *Polymer Degradation and Stability* **1984**, *8*, 107–121.
58. P. Gijssman, J. Hennekens, D. Tummers, *Polymer Degradation and Stability* **1993**, *39*, 225–233.
59. S. M. Borisov, D. L. Herrod, I. Klimant, *Sensors and Actuators B: Chemical* **2009**, *139*, 52–58.
60. K. Oige, T. Avarmaa, A. Suisalu, R. Jaaniso, *Sensors and Actuators B: Chemical* **2005**, *106*, 424–430.
61. W. Jivaramonaikul, P. Rashatasakhon, S. Wanichwecharungruang, *Photochemical & photobiological sciences : Official journal of the European Photochemistry Association and the European Society for Photobiology* **2010**, 1–9.
62. S. M. Borisov, I. Klimant, *Informacije MIDE M* **2010**, *40*, 291–297.
63. J. Wu, W. Liu, J. Ge, H. Zhang, P. Wang, *Chemical Society reviews* **2011**, *40*, 3483–95.
64. H. N. Kim, Z. Guo, W. Zhu, J. Yoon, H. Tian, *Chemical Society reviews* **2011**, *40*, 79–93.
65. Q. Zhao, F. Li, C. Huang, *Chemical Society reviews* **2010**, *39*, 3007–30.

66. L. F. Capitán-Vallvey, A. J. Palma, *Analytica chimica acta* **2011**, *696*, 27–46.
67. F.-Y. Ge, L.-G. Chen, *Journal of fluorescence* **2008**, *18*, 741–7.
68. R. Wang, C. Yu, F. Yu, L. Chen, *TrAC Trends in Analytical Chemistry* **2010**, *29*, 1004–1013.
69. X.-l. Wu, X.-l. Jin, Y.-x. Wang, Q.-b. Mei, J.-l. Li, Z. Shi, *Journal of Luminescence* **2011**, *131*, 776–780.
70. J. Han, K. Burgess, *Chemical reviews* **2010**, *110*, 2709–28.
71. T. Li, Z. Yang, Y. Li, Z. Liu, G. Qi, B. Wang, *Dyes and Pigments* **2011**, *88*, 103–108.
72. T. Mayr, S. M. Borisov, T. Abel, B. Enko, K. Waich, G. Mistlberger, I. Klimant, *Analytical Chemistry* **2009**, *81*, 6541–6545.
73. A. Helal, M. H. Or Rashid, C.-H. Choi, H.-S. Kim, *Tetrahedron* **2011**, *67*, 2794–2802.
74. K. C. Ko, J.-S. Wu, H. J. Kim, P. S. Kwon, J. W. Kim, R. a. Bartsch, J. Y. Lee, J. S. Kim, *Chemical communications (Cambridge, England)* **2011**, *47*, 3165–7.
75. S. Voutsadaki, G. K. Tsikalas, E. Klontzas, G. E. Froudakis, H. E. Katerinopoulos, *Chemical communications (Cambridge, England)* **2010**, *46*, 3292–4.
76. M. Suresh, A. Das, *Tetrahedron Letters* **2009**, *50*, 5808–5812.
77. K. Swamy, M.-J. Kim, H.-R. Jeon, J.-Y. Jung, J.-Y. Yoon, *Bulletin of the Korean Chemical Society* **2010**, *31*, 3611–3616.
78. J. Yao, W. Dou, W. Qin, W. Liu, *Inorganic Chemistry Communications* **2009**, *12*, 116–118.
79. M. Y. Jung, D. B. Min, *Journal of food science* **2009**, *74*, C449–55.
80. J. R. Sheng, F. Feng, *Sensors (Peterborough, NH)* **2008**, 37–41.
81. N. Saleh, Y. a. Al-Soud, W. M. Nau, *Spectrochimica acta. Part A, Molecular and biomolecular spectroscopy* **2008**, *71*, 818–22.

82. T. Hien Nguyen, T. Venugopalan, T. Sun, K. T. Grattan, *2009 IEEE Sensors* **2009**, 89–94.
83. S. W. Hong, W. H. Jo, *Polymer* **2008**, *49*, 4180–4187.
84. K. Waich, S. Borisov, T. Mayr, I. Klimant, *Sensors and Actuators B: Chemical* **2009**, *139*, 132–138.
85. S. G. Schulman, S. Chen, F. Bai, M. J. P. Leiner, L. Weis, O. S. Wolfbeis, *Analytica Chimica Acta* **1995**, *304*, 165–170.
86. O. S. Wolfbeis, E. Furlinger, H. Kroneis, H. Marsoner, *Fresenius' Journal of Analytical Chemistry* **1983**, *314*, 119–124.
87. A. Mills, Q. Chang, *The Analyst* **1993**, *118*, 839.
88. S. M. Borisov, R. Seifner, I. Klimant, *Analytical and bioanalytical chemistry* **2011**, *400*, 2463–74.
89. C.-S. Chu, Y.-L. Lo, *Sensors and Actuators B: Chemical* **2009**, *143*, 205–210.
90. R. N. Dansby-Sparks, J. Jin, S. J. Mechery, U. Sampathkumaran, T. W. Owen, B. D. Yu, K. Goswami, K. Hong, J. Grant, Z.-L. Xue, *Analytical chemistry* **2010**, *82*, 593–600.
91. D. Wencel, J. P. Moore, N. Stevenson, C. McDonagh, *Analytical and bioanalytical chemistry* **2010**, *398*, 1899–907.
92. S. M. Borisov, I. Klimant, *Dyes and Pigments* **2009**, *83*, 312–316.
93. Y. Amao, *Microchimica Acta* **2003**, *143*, 1–12.
94. H. N. Kim, K. Swamy, J. Yoon, *Tetrahedron Letters* **2011**, *52*, 2340–2343.
95. S. M. Borisov, G. Zenkl, I. Klimant, *ACS applied materials & interfaces* **2010**, *2*, 366–74.
96. Y. Amao, *Analytica Chimica Acta* **2001**, *445*, 177–182.
97. J. N. Demas, B. a. DeGraff, *Analytical Chemistry* **1991**, *63*, 829A–837A.
98. S. M. Borisov, I. Klimant, *Microchimica Acta* **2008**, *164*, 7–15.

99. J. Brooks, Y. Babayan, S. Lamansky, P. I. Djurovich, I. Tsyba, R. Bau, M. E. Thompson, *Inorganic chemistry* **2002**, *41*, 3055–66.
100. P. Anzenbacher, Y.-L. Liu, M. E. Kozelkova, *Current opinion in chemical biology* **2010**, *14*, 693–704.
101. J. E. Mark (Ed.), *Polymer Data Handbook*, Oxford University Press, **1999**.
102. D. Bellus in *Singlet Oxygen. Reactions with Organic Compounds & Polymers*, Ranby B., J. F. Rabek (Eds.), Wiley, **1978**, chapter 9, pp. 61–110.
103. K. Ohara, K. Kikuchi, T. Origuchi, S.-i. Nagaoka, *Journal of photochemistry and photobiology. B, Biology* **2009**, *97*, 132–7.
104. S. He, L. Jiang, B. Wu, Y. Pan, C. Sun, *Biochemical and biophysical research communications* **2009**, *379*, 283–7.
105. B. M. Monroe, *The Journal of Physical Chemistry* **1977**, *81*, 1861–1864.
106. J. R. Lancaster, A. a. Martí, J. López-Gejo, S. Jockusch, N. O'Connor, N. J. Turro, *Organic letters* **2008**, *10*, 5509–12.
107. K. C. Das, H. P. Misra, *Molecular and Cellular Biochemistry* **2004**, *262*, 127–133.
108. S.-i. Nagaoka, A. Fujii, M. Hino, M. Takemoto, M. Yasuda, M. Mishima, K. Ohara, A. Masumoto, H. Uno, U. Nagashima, *The journal of physical chemistry. B* **2007**, *111*, 13116–23.
109. C. Ouannes, T. Wilson, *Journal of the American Chemical Society* **1968**, *90*, 6527–6528.
110. F. E. M. Vieyra, H. J. Boggetti, I. C. Zampini, R. M. Ordoñez, M. I. Isla, R. M. S. Alvarez, V. De Rosso, A. Z. Mercadante, C. D. Borsarelli, *Free radical research* **2009**, *43*, 553–64.
111. E. A. Ogryzlo, C. W. Tang, *Journal of the American Chemical Society* **1970**, *92*, 5034–5036.
112. J. R. Kanofsky, P. D. Sima, *Photochemistry and photobiology* **2009**, *85*, 391–9.

113. M. I. Gutiérrez, *Photochemical & photobiological sciences : Official journal of the European Photochemistry Association and the European Society for Photobiology* **2008**, *7*, 480–4.
114. S. Kaiser, P. Di Mascio, M. Murphy, *Archives of Biochemistry and Biophysics* **1990**, *277*, 101–108.
115. V. V. De Rosso, F. E. Morán Vieyra, A. Z. Mercadante, C. D. Borsarelli, *Free radical research* **2008**, *42*, 885–91.
116. C. Corvaja in *Electron Paramagnetic Resonance, A Practitioners Toolkit*, M. Brustolon, E. Giamello (Eds.), Wiley, **2009**, chapter 1, pp. 3–35.
117. C. F. Chignell, *Journal of Pure Applied Chemistry* **1990**, *62*, 301–305.
118. J. R. Harbour, S. L. Issler, M. L. Hair, *Journal of the American Chemical Society* **1980**, *102*, 7779–7780.
119. L. Y. Zang, Z. Y. Zhang, H. P. Misra, *Photochemistry and photobiology* **1990**, *52*, 677–83.
120. L.-Y. Zang, F. Van Kuijk, B. Misra, H. Misra, *Biochemistry and Molecular Biology International* **1995**, *37*, 283–293.
121. R. Bensasson, J. Frederiksen, M. Rougee, D. Lexa, N. Harrit, *Molecular Pharmacology* **1992**, *42*, 718–722.
122. D. M. Wiles in *Singlet Oxygen. Reactions with Organic Compounds & Polymers*, Ranby B., J. F. Rabek (Eds.), Wiley, **1978**, chapter 34, pp. 320–327.
123. R. H. Young, D. Brewer in *Singlet Oxygen. Reactions with Organic Compounds & Polymers*, B. Ranby, J. F. Rabek (Eds.), Wiley, **1978**, chapter 6, pp. 36–60.
124. A. A. Krasnovsky, *Biochemistry (Moscow)* **2007**, *72*, 1065–1080.
125. S. Egorov, V. Kamalov, N. Koroteev, J. Krasnovsky, B. Toleutaev, S. Zinukov, *Chemical Physics Letters* **1989**, *163*, 421–424.
126. P. R. Ogilby, C. S. Foote, *Journal of the American Chemical Society* **1982**, *104*, 2069–2070.

127. J. Baier, T. Fuss, C. Pöllmann, C. Wiesmann, K. Pindl, R. Engl, D. Baumer, M. Maier, M. Landthaler, W. Bäuml, *Journal of photochemistry and photobiology. B, Biology* **2007**, *87*, 163–73.
128. P. R. Ogilby, M. P. Dillon, M. Kristiansen, R. L. Clough, *Macromolecules* **1992**, *25*, 3399–3405.
129. P. R. Ogilby, I. Kai Kong, *Journal of the American Chemical Society* **1987**, *109*, 4746–4747.
130. K. Schiller, F. W. Müller, *Polymer International* **1991**, *25*, 19–22.
131. A. Rivaton, J.-L. Gardette, B. Mailhot, S. Morlat-Therlas, *Macromolecular Symposia* **2005**, *225*, 129–146.
132. F. Gugumus, *Die Angewandte Makromolekulare Chemie* **1990**, *176*, 27–42.
133. F. Fraïsse, A. Kumar, S. Commereuc, V. Verney, *Journal of Applied Polymer Science* **2006**, *99*, 2238–2244.
134. P. W. Labuschagne, W. A. Germishuizen, S. M. C. Verry, F. S. Moolman, *European Polymer Journal* **2008**, *44*, 2146–2152.
135. S. a. Stern, V. M. Shah, B. J. Hardy, *Journal of Polymer Science Part B: Polymer Physics* **1987**, *25*, 1263–1298.
136. R. Dedic, M. Korinek, a. Molnar, a. Svoboda, J. Hala, *Journal of Luminescence* **2006**, *119-120*, 209–213.
137. J. Regensburger, Ph.D. thesis, Universität Regensburg, **2010**.
138. R. H. Young, R. L. Martin, *Journal of the American Chemical Society* **1972**, *94*, 5183–5185.
139. P. Klemchuk, *Polymer Degradation and Stability* **1988**, *22*, 241–274.
140. O. W. Webster, *Journal of Polymer Science Part A: Polymer Chemistry* **2002**, *40*, 210–221.
141. J. S. Miller, *Angewandte Chemie (International ed. in English)* **2006**, *45*, 2508–25.
142. W. Kaim, M. Moscherosch, *Coordination Chemistry Reviews* **1994**, *129*, 157–193.

143. K. Walzer, B. Maennig, M. Pfeiffer, K. Leo, *Chemical reviews* **2007**, *107*, 1233–71.
144. W. Phillips, J. Rowell, S. Weissmann, *The Journal of Chemical Physics* **1960**, *33*, 626.
145. F. Gerson, R. Heckendorn, D. O. Cowan, A. M. Kini, M. Maxfield, *Journal of the American Chemical Society* **1983**, *105*, 7017–7023.